Activation of *n*-octane using VO_x/MgO catalysts prepared by a mixed fuel solution combustion synthesis method

Samantha Padayatchee

21002028

SUBMITTED IN FULFILMENT OF THE REQUIREMENTS OF THE DEGREE OF MASTER OF APPLIED SCIENCE IN CHEMISTRY IN THE FACULTY OF APPLIED SCIENCES AT THE DURBAN UNIVERSITY OF TECHNOLOGY

May 2024

Supervisor: DOCTOR P. NTOLA
Co-Supervisor: PROFESSOR H.B. FRIEDRICH
Co-Supervisor: PROFESSOR E.J OLIVIER

DECLARATION

I, **Samantha Padayatchee,** declare that the thesis submitted for the degree of Master of Applied Science in Chemistry at the Durban University of Technology is the result of my investigation and has not already been accepted in substance for any degree and is not being concurrently submitted for any other degree. All the work was done by the author.

Student name : Samantha Padayatchee

Student signature**:** .....Date: 12.08.2024

Supervisor name : Dr P. Ntola

Supervisor signature **:** te**: 12/08/2024**

Co-Supervisor name : Professor H.B. Friedrich

Co-Supervisor signature **: 12/08/2024**

Co-Supervisor name : Prof E.J Olivier

Co-Supervisor signature ate**: 12/08/2024**

DEDICATION

To my beloved family,

Mom and Dad, thank you for always being my rock and for constantly reminding me of my worth. Your wisdom and guidance have been invaluable in shaping who I am today. To my brother and sister-in-law thank you for always cheering me on, making me laugh, and reminding me to stay humble. Your friendship and presence in my life have been such a gift. To my fur baby Lola, thank you for being the best stress reliever, and to my extended family for their words of encouragement, love and support. I dedicate this thesis to all of you, with all my heart, and I hope that it brings you as much pride and happiness as it does for me.

ACKNOWLEDGEMENTS

I would like to express my sincerest gratitude to my supervisor **Dr P Ntola** for her immense contributions to this study. Dr Ntola's guidance, support, and expertise have been invaluable throughout this research process. Her patience with me, especially during my moments of self-doubt and struggles, has been truly extraordinary including critical feedback and insightful comments that challenged me to think and improve my writing. I would like to express my deepest appreciation to my co-supervisors **Prof. H.B Friedrich** and **Prof E.J Olivier** for their tremendous contributions to this work. Their unwavering support, guidance, and expertise were instrumental to the successful completion of this work.

A very special thanks to the Catalysis Research Group **(CRG)-UKZN** for their exceptional guidance and encouragement throughout my laboratory work. Every member of that group supported me wholeheartedly. Special thanks go to **Alisa Govender** from Sasol for her thoughtful and insightful comments, both positive and critical, helped me to refine and clarify my arguments, inclusive of assistance with specific characterization techniques.

CONFERENCE CONTRIBUTIONS

Poster Presentations

S. Padayatchee, H.B Friedrich, E.J Olivier, A. Govender, A.K Datye, H.N Pham and P. Ntola, *Activation of n-octane by VO_x/MgO catalysts using solution combustion synthesis (SCS): Mixed fuel approach*, CATSA 2022, Champagne sports resort, Drakensberg, KwaZulu-Natal, South Africa.

S. Padayatchee, H.B Friedrich, E.J Olivier, A. Govender, A.K Datye, H.N Pham and P. Ntola, *Activation of n-octane by VO_x/MgO catalysts using solution combustion synthesis (SCS): Mixed fuel approach*, Applied Science Faculty Research Day, Musgrave Hotel, 2022, Durban, KwaZulu-Natal, South Africa

S. Padayatchee, H.B Friedrich, E.J Olivier, A. Govender and P. Ntola, *Characterization of VO_x/MgO catalysts produced using solution combustion synthesis: Mixed fuel approach*, MSSA 2022, Gold reef city, Johannesburg, South Africa

ABSTRACT

Oxidative dehydrogenation (ODH) is an important chemical process used to produce various industrial fuels and building blocks, such as butadiene, styrene, and propylene. In this process, a catalyst facilitates the oxidation of hydrocarbons, leading to the removal of two hydrogen atoms and the formation of an olefin. This reaction has attracted significant attention due to its ability to generate high yields and low by-product formation, making it an environmentally sustainable approach for olefin production. However, ODH reactions face certain challenges that must be addressed to make them more efficient and viable for large-scale production. The major challenge in this process is the low selectivity for the formation of olefins, as side reactions lead to the formation of unwanted by-products. In addition, the catalyst employed should exhibit stability and maintain high levels of activity and selectivity under the specified operating conditions.

In recent years, the solution combustion synthesis method (SCS) has emerged as a promising technique for producing highly active and stable catalysts for oxidative dehydrogenation. In the SCS method, a precursor solution is heated in a furnace to produce a high-temperature exothermic reaction that drives the formation of nanoscale particles. SCS has several advantages over traditional synthesis methods such as sol-gel and solid-state reactions. This includes its simplicity in eliminating the need for an inert atmosphere or subsequent calcination procedures. Additionally, it allows for precise control of the particle size, morphology, and composition, which can significantly influence the catalyst's performance. It is also a cost-effective technique as it uses simple and inexpensive chemicals as precursors. The nanoparticles created through SCS are characterized by their ability to bind to high surface areas and tailor their specific morphology, such as a highly porous structure or a specific crystal facet. This structural control can significantly impact the catalyst's performance, as it influences the catalyst's active sites and the reactant's diffusion and adsorption properties.

In this study, VO_x/MgO catalysts were synthesized using a solution combustion synthesis method with three fuel mixtures as reducing agents. The fuel mixtures comprised of urea/hydrazine hydrate (UR/HH), glycine/urea (GLY/UR), and glycine/hydrazine hydrate (GLY/HH). The catalysts were characterized using BET, XRD, ICP-OES, HR-TEM, TPR and TPD-MS. Catalytic testing was performed in a continuous flow fixed-bed tubular stainless-steel reactor, operated in a down-flow mode, using air as the oxidant and nitrogen as the diluent gas. Reactions were carried out over a temperature range of 350-450 °C with 5% feed and 350-450 °C at 12% feed. The gas flow rates were varied to attain gas hourly space velocities of 8000 h^{-1}. The carbon to oxygen ratio was 8:2. The catalyst bed was maintained at a volume of 1 cm^3 with pellet sizes ranging between 600 – 1000 um. The reaction product stream was analyzed using gas chromatographs, one fitted with a thermal conductivity detector, and the other with a flame ionization detector.

The results obtained from this study demonstrated varying morphologies and surface areas for each catalyst. The VO_x/MgO catalysts showed the distribution of vanadium on the surface of the support with an aggregation of VO_x clusters at certain locations. The $\%V_2O_5$ loading varied from 14 wt%- 14.9 wt%, which correlated with the SEM-EDS results. XRD and Rietveld refinement results demonstrated that the vanadium supported on MgO catalysts was present as biphasic constituents, with the predominant phase being attributed to the MgO periclase phase. The second phase was identified as the magnesium orthovanadate ($Mg_3(VO_4)_2$), while the crystalline $Mg_2V_2O_7$ magnesium pyrovanadate phase was only identified only in the GLY/UR catalyst. Further characterization was performed using TPR for redox properties and TPD-MS for acid-base properties.

The GLY/UR and GLY/HH catalysts displayed a high H_2 consumption, with two distinct reduction peaks followed by a high concentration of Brønsted acid sites of >100 µmole/g for both catalysts. Catalytic testing revealed that all three catalysts exhibited activity for the ODH of *n*-octane. The selectivity towards the desired products was dependent on the vanadium concentration and the phase composition of the catalysts. Octene isomers, aromatic compounds, cracked products and carbon oxides were identified in the product stream. The GLY/HH catalyst displayed the best selectivity of 66% towards the formation of octenes. A decrease in feed concentration from 12% to 5% led to an increase in octene selectivity, specifically at 450 ºC. This confirmed that the selectivity and conversion depend on the reaction temperature, phase composition and morphology.

CONTENTS

DECLARATION 1

DEDICATION 2

ACKNOWLEDGEMENT 3

LIST OF ACRONYMS AND SYMBOLS 13

CONFERENCE CONTRIBUTIONS 4

ABSTRACT 5

LIST OF FIGURES 9

LIST OF TABLES 11

LIST OF EQUATIONS 12

Chapter 1: Introduction 14

1.1 Background 14
1.1.1 Homogeneous catalysis 14
1.1.2 Heterogeneous catalysis 15
1.1.3 Alkanes 17

Chapter 2: Literature Review 19

2.1 Oxidative Dehydrogenation 19
2.1.1 Redox properties 20
2.1.2 Acid-base properties 21
2.1.3 Selective oxidation on medium chain alkanes 21
2.1.4 Oxidative dehydrogenation of n-octane 22
2.1.5 Vanadia-based catalysts 23
2.1.6 Magnesium oxide as a support for vanadium 24
2.1.7 VO_x/MgO catalysts on short chain alkanes 25
2.1.8 VO_x/MgO catalysts for medium-chain alkanes 26
2.1.9 VO_x/MgO catalysts on the ODH of n-octane 26
2.2 Solution Combustion Synthesis (SCS) 28
2.2.1 Single-fuel approach 29
2.2.3 Fuel selection for the mixed fuel approach 30
2.3 Aim and Objectives 31

Chapter 3: Research design: Experimental 32

3.1 Solution combustion synthesis parameters 32
3.1.2 Fuel type 32
3.1.3 Oxidant type 32
3.1.5 Mixed Fuel approach 34
3.1.6 Catalyst preparation 35
3.1.7 Synthesis of the MgO supports 36
3.1.8 Catalyst preparation for VO_x/MgO catalysts 37
3.1.9 Adiabatic temperature 38
3.2 Catalyst characterization 39
3.2.1 Inductively coupled plasma optical emission spectroscopy (ICP-OES) 39
3.2.2 X-ray diffraction and Rietveld refinement (XRD) 40
3.2.3 Temperature programmed reduction (TPR) 40
3.2.4 Temperature programmed desorption-CO_2-(TPD) 40
3.2.5 Scanning electron microscopy (SEM) 40

3.2.6 Transmission electron microscopy (TEM) 40
3.2.7 Brunauer-Emmett-Teller (BET) analysis 41
Chapter 4: Results and Discussion 42
4.1 Surface and elemental properties 42
4.1.1 XRD and Rietveld refinement 45
4.1.2 Transmission electron microscopy 48
4.1.3 Scanning Transmission Electron Microscopy - Electron Energy Loss Spectroscopy 52
4.1.4 Temperature programmed reduction (TPR) 56
4.1.5 Temperature-programmed desorption 58
4.1.6 Thermodynamics 59
4.1.7 Phase formation of VO_x/MgO 63
Chapter 5: Catalytic Testing 65
5.1 MgO supports 65
5.2 VO_x/MgO catalysts 68
5.3 Influence of the feed ratio 72
Chapter 6: Conclusions and recommendations 79
REFERENCES 81
APPENDIX A 93
APPENDIX B 93

LIST OF FIGURES

Figure 1.1**:** Scheme for the four-step process for heterogeneous catalysis (Haber, 1994) 15

Figure 1.2: The hydrogenation of polyunsaturated fats and oils using Ni catalysts (Richardson, 1989) 16

Figure 1.3**:** Limitations of the prominent dehydrogenation technique (Centi et al., 2001) 18

Figure 2.1: Cycle of reduction/oxidation on the surface of a catalyst obeying MvK mechanism (Wang et al., 2018) 20

Figure 2.2: Schematic representation of V_2O_5 nanoparticle formation on top of a surface vanadia monolayer on an oxide support 25

Figure 2.3**:** List of industries that use SCS produced nanomaterials (Parauha et al., 2021) 28

Figure 2.4: Schematic flow of the SCS process (Gotoh et al., 2020) 29

Figure 3. 2**:** Schematic flow of SCS process for the preparation of MgO and VOx/MgO using mixed fuel 36

Figure 4.1**:** Correlation between crystallite size and surface area for the mixed fuel VO_x/MgO catalyst prepared by fuel mixtures GLY/UR, GLY/HH and UR/HH 43

Figure 4.2**:** Low-temperature nitrogen adsorption-desorption isotherms for mixed fuel VO_x/MgO catalyst 44

Figure 4.3**:** X-ray diffractogram for VOx/MgO catalyst prepared by GLY/UR fuel mix 45

Figure 4.4**:** X-ray diffractogram for VOx/MgO catalyst prepared by GLY/HH fuel mix 46

Figure 4.5: X-ray diffractogram for VOx/MgO catalyst prepared by UR/HH fuel mix 47

Figure 4.6(A) EDS spectrum of sample GLY/UR (B) EDS spectrum of sample GLY/HH (C) EDS spectrum of sample UR/HH. 49

Figure 4.7(A) Bright-field TEM image of sample GLY/UR. (B) Bright-field TEM image of sample GLY/HH. (C) Bright-field TEM image of sample UR/HH 50

Figure 4.8A) SAED-TEM pattern of catalyst GLY/UR. (B) SAED-TEM pattern of catalyst GLY/HH (C) SAED-TEM pattern of catalyst UR/HH 51

Figure 4.9**:** (A) High-resolution image, (B) FFT of (A) 52

Temp : Elemental distribution maps of sample GLY/UR generated using STEM-EELS 52

Figure 4.11: Elemental distribution maps of sample GLY/HH generated using STEM-EELS 53

Figure 4.12: Elemental distribution maps of sample UR/HH generated using STEM-EELS 54

Figure 4.13**:** (A) HCD image of sample GLY/UR. (B) HCD image of sample GLY/HH. (C) HCD image of sample UR/H 55

Figure 4.14**:** H_2-TPR profile of VO_x/MgO catalysts 57

Figure 4.15: Adiabatic temperature as a function of VO_x/MgO and MgO catalysts 62

Figure 4.16: Adiabatic temperature as a function of no of moles release 62

Figure 4.17: Phase change graph showing the formation of the different phases in VO_x/MgO 64

Figure 5.1**:** Conversion of n-octane of MgO catalysts. (A) GLY/HH, (B) GLY/UR and (C) UR/HH **(**Reaction conditions: Temperature = (400-500 °C), Feed = 12% n-octane, C: O = 8:2 and GHSV = 8005 h^{-1}) 66

Figure 5.2**:** Selectivity as a function of temperature of MgO catalysts. (A) GLY/HH, (B) GLY/UR and (C) UR/HH (Reaction conditions: Temperature = (400-500 °C), Feed = 12% n-octane, C: O = 8:2 and GHSV = 8005 h^{-1}) 68

Figure 5.3**:** Conversion of n-octane of VO_x/MgO catalysts. (A) GLY/HH, (B) GLY/UR and (C) UR/HH **(**Reaction conditions: Temperature = (400-500 °C), Feed = 12% n-octane, C:O = 8:2 and GHSV = 8005 h^{-1}) 69

Figure 5.4: Selectivity as a function of temperature of VO_x/MgO catalysts prepared by mixed fuels (A) GLY/HH, (B) GLY/UR and (C) UR/HH (Reaction conditions: Temperature = (400-500 °C), Feed = 12% n-octane, C:O = 8:2 and GHSV = 8005 h^{-1}) 72

Figure 5.5**:** Conversion of n-octane of VO_x/MgO catalysts. (A) GLY/HH, (B) GLY/UR and (C) UR/HH **(**Reaction conditions: Temperature = (350-450 °C), Feed = 5% n-octane, C: O = 8:2 and GHSV = 8005 h^{-1}) 73

Figure 5.6**:** Selectivity as a function of temperature of VO_x/MgO catalysts**.** (A) GLY/HH, (B) GLY/UR and (C) UR/HH (Reaction conditions: Temperature = (350-500 °C), Feed = 5% n-octane, C:O = 8:2 and GHSV = 8005 h^{-1}) 76

Figure 5.7**:** Octene **s**electivity of VO_x/MgO catalysts with the 5% n-octane feed as a function of temperature (Reaction conditions: Temperature = (350 °C-450 °C), Feed = 5% n-octane, C:O = 8:2 and GHSV = 8002 h^{-1} 77

Figure 5.8: Selectivity at iso-conversion as a function of temperature over the VO_x/MgO catalysts prepared by mixed fuels (A) GLY/HH, (B) GLY/UR (Reaction conditions: Temperature = 450 °C, Feed = 12% n-octane, C:O: 8:2 and GHSV: GLY/UR = 10082 h^{-1} and GLY/HH =11139 h^{-1} *78*

LIST OF TABLES

Table 2. 1**:** List of catalysts used in ODH, obeying different chemical properties 21

Table 3. 1:Elements and their oxidizing/reducing valence 39

Table 3. 2**:** The corresponding quantities of metal nitrate salts and fuel compositions 37

Table 3. 3**:** Calculated values of equivalence ratios (φ) 37

Table 3. 4: Enthalpies and heat capacities data for the calculation of the adiabatic temperature of VO_x/MgO synthesized by SCS method (Sherikar and Umarji, 2011) 39

Table 4. 1**:** Nitrogen physisorption results and elemental composition obtained from BET and ICP-OES 42

Table 4. 2: XRD and Rietveld refinement 47

Table 4. 3**:** TPR data for mixed fuel VO_x/MgO 57

Table 4. 4: Temperature programmed desorption of n-propylamine using an MS detector to quantify the concentration of Brønsted acidic sites over the surfaces of selected catalysts. 59

Table 4. 5**:** Physical characteristics of the powders 61

Table 4. 6: Flame characteristics 61

LIST OF EQUATIONS

$C_2H_4\,(g) + H_2\,(g) \longrightarrow C_2H_6\,(g)$ Equation 1. 1 16

$C_nH_{2n+2} \rightarrow C_nH_2n + H_2$ Equation 1. 2 17

$C_nH_{2n+2} + 0.5O_2 \rightarrow C_nH_2n + H_2O$ Equation 2. 1 19

$\varphi = -1.\frac{RV}{OV}n$ Equation 3.1 33

OV-$Mg(NO_3)_2.6H_2O$ = 1Mg = +2; 2N = 0; 6O = -12; $6H_2O$ = -10 Equation 3.2 33

OV-NH_4VO_3 = 1V = +5; 1N = 0; 4H = +4; 3O = -6 = +3 Equation 3.3 33

RV-$C_2H_5NO_2$ = 2C = +8; 5H = +5; 1N = 0; 2O = -4 = +9 Equation 3.4 33

RV-$CO(NH_2)_2$ = 1C = +4; 1O = -2; 2N = 0; 4H = +4 = +6 Equation 3.5 33

RV- $N_2H_4.H_2O$ =2N = 0; 6H = +6; 1O = -2 = +4 Equation 3.6 33

$0.02\ NH_4VO_3 + 0.25\ Mg(NO_3)_2.6H_2O + 0.25\ CO(NH_2)_2 + 0.25\ C_2H_5NO_2 + 0.33\ O_2 \rightarrow 0.01\ V_2O_5 +$

$0.25\ MgO + 0{,}64\ N_2 + 0.75\ CO_2 + 2.67\ H_2O$ Equation 3.7 34

$0.02\ NH_4VO_3 + 0.25\ Mg(NO_3)_2.6H_2O + 0.25\ N_2H_4.H_2O + 0.25\ C_2H_5NO_2 + 0.2\ O_2 \rightarrow 0.01\ V_2O_5 + 0.25$

$MgO + 0.64\ N_2 + 0.5\ CO_2 + 2.93H_2O$ Equation 3.8 34

$0.02\ NH_4VO_3 + 0.25\ Mg(NO_3)_2.6H_2O + 0.25\ CO(NH_2)_2 + 0.25\ N_2H_4.H_2O + 0.01\ O_2 \rightarrow 0.01\ V_2O_5 +$

$0.25\ MgO + 0.76\ N_2 + 0.25\ CO_2 + 2.81\ H_2O$ Equation 3.9 34

$\text{Equivalence ratio} = \frac{\text{Fuel-oxidizer ratio}}{\text{Stoichiometric fuel to oxidizer ratio}}$ Equation 3.10 37

$Tad = T^0 + \frac{\Delta H\text{reactants} - \Delta H\text{products}}{Cp}$ Equation 3.11 38

$\boldsymbol{Cp} = \boldsymbol{\alpha} + \boldsymbol{\beta T} + \boldsymbol{\gamma}$ Equation 3.12 39

$\Delta H_{comb}^{o} = \Delta H_f^{o}$ (products) – ΔH_f^{o} (reactants) Equation 4. 1 60

$4MgO + 2V_2O_5 \rightarrow 2Mg_2V_2O_7 + O_2\,(g)$ Equation 4. 2 63

LIST OF ACRONYMS AND SYMBOLS

BET	:	Brunauer- Emmett- Teller
BF-TEM	:	Bright-field transmission electron microscopy
DF-TEM	:	Dark field transmission electron microscopy
DH	:	Dehydrogenation
EDS	:	Energy dispersive spectroscopy
EELS	:	Electron energy loss spectroscopy
FID	:	Flame ionization detector
GHSV	:	Gas hourly space velocity
GLY	:	Glycine
HAADF	:	High angle angular dark field
HH	:	Hydrazine hydrate
HCDF-TEM	:	Hollow-cone dark field transmission electron microscopy
HR-TEM	:	High resolution transmission electron microscopy
MvK	:	Mars and van Krevelen
ODH	:	Oxidative dehydrogenation
XRD	:	X-ray diffraction
REDOX	:	Reduction and oxidation
SCS	:	Solution combustion synthesis
SEM	:	Scanning electron microscopy
STEM	:	Scanning transmission electron microscopy
TCD	:	Thermal conductivity detector
TEM	:	Transmission electron microscopy
TPD	:	Temperature programmed desorption
TPD-MS	:	Temperature programmed desorption- mass spectroscopy
TPR	:	Temperature programmed reduction
UR	:	Urea

CHAPTER 1: INTRODUCTION

1.1 Background

Catalysts are highly valuable for their ability to drastically reduce reaction times and increase yields, making them a key tool in the chemical industry (Munnik *et al.,* 2015). Furthermore, catalysis has a wide range of applications in various areas of industrial production, including pharmaceuticals, polymers, and food additives (Basso and Serban, 2019). Many of the world's largest chemical corporations, such as Dow, Monsanto, DuPont, BASF, GE, and ICI, have sites dedicated solely to catalysis research and development (Cornils *et al*., 2017). Catalysis has a significant economic impact, accounting for 30–40 percent of the chemical industry's total market value as a percentage of global GDP. The development of more efficient catalysts will allow industrial processes to operate at lower temperatures, which will save money on energy costs, reduce the emission of hazardous materials, and increase the productivity of chemical processes which overall is gaining importance in energy conservation and, consequently, in the conservation of our natural resources (Ivankovic *et al.,* 2017). Catalysts can be modified to increase selectivity for desired products. The development of these greener, more viable methods demonstrates that the process of catalytic reactions can be made more selective and efficient, resulting in less waste and greater sustainability. Catalysis is a highly researched field, owing to the need to produce active catalysts with increased levels of conversion and selectivity to value added compounds. Catalysis is divided into two broad categories: heterogeneous and homogeneous catalysis.

1.1.1 Homogeneous catalysis

Homogeneous catalysis refers to the type of catalytic process where the catalyst and the reactants are in the same phase, typically in a liquid or gas form (Dibenedetto *et al.,* 2014). In this process, the catalyst dissolves or disperses in the reaction medium and interacts directly with the reactants to facilitate the desired chemical reaction (Climent *et al.,* 2012). These systems require higher heat transfer efficiency and can operate under milder conditions than in heterogeneous catalysis (De *et al.,* 2020). There is widespread use of homogeneous catalysts, such as in the hydrolysis of esters by acids and decomposition of potassium chlorate by MnO_2, as well as many others (Zhang *et al.,* 2021). However, there are certain challenges associated with homogeneous catalysis. One major drawback is the separation and recovery of the catalyst from the reaction mixture at the end of the process (Dreimann *et al.,* 2016). Since the catalyst is in the same phase as the reactants and products, it can be challenging to separate and reuse the catalyst, especially if it is expensive or toxic (Dreimann *et al.,* 2016).

1.1.2 Heterogeneous catalysis

Heterogeneously catalysed reactions involve the catalyst, products and reactants existing in different phases (Che *et al.,* 2012). Heterogeneous catalysis involves solid catalytic materials with reactants and products in liquid or gaseous phase, the processes typically using transition metals, transition metal oxides, zeolites, silica, and alumina catalysts (Vedrine, 2017). Most large-scale industrial catalytic processes fall within this category (Vedrine, 2017). The mechanism involved with heterogeneous catalysts is adsorption, which is a surface phenomenon that can be divided into two categories: physical adsorption (physisorption) and chemical adsorption (chemisorption) (Zhao *et al.,* 2020).

Physisorption involves relatively weak physical attraction forces, similar to Van der Waals forces, (Huber *et al.,* 2019). Chemisorption involves the formation of a chemical bond between the adsorbate and a surface and involves a substantial rearrangement of electron density (Lambert *et al.,* 2013; Dobrota and Pašti, 2020). Heterogeneous catalysis has at least four steps (Haber, 1994). Figure 1.1 illustrates the four-step process for heterogeneous catalysis.

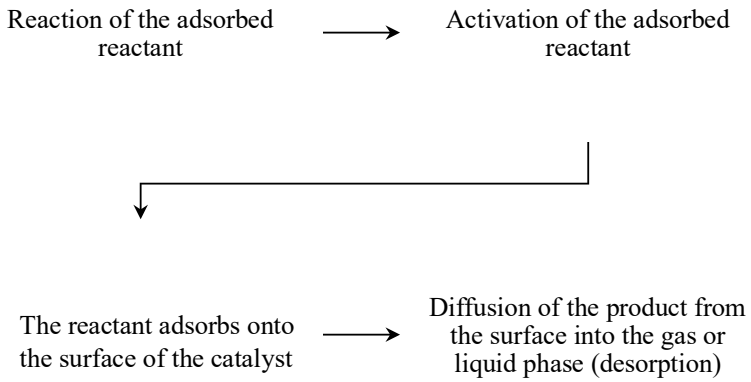

Figure 1.1**:** Scheme for the four-step process for heterogeneous catalysis (Haber, 1994)

Gas-phase reactions with heterogeneous catalysts start with the adsorption of reactant molecules on the surface of the catalyst, which means that hydrogen is adsorbed in the following reaction, breaking the H-H bond, and forming a M-H bond. An example of a gas-phase reaction is the hydrogenation of polyunsaturated fats and oils illustrated in Figure 1.2. Nickel is used in the hydrogenation of polyunsaturated fats and oils (Richardson, 1989). This interaction weakens the chemical bonds between the molecules of the reactants, which can lead to bond breakage and radical formation, and suggests that ethylene undergoes π bond cleavage to form a Ni-C bond. In addition, atoms diffuse across the surface and form new C-H bonds as they collide. Finally, the adsorbed product (C_2H_6) desorbs from the Ni surface and returns to the gas phase, leading to regeneration of the active site (Richardson, 1989).

$C_2H_4\,(g) + H_2\,(g) \longrightarrow C_2H_6\,(g)$ Equation 1. 1

The steps that occur in the reaction of compounds containing a carbon– carbon double bond with hydrogen on a nickel surface is illustrated in Figure 1.2 below.

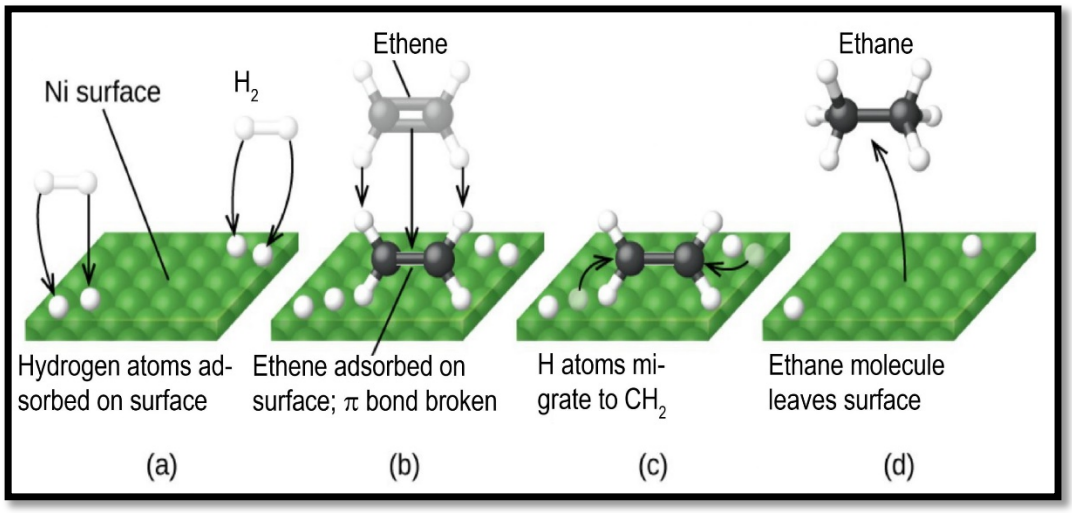

Figure 1.2: The hydrogenation of polyunsaturated fats and oils using Ni catalysts (Richardson, 1989)

In the context of the mechanism depicted in Figure 1.2, turning to kinetic studies is essential for understanding of the catalytic cycle's individual steps. Kinetic studies provide insights into the rate at which each step in the cycle occurs, which is crucial for determining how efficiently the catalyst operates. The reaction in question does not always proceed as outlined in the mechanism, leading to the formation of unwanted by-products such as CO_x. This deviation is likely due to the complex nature of the catalytic process, where multiple pathways might be possible, and various factors such as temperature and the presence of other compounds can influence the direction and rate of the reaction.

Chemisorption is the typical mechanism for this kind of intense interaction, which takes place between the reaction products and the active site (Huber *et al.,* 2019). Coking is a major factor in catalyst deactivation and is known to inhibit catalyst performance (Huber *et al.,* 2019). Heterogeneous catalysts are known to be complicated and can be categorized based on their pore size distribution, as well as the relative proportions of each component, shape, and size (Lambert *et al.,* 2013; Dobrota and Pašti, 2020). Meima and Menon (2001) discovered that a catalyst can have one or more active components, each with its own unique properties, their combination with those of other important materials producing synergistic effects.

1.1.3 Alkanes

The demand for functional alkenes and aromatics has increased significantly, resulting in the sourcing of various raw materials as an active area of study for many years (Bond *et al.,* 2014). Straight-chain alkanes are an abundant and relatively inexpensive source of hydrocarbons in the petrochemical industry. Alkanes are also easy to extract from natural gas and petroleum (Pedentchouk and Turich, 2018). Global gas-to-liquid plants produce 1 million tons of alkanes annually and will continue to do so. Alkanes are saturated hydrocarbons with the formula CnH_{2n+2} with strong sigma bonds. Carbon and hydrogen are equally electronegative because their C-H bonding atoms are shared. Alkanes and their properties have posed a challenge for researchers, specifically the various conditions that trigger their activation, such as high reaction temperatures and the type of oxide catalyst employed (Wang *et al.,* 2021). The evidence suggests that longer-chain alkanes are significantly more reactive than their shorter-chain counterparts (Pedentchouk and Turich, 2018). It's been theorised that *n*-octane is more reactive than hexane, butane, propane, and methane, and therefore requires lower activation temperatures (Ran, 2017). Alkanes that form a continuous chain without branching are referred to as linear alkanes and are identified by the number of carbon atoms that combine to form the chain. A carbon atom in a linear alkane can be either primary (bonded to only one other carbon atom) or secondary (bonded to two other carbon atoms). In this study, the linear alkane of interest is *n*-octane, the eight-carbon alkane.

1.1.4 Dehydrogenation

Catalytic dehydrogenation of alkanes is an endothermic reaction that can be represented by Equation 1.2.

$C_nH_2n_{+2} \rightarrow C_nH_2n + H_2$ Equation 1. 2

As the C-C bond strength is roughly 246 kJ/mol, which is much lower than the C-H bond strength of about 363 kJ/mol, the above reaction is highly unfavourable and cannot be carried out due to the cracking of the hydrocarbons (Bijani *et al.,* 2014). Nonetheless, with the help of a suitable catalyst, dehydrogenation can be accomplished with only a small amount of C-C bond cleavage (Bijani *et al.,* 2014). Metal or oxide catalysts activate strong C-H bonds through hydrogen abstraction, given their ability to form O-H bonds with equivalent strength to C-H bonds. As the M-H bond is much weaker than the C-H bond, metals cannot be used alone to achieve hydrogen abstraction (Kang *et al.,* 2019). This approach involves the activation of the M-H bond, subsequent transfer of the hydrogen to the M-C bond, and the eventual cleavage of the M-C bond to release hydrogen gas (Bijani *et al.,* 2014).

Dehydrogenation is highly endothermic, which leads to coke formation and catalyst deactivation to occur rapidly (Kang *et al.,* 2019). High temperatures during the dehydrogenation process increase the likelihood of unwanted reactions, and the need to regenerate the catalyst by burning out the coke with oxygen requiring additional energy (Satyanarayana *et al.,* 2016). There are four major limitations in dehydrogenation that need to be overcome with respect to developing a catalyst (Chen *et al.,* 2021). These are presented in Figure 1.3.

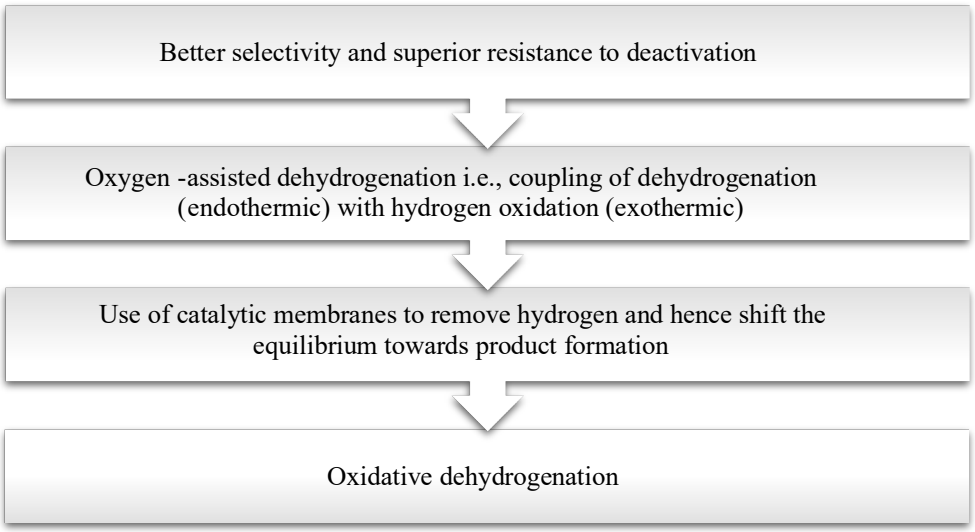

Figure 1. 3**:** Limitations of the prominent dehydrogenation technique (Chen *et al.,* 2021)

CHAPTER 2: LITERATURE REVIEW

2.1 Oxidative Dehydrogenation

The petrochemical industry currently relies heavily on olefins and aromatics as feedstocks, most of which are derived from the oil refining processes of steam cracking naphtha and fluid catalytic cracking (Karaba *et al.,* 2020). The Fischer-Tropsch processes used by Sasol produce large quantities of olefins and aromatics in South Africa (Dry, 1982). The ODH of paraffins to olefins and aromatics has the potential to revolutionize the production of a wide variety of essential organic chemicals (Vedrine *et al.,* 2016). There is an increased demand in the polymer for industry for olefins for both catalytic and steam cracking, which has led to a shortage of these valuable raw materials worldwide (Vedrine *et al.,* 2016). Since the late 1930s, olefins have been produced commercially through catalytic paraffin dehydrogenation (Chen *et al.,* 2021). There are various drawbacks to the catalytic dehydrogenation process, for example, side reactions such as cracking and coke formation are amplified, the catalyst's life is nearly halved, and regeneration is required (Chen *et al.,* 2021). Reactions are thermodynamically limited, and separating the desired products from by-products becomes more difficult (Dasireddy *et al.,* 2012). Limitations caused by catalytic dehydrogenation can be overcome by using ODH (Dasireddy *et al.,* 2012). During this reaction, oxygen reacts directly with the paraffin molecule on the catalyst surface (Wang *et al*, 2021). First, H^+ is removed from an organic molecule, and then another H^+ is removed from a neighbouring carbon atom, forming a double bond. Finally, water is removed from the molecule, as shown in Equation 2.1, demonstrating how "activation," changes an alkane into an alkene (Wang *et al*, 2021).

$C_nH_{2n+2} + 0.5O_2 \rightarrow C_nH_2n + H_2O$ Equation 2. 1

This reaction is thermodynamically favourable as it results in the formation of water. ODH yields olefins and water as by-products. Full conversion of these can be accomplished with relative ease, especially at low temperatures and high pressures. Doing so has environmental and economic benefits (Dasireddy *et al.,* 2012). As ODH reactions are exothermic and can operate at lower temperatures than their dehydrogenation counterparts, the formation of coke and cracked products is relatively insignificant, as is frequent catalyst degeneration (Samantaray *et al.,* 2019). The only significant limitation associated with ODH is the poor selectivity towards the desired products, as cracked products are typically more thermodynamically stable than the desired products (Carter *et al.,* 2021).

There is some evidence to suggest that using oxygen can help mitigate the amount of CO_2 and CO that is released during a reaction. Finding a way to reduce the harmful by-products or oxidizers produced by the catalyst is critical. The use of reactors presents a second challenge for ODH, and due to the high exothermicity of these reactions, extra precautions must be taken during operation to prevent the possibility of reaction runaway (Carter *et al.,* 2021). The catalysts for this reaction must possess active sites, which are either redox, acid-base or defect related properties.

2.1.1 Redox properties

In an ODH reaction, the catalyst, often a metal oxide or transition metal, must possess redox capabilities to effectively oxidize hydrocarbons and facilitate their reduction (Grant *et al.,* 2017). The gaseous oxygen utilized in the ODH reaction will then replenish the oxygen vacancies in the lattice created by the cations and re-oxidize (Al-Ghamdi and de Lasa, 2014), with the rate of this redox reaction being monitored and controlled. Prior research has established a correlation between redox potential and selectivity, particularly the reducibility of the mixed metal oxides (Wang, 2022). The ODH of alkanes to alkenes is known as a nucleophilic reaction which occurs when electrophilic oxidation attacks double bonds to form alkenes, leading to the formation of value-added products (Wang, 2022). Oxygen plays a crucial role in the ODH catalytic reaction, which follows the Mars and van Krevelen (MvK) mechanism and involves the breaking of C–H bonds with the participation of absent lattice oxygen species (Mars *et al.,* 1985). The schematic flow of reduction/oxidation on the surface of a catalyst obeying the MvK mechanism is presented in Figure 2.1

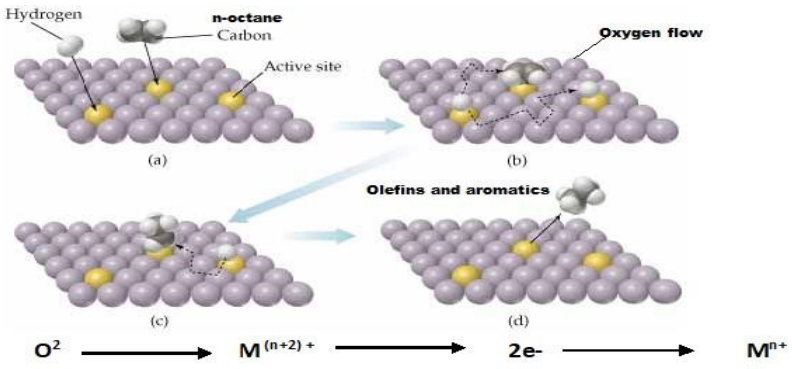

Figure 2.1: Cycle of reduction/oxidation on the surface of a catalyst obeying the MvK mechanism (Wang *et al.,* 2018)

A mixed oxide catalyst must be able to provide the necessary lattice oxygen for the ODH reaction to occur (Wang *et al.,* 2018**).** In the MvK mechanism, activated alkyl radicals are subjected to a nucleophilic addition of oxygen, which is followed by the elimination of the hydrogen atom (Najari *et*

al., 2021). The feedstock introduced into the system interacts with the catalyst, leading to the production of gaseous oxygen (Najari *et al.*, 2021). This enables the lattice oxygen to be replenished, which in turn prevents the catalyst from becoming inactive (Valverde *et al.,* 2003). The MvK mechanism faces limitations when the catalyst lacks redox properties, which prevents it from successfully activating an alkane feed (Yun *et al.,* 2018). In such situations, the acid-base properties of either the support material or the transition metal in a supported mixed oxide catalyst have the potential to activate the C-H bond (Vedrine, 2019).

2.1.2 Acid-base properties

The acid-base characteristics of an oxide catalyst can influence its behaviour, with the first step involving the activation of the alkane and the second involving the rate of adsorption and desorption of reactants and products (Vedrine, 2015). Selectivity is influenced by both the interaction of the products with the surface and the strength of the Lewis acid and base sites on the oxide catalyst (Johnson and Bell, 2016). A strong acidic oxidation product would be strongly adsorbed by a basic catalyst, and this interaction would increase the likelihood that the product would be completely oxidized to a carbon dioxide surface (Johnson and Bell, 2016). As a result, the use of an acidic catalyst would facilitate desorption of an acidic product, thereby enhancing the selectivity of the surface (Wu *et al.,* 2022). Similarly, catalysts with basic surfaces will preferentially allow desorption of basic products like olefins. In contrast, alkane activation can occur at acid-base sites. For this reason, the efficiency of a catalyst depends on the ratio of acid sites to base sites on its surface (Wu *et al.,* 2022). Some of these properties are discussed in detail by Gounden *et al* and are shown in Table 2.1 below.

Table 2. 1**:** List of catalysts used in ODH (Gounden *et al.,* 2014)

Type of catalysts	Examples
Redox catalysts	V_2O_5, MoO_3
Acid–base catalysts	H_2SO_4, HF, $AlSiO_2$
Poly-functional catalysts	$NiO\text{-}V_2O_6\text{-}MoO_3/Y\text{-}Al_2O_3$
CO transformation catalysts	Cu/Zn/Al/O based for MeOH

2.1.3 Selective oxidation on medium chain alkanes

Selective oxidation of saturated hydrocarbons with the range of 6-12 carbon atoms, known as medium chain were studied extensively by Cavani and Trifiro (Cavani *et al.,* 1999). Their research was specifically focused on the redox properties of mixed metal oxides on the oxidative conversion of alkane feedstocks. The authors observed the effect of a homogeneous reaction on non-redox-active metal oxides and the heterogeneity associated with the activation of these reactions. Lopez-Nieto and co-

authors investigated mixed vanadium catalysts and how their redox and acid-base properties affected the activity and selectivity of ethane, propane, and butane in ODH. They discovered that the acidic sites favour certain reaction pathways, while the basic sites could affect the stability of the intermediate species (Chieregato *et al.,* 2015; Del Campo *et al.,* 2021). There is a wealth of literature of the ODH of medium chain alkanes and of *n*-octane using materials synthesized by traditional synthesis methods such as wet impregnation and co-precipitation. However, very little attention has been given to the ODH of *n*-octane using materials synthesized by solution combustion synthesis.

2.1.4 Oxidative dehydrogenation of *n*-octane

Octenes and aromatics, are commonly used in the manufacturing process of various polymers, lubes, and adhesives. The conversion of saturated octenes and aromatics in catalysis is a complex process that involves challenges (Karaba *et al.,* 2020). These challenges include catalyst deactivation, selectivity, high energy consumption, safety issues, feedstock availability and incomplete conversion, with many research initiatives having been established to overcome these (Wei *et al*., 2020). Various researchers have used different catalytic systems, all to increase aromatic and olefin formation and decrease the formation of carbon oxides.

Fadlalla and Friedrich (2014) conducted the ODH of *n*-octane using molybdate-based catalysts, following a co-precipitation catalyst synthesis method (Fadlalla and Friedrich, 2014). The study focused on magnesium molybdate ($MgMoO_4$) and cobalt molybdate ($CoMoO_4$) based catalysts. In terms of catalytic behaviour, catalysts with near stoichiometric Mg:Mo (i.e. 0.98:1.06) demonstrated the highest *n*-octane conversion, particularly at high reaction temperatures (28% at 500 °C). With regard to the selectivity trend, increasing the molybdenum content in the catalyst decreased the selectivity to octene while increasing selectivity to aromatics and CO_x. Iso-conversion (24% at 500 °C), studies revealed that these catalysts were also the most selective for octenes (45%) and C8 aromatics (19%). The catalyst with the highest molybdenum trioxide content had the lowest selectivity for octene and C_8 aromatics.

Dasireddy *et al.* (2015) investigated the effects of the alkaline earth metal hydroxyapatite (HAp) on the *n*-octane ODH. Hydroxyapatite catalysts were more selective towards carbon oxides, followed by cracked products, octenes and aromatics. Sr-HAp showed superior selectivity and high turnover numbers for C8 products with the catalyst activating *n*-octane via the Eley-Rideal mechanism. The rate of product formation depends on the specific reaction rate, which is determined by the amount of oxygen chemisorbed on the catalyst surface. The acidity strength, product selectivity, and turnover numbers were as follows: Sr-HAp > Mg-HAp > Ca-HAp > Ba-Hap (Dasireddy *et al.,* 2015).

Gounden *et al*. (2014) investigated the oxidative activation of *n*-octane over titania-supported cobalt catalysts, revealing its strong potential for oxidative dehydrogenation due to a preference for dehydrogenation and dehydrocyclization pathways. The study identified octenes and aromatics as the primary valorization products, which were observed in variable quantities. The highest yield of value-added products (octenes and aromatics) was obtained at 550 ^{o}C at a feed ratio of 8:4, GHSV of 4000 h^{-1}, and a pellet size of 600-1000 um. The linear alkane *n*-octane retains its chain length without cracking after dehydrogenation and continues to aromatize over this catalytic system. The TiO_2 metal oxide support and the loaded Co_3O_4 metal can interact synergistically, resulting in the system's high activity in the oxidative dehydrogenation of *n*-octane (Gounden *et al.,* 2014). More recently, there has been use of vanadia-based materials have been used by various authors, as discussed in the following section.

2.1.5 Vanadia-based catalysts

The choice of the support material is important, as it can influence the overall catalytic activity, selectivity, and stability (Gärtner *et al.,* 2013). The support material often provides a high surface area and can help to disperse the active vanadium species evenly, thereby enhancing the catalytic performance (Gärtner *et al.,* 2013). Additionally, the interaction between vanadium and the support can lead to the creation of unique catalytic sites and electronic properties, which are essential for various chemical reactions (Langeslay *et al.,* 2018). Depending on the degree of assistance provided, the activity may be superior or inferior to that of the bulk vanadia, while the other cations in mixed oxides have a major impact on its reduction thermodynamics (Vedrine *et al.,* 2016).

In catalysis, vanadium oxide is typically supported on a metal oxide, such as TiO_2, ZrO_2, CeO_2, or MgO. These catalysts contain VO_x species that are thought to be active sites and exhibit excellent redox properties due to the presence of lattice oxygen in MgO (Taghavinezhad *et al.,* 2018). The presence of these oxygen vacancies facilitates the formation of active oxygen intermediates on the surface of the VO_x/MgO. Vanadium has sites which act as Lewis acids, while the surface sites of MgO serve as Lewis bases. VO_x supported on MgO possesses unique redox and acid base characteristics, which affect its activity, selectivity, and stability in ODH reactions (Taghavinezhad *et al.,* 2018). Catalyst supports are used to increase the surface area of the active compound and the mechanical stability of the catalyst, with vanadia selectivity and activity being significantly affected by the support material (Langeslay *et al.,* 2018).

2.1.6 Magnesium oxide as a support for vanadium

Magnesium oxide is a commonly used basic catalyst and its basic character is promoted by the O sites (Taghavinezhad *et al.,* 2018). Magnesium oxide has Mg^{2+} and five O ions in its structure, with the Mg^{2+} ions being strongly electropositive and the oxygen vacancies are anions (Taghavinezhad *et al.,* 2018). Sharp edges, kinks and corners on MgO structures contribute to its catalytic activity and are involved in the breaking of chemical bonds in an alkane (Gärtner *et al.,* 2013). As the surface of the metal oxide is predominantly acidic, the positively charged cations on the catalyst surface are known as "active sites" and are used for feedstock absorption which is an important step in the activation of alkane molecules in the presence of a catalyst (Gärtner *et al.,* 2013). The three known stable phases of magnesium vanadate can be altered by varying factors such as calcination temperature, heating rate and the presence of visible impurities in the mixed oxide that are formed during the preparation process (Gärtner *et al.,* 2013). These include magnesium orthovanadate ($Mg_3V_2O_8$), magnesium pyrovanadate ($Mg_2V_2O_7$), and magnesium metavanadate (MgV_2O_6) (Sushchenko *et al.,* 2017; Ntola *et al.,* 2022). The molecular structure of magnesium orthovanadate consists of MgO_6 units which is connected by a lone VO_4 tetrahedra.

The structure of magnesium orthovanadate is nearly cubic, with the magnesium atoms occupying octahedral sites and the vanadium atoms filling tetrahedral sites in oxygen atom layers (Tang *et al.,* 2016). Every oxygen atom is connected to vanadium and magnesium. The known phase *a*-$Mg_2V_2O_7$ is composed of V_2O_7 units that are attached to one another at the corners by VO_4 tetrahedra. The structure is made up of rows of these V_2O_7 groups, all of which contain vanadium-oxygen bridges in between (Misra and Andronenko, 2018). The oxygen atom that forms the shortest bond with the magnesium atom forms this bond with a magnesium atom; all the other oxygen atoms that are present in the V_2O_7 units each have two magnesium atoms attached to them (Pellizzeri *et al.*, 2017). MgV_2O_6 consists of VO_5 octahedra joined by edges and linked together by MgO_6 octahedra (Ikram *et al.,* 2021). The octahedra in VO_6 are highly distorted, similar to those in V_2O_5, therefore, the vanadium-oxygen bonds are ionic in nature and are less covalent in the pyrovanadate phase than in the orthovanadate phase, while the metavanadate phase is ionic rather than covalent (Ikram *et al.,* 2021).

Magnesium oxide has been used as a support for vanadium to synthesize VO_x/MgO catalysts. Tetrahedral vanadium species in the catalyst, cycling between V^{5+} and V^{4+} through reduction-oxidation processes, are identified as the most active components in facilitating the reaction (Rostom, 2018). The phases in which these active centres are found are still unknown since many researchers have had conflicting opinions. Some researchers suggested that the magnesium orthovanadate phase is the most selective (James *et al.,* 2016) while others have argued that it is the magnesium pyrovanadate phase

(Rostom, 2018). The incorporation of the vanadium in the MgO with equal distribution and dispersion, inclusive of both orthovanadate and pyrovanadate phases being present in each catalyst, plays an important role in both selectivity and reactivity (Marcu *et al.,* 2017).

The two most active phases of VO_x/MgO for the ODH of paraffins are the magnesium pyrovanadate ($Mg_2V_2O_7$) and magnesium orthovanadate ($Mg_3V_2O_8$) phases (Ntola *et al.,* 2021). Although the coexistence of both phases is regarded as optimal for catalytic performance, there are different views regarding the selectivity of each phase, with a catalyst's single phase performing at a subpar level (Marcu *et al.,* 2017). Figure 2.2 shows that the V_2O_5 crystallites formed bonds with the OH^- groups on the MgO support.

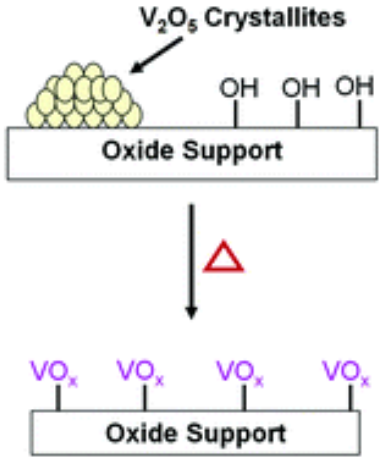

Figure 2.2: Schematic representation of V_2O_5 nanoparticle formation on top of a surface vanadia monolayer on an oxide support (Wachs, 2013)

2.1.7 VO_x/MgO catalysts on short chain alkanes

Chao and Ruckenstein (2004) investigated the oxidation of ethane using a VO_x/MgO catalyst under non-catalytic conditions at elevated temperatures. The non-catalytic thermolysis process with the aid of a catalyst displayed enhanced conversions and selectivity rates of ethane to ethene, accompanied by large carbon deposits. At low temperatures, homogeneous reactions contributed less to the ODH of ethane. Alcohol, aldehydes, ketones, and acids are among the by-products of non-catalytic reactions. Under catalytic conditions, a higher fraction of the feed was converted to oxygenates, with higher selectivity for formaldehyde at comparable conversions than under non-catalytic conditions (Chao and Ruckenstein, 2004). In a study by Govender et al. (2007) on the ODH of propane using VO_x/MgO catalysts, it was reported that the $Mg_3(VO_4)_2$ phase exhibited higher selectivities towards the formation of propene compared to the $Mg_2V_2O_7$ phase. The redox behaviours of these phases were investigated, highlighting their influence on catalytic efficiency and selectivity. By purging the reactor with nitrogen

initially, lattice oxygen was removed from the catalyst, allowing oxygen to subsequently interact with it. This resulted in a decrease in selectivity towards the formation of the desired products and an increase in selectivity towards oxidation products in the $Mg_2V_2O_7$ pyrovanadate phase. Conversely, the $Mg_3(VO_4)_2$ orthovanadate phase demonstrated greater selectivity towards propene.

2.1.8 VO_x/MgO catalysts for medium-chain alkanes

To investigate the aromatization of *n*-hexane, Chetty et al. (2017) studied vanadium magnesium oxide with varying vanadium loadings prepared using the wet impregnation method. MgO and $Mg_3(VO_4)_2$ were the only phases observed in each catalyst. The by-products formed over the VO_x/MgO catalysts were benzene, 1-hexene, 2-hexene, propane, propene, CO_x and H_2O. The most effective catalyst was the VO_x/MgO with a vanadium loading of 19 wt.%, which demonstrated that their combination facilitated the increased production of olefins and aromatics. The synergistic effect of the two phases improved the catalyst's efficiency, in the presence of limited oxygen in the system. Its surface therefore became saturated with reactive paraffin molecules, resulting in non-selective reactions (Chetty *et al.,*2017)

Dasireddy et al. (2015) conducted a study on the activation of *n*-heptene using vanadium oxide supported on alkaline earth hydroxyapatites. These were also prepared using the wet impregnation method. The catalytic results demonstrated that the product selectivity is determined by the phase of vanadium that is present on the HAp catalysts, and that the conversion rate is directly proportional to the quantity of chemisorbed oxygen that is present on the surface of the catalyst. Over the HAp support, carbon oxides were the primary products, whereas heptene isomers were the primary products over the VO_x/HAp catalyst, followed by heptene isomers, aromatics, and oxygenate products, 2-heptene, toluene, and 2-heptanol. The optimal activation position of *n*-heptene was determined to be C_2, followed by C_3 and C_1. The C_1-C_6 cyclization of 1-heptene led to the formation of toluene, the most abundant aromatic product (Dasireddy *et al.* 2015).

2.1.9 VO_x/MgO catalysts on the ODH of *n*-octane

Elkhalifa and Friedrich, (2014) conducted the ODH of *n*-octane over V/MgO catalysts. These catalysts were synthesized by impregnating magnesium oxide with an aqueous solution of ammonium metavanadate. When the *n*-octane concentration exceeded 19 wt%, the major products formed were octenes, octadienes, octatrienes, benzene, ethylbenzene, styrene, o-xylene, carbon monoxide, and water. The direct conversion of *n*-octane to styrene has the potential to be an appealing commercial process, making styrene a particularly desirable product. The maximum styrene selectivity and yield were attained by optimizing the process conditions to 22% and 15%, respectively, with the most effective

catalyst being the V/MgO catalyst with a vanadium loading of 19 wt%, which demonstrated that the coexistence of precise quantities of MgO and $Mg_3(VO_4)_2$ was advantageous for the increased production of aromatics (Elkhalifa and Friedrich, 2014).

Padayachee et al., 2019 studied the activation of *n*-octane using a variety of catalysts, including mixed metal oxide catalysts, under a range of reaction conditions. Octene isomers serve as intermediates in the synthesis of C8 aromatics, ethyl benzene, styrene, and o-xylene, which can also result in the undesirable compound CO_x. C8 aromatics formed via C_2-C_7 dehydrocyclization are useful compounds for many reactions, while ethylbenzene is used as a feedstock for styrene and in other chemical processes. The petrochemical industry relies heavily on styrene, a monomer that plays a significant role in many processes (Padayachee *et al.,* 2019). Elkhalifa *et al.* (2011) also used V/MgO catalysts for *n*-octane activation following the wet impregnation method. Catalysts were synthesized with varying vanadium loadings, which affected both their textural and chemical properties. At all vanadium loadings, crystalline $Mg_3V_2O_8$ was formed, whereas crystalline $Mg_2V_2O_7$ was detected only at high vanadium concentrations of 50 wt. % V/MgO. The reduction and re-oxidation of the catalyst improved as the vanadium loadings increased. In addition to carbon oxides, the partial oxidation of *n*-octane over V/MgO catalysts produced primarily octene, styrene and ethylbenzene, and to a lesser extent xylene, as well as some cracking products. The dominant octane isomer was 2-octene, while 50 wt. % V/MgO had the highest octene selectivity and the lowest aromatic selectivity (Elkhalifa *et al.,* 2011).

Elkhalifa and Friedrich (2014) studied the ODH of *n*-octane using V/MgO catalysts prepared from various Mg precursors, using wet impregnation. Changing the MgO precursor and treatment resulted in changes in the textural and chemical properties of the resulting V/MgO catalysts, including crystallite sizes, vanadium dispersion, reducibility and surface acidity. Vacuum treatment of the support precursor resulted in catalysts with rough surfaces and relatively better catalytic performance. The preparation method of the support influenced the properties and catalytic performance of the V/MgO system (Elkhalifa and Friedrich, 2014). Elkhalifa *et al.* (2011) studied the effects of varying concentrations of *n*-octane in the feed. The results demonstrated that the catalytic performance was sensitive to changes in the *n*-octane concentration. At 500 and 550 °C, with a C:O molar ratio of 8:10, the maximum conversion was 80 mol%. Over the entire range of investigated C:O molar ratios, the highest CO_x selectivity of 80 mol% corresponded to the highest conversion. No phase changes were observed in any of the catalysts, indicating their stability under the experimental conditions (Elkhalifa *et al.*, 2011). A variety of synthesis methods have been used for the preparation of this system, including solution combustion synthesis.

2.2 Solution Combustion Synthesis (SCS)

Solution combustion synthesis (SCS) is a simple, cost-effective, and sustainable synthesis method for synthesizing advanced materials with narrow size distributions and adjustable properties (Carlos *et al.,* 2020). There have been extensive investigations into the SCS method and the properties of mixed metal oxides, with numerous research efforts having been successful in creating nanocrystalline solids (Shinde and Jun, 2020). Figure 2.3 shows the various industries that use SCS produced nanomaterials, such as electronics for semiconductor production, energy for catalysts and battery components, biomedical materials for drug delivery systems and imaging, automotive materials for high-performance coatings and sensors, aerospace for structural materials and thermal barriers, environmental materials for pollution control and filtration, and materials science for advanced ceramics and composites (Parauha *et al.,* 2021).

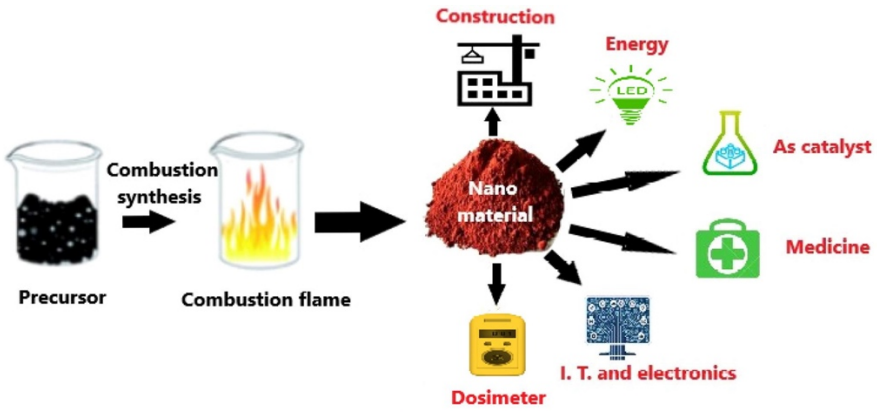

Figure 2.3**:** List of industries that use SCS-produced nanomaterials (Parauha *et al.,* 2021)

The SCS process uses extremely high temperatures, which results in the mixed metal oxide being porous, with a higher purity and larger surface area (Wen and Wu, 2014). Calcination, which is typically the final step of most synthesis techniques, can be omitted when utilizing SCS, as the final composition has already been attained (Varma *et al.,* 2016). This method also causes large gas changes over short periods of time, which stops the particle size from increasing (Gonzalez and Imbert, 2013). Most SCS preparations are usually conducted via a single fuel approach, with little attention given to the mixed fuel approach. Figure 2.3 shows a schematic flow of the SCS process.

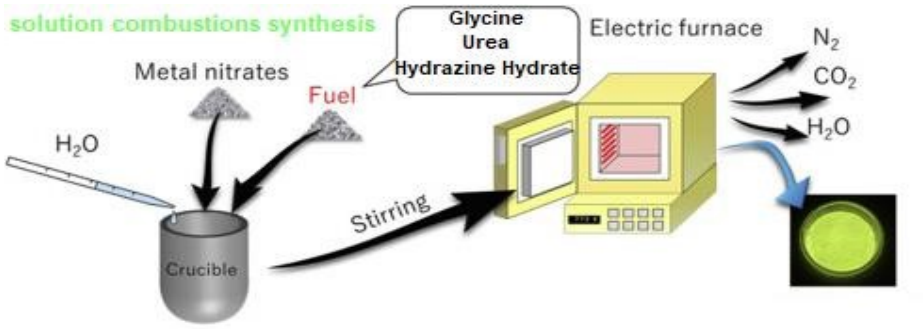

Figure 2.4: Schematic flow of the SCS process (Gotoh *et al*., 2020)

The selected fuel rarely provides sufficient heat for a complete conversion of the oxidizers, such as nitrates, to the desired phase, although by combining the fuels, sufficient energy is available during combustion for complete crystallization (Thoda *et al.,* 2018). Due to the simplicity of the synthesis route and the fast reaction rate, SCS is regarded as an attractive method for catalyst production (Thoda *et al.,* 2018).

2.2.1 Single-fuel approach

In a study by Bai et al. (2011), MgO catalysts were synthesized using magnesium nitrate as the oxidizer and soluble starch as the fuel (Bai *et al.,* 2011). The authors reported that nanoporous agglomerates were formed in the powders when the weight percent of starch increased. It was also observed that the nanocrystalline size of the MgO increased, while the average particle size decreased significantly, which was linked to the amount of starch fuel used.

Pathak and Swart, 2019 synthesized ZnO using a single-fuel SCS. The aim of their studies was to determine the structure and luminescence of ZnO nanoparticles. A large surface area was observed for each catalyst without the need for calcination (Bai *et al.,* 2011; Pathak and Swart, 2019). Toniolo et al., reported that glycine-nitrate and urea-nitrate are the best combinations for preparing cobalt oxide powders. Under fuel-rich conditions, glycine produced metallic cobalt powder, while the combination of urea and glycine, both of which are fuel-rich, produced cobaltous oxide phases. In a Bunsen-heated stainless-steel container, cobalt nitrate-glycine and cobalt nitrate-urea water solutions were prepared. As a result, the smallest crystallite size obtained was 23 nm, and the highest specific surface area achieved was 36 m^2/g for fuel-lean reactions using glycine as a fuel. Combustion reaction thermodynamic modelling demonstrates that an increase in the fuel-to-oxidant ratio results in a greater amount of gas produced and a hotter adiabatic flame which can influence phase formation (Toniolo *et al.,* 2010).

2.2.2 Mixed fuel approach

The concept of fuel mixture was first established in 2004 by Bai *et al.* (2011). Since then, various researchers have successfully used the SCS method with different fuel mixtures to obtain single or multicomponent oxide nanoparticles (Kopp *et al.,* 2013). In a study on mixed fuels by Sasikumar *et al.,* (2008), the auto-ignition temperature of succinic acid was reduced from 425 ^{o}C to 290 ^{o}C by the addition of citric acid. Bai et al. (2011) pioneered a mixed fuel approach in 2004. Nanoscale $MgAl_2O_4$ powders were synthesized using a microwave-assisted solution combustion process with various mixtures of urea, glycine and starch. The addition of starch altered the catalyst specific surface area and crystallite size of the powders, and the specific surface area of the powders increased significantly with the starch addition level but reached a saturation point and decreased after a certain percentage (Kopp *et al.,* 2013; Sasikumar *et al.,*2008; Bai *et al.,*2011).

The effect of mixing fuels using the SCS method for the preparation of Al_2O_3 was studied by Sherikar et al. (2012). The study demonstrated that the powders that formed produced polycrystalline oxides with ranging crystallite sizes ranging from 81 nm for alpha alumina to ~ 5 nm for gamma alumina, with all the catalysts displaying a porous microstructure. Six samples were synthesized using various fuel-to-oxidizer ratios and mixtures of the two fuels, with urea promoting the product's crystalline nature, while glycine promoted its amorphous nature. Mixed fuel enhances crystallinity without the need for calcination, while the single fuel glycine influences particle size. Urea single fuel permits a high flame and particle agglomeration (Sherikar *et al.,*2012).

2.2.3 Fuel selection for the mixed fuel approach

Ntola *and* co-authors explored the role of fuel selection on the micro-structure of SCS-synthesized VO_x/MgO catalysts (single fuel approach), and found that glycine, urea and hydrazine hydrate produced catalysts that were selective towards olefins and aromatics (Ntola *et al*., 2022, Ntola *et al.,* 2023). Both urea and hydrazine hydrate had particle sizes >10 nm, with the former exhibiting well-defined faceted particles were observed. The catalyst synthesized using glycine fuel had a round, porous morphology, which indicates a preference for greater selectivity. The optimal order of fuels for increasing MgO crystallite size is glycine, urea and hydrazine hydrate, with the magnesium vanadate phases being present in all three catalysts. It was also established that the magnesium vanadate phase can form between temperatures of 800-1500 ^{o}C, with the magnesium orthovanadate and magnesium pyrovanadate phases being able to form within that temperature range (Zhou *et al*., 2014). The SCS system therefore enables the temperature to reach that range for optimal phase formation. The more time spent at that temperature, the greater the segregation of Mg and V in each phase (Gonzalez and

Imbert, 2013). In comparison to single fuels, fuel mixing produces an ideal temperature, with hydrazine hydrate and glycine being high combustion fuels individually, while mixing them with urea will allow a lower adiabatic temperature that gradually increases over time. This will allow sufficient time for the formation of the above-mentioned phases (Ntola *et al.,* 2022).

2.3 Aim and Objectives

Aim

The aim of the study was to synthesize VO_x/MgO catalysts for the ODH of *n*-octane using mixed fuel solution combustion synthesis.

Objectives

1. To synthesize VO_x/MgO catalysts using mixed fuel solution combustion synthesis.
2. To characterize the synthesized catalysts using ICP-OES, HRTEM and SEM, XRD and Rietveld refinement, BET, TPR and TPD.
3. To test the effects of the catalysts on the ODH of *n*-octane.

CHAPTER 3: RESEARCH DESIGN: EXPERIMENTAL

This chapter deals with the synthesis of VO_x/MgO catalysts using the SCS method. In this method, a select mixture of fuels was used, viz; (GLY/UR), (UR/HH), and (GLY/HH). Catalyst preparation was followed by a set of characterization techniques that were used to evaluate the physicochemical properties of the catalysts. For the first time, VO_x/MgO catalysts were prepared by a mixed-fuel solution combustion synthesis approach.

3.1 Solution combustion synthesis parameters

There are three parameters of the SCS reaction that strongly affect the morphology and composition of the synthesized powders: the fuel type, oxidant type and the fuel-oxidant ratio.

3.1.2 Fuel type

Studies have reported that the structure and/or surface properties of the final product obtained via SCS are affected not only by the nature or type of fuel, but also by the fuel-to-oxidizer ratio (Kang *et al.,* 2018). An effective fuel in the SCS is characterized by the following characteristics (Deganello *et al.,* 2018):

- Usually soluble in water; however, organic solvents can also be used to improve fuel solubility.
- Act as metal dispersing and/or complexing agent that would form a new metal–fuel precursor.
- Melting point usually below 250 ^{o} C, with an ignition temperature of below 500 ^{o}C. Usually fully decomposed, evolving large amounts of gases that would improve catalyst textural properties

3.1.3 Oxidant type

Typical oxidants are metal salts such as nitrates, sulphates, and carbonates. Nitrate metal precursors are most commonly used due to their high water solubility (Deganello *et al.,* 2018).

3.1.4 Fuel-Oxidant ratio

The fuel-oxidant ratio determines the rate at which solutions undergo combustion, with a ratio of 1 indicating that the solution mixture is stoichiometric ($\varphi = 1$). This implies that there are equal parts of both precursors and fuels in the sample mixture (Wang *et al.,* 2021). The combustion reaction will gradually burn with a luminous flame and reach an ideal temperature that can be calculated theoretically

(Varma *et al.,* 2016). A method was developed for calculating the oxidizing valency (OV) of the oxidants and the reducing valency (RV) of the fuels in a redox reaction mixture (Frikha *et al.,* 2020). From this, the fuel-oxidant ratio (φ) of the redox mixture is calculated (Varma *et al.,* 2016).). The relationship between the number of moles of a reactant and its reducing and oxidizing valency (RV/OV) is shown in Equation 3.1.

$$\varphi = \frac{(-1).RV}{OV}\ n \qquad \text{Equation 3.1}$$

The fuel-oxidizer ratio φ is determined by the balance between the reducing agent (fuel) RV and the oxidizing agent OV, with 'n' adjusting the ratio to suit specific reaction conditions. The overall oxidizing or reducing valence is calculated as the sum of the elemental valences of the molecule. The elemental oxidizing and reducing valences are presented in Table 3.1 (Varma *et al.,* 2016).

Table 3.1: Elements and their oxidizing/reducing valences (Varma *et al.,* 2016).

Element	Oxidizing/Reducing Valence
C	+4
N	0
H	+1
O	-2
V	+5
Mg	+2

The oxidizing valence of the precursors were calculated according to equations 3.2 and 3.3.

OV-$Mg(NO_3)_2.6H_2O$ = 1Mg = +2; 2N = 0; 6O = -12; $6H_2O$ = -10 Equation 3.2

Note that hydration water does not affect the overall compound valence (Varma et al., 2016)

OV-NH_4VO_3 = 1V = +5; 1N = 0; 4H = +4; 3O = -6 = +3 Equation 3.3

The reducing valence of the fuels used were calculated according to equations 3.4, 3.5 and 3.6.

RV-$C_2H_5NO_2$ = 2C = +8; 5H = +5; 1N = 0; 2O = -4 = +9 Equation 3.4

RV-$CO(NH_2)_2$ = 1C = +4; 1O = -2; 2N = 0; 4H = +4 = +6 Equation 3.5

RV- $N_2H_4.H_2O$ =2N = 0; 6H = +6; 1O = -2 = +4 4 Equation 3.6

3.1.5 Mixed Fuel approach

In the preparation of VO_x/MgO catalysts and MgO supports using mixed fuel SCS, the selection of different fuel mixtures plays a critical role in influencing the reaction dynamics and the properties of the synthesized material (Xanthopoulou *et al.,* 2018). The UR/HH mixture combines the relatively slow and controlled release of energy from urea with the more reactive and rapid decomposition of hydrazine hydrate (Deganello *et al.,* 2018). The GLY/UR mixture integrates the moderate combustion characteristics of urea with the additional complexing ability of glycine. Glycine is known to complex with metal ions, potentially leading to a more homogeneous distribution of the reactants and influencing the morphology of the final product (Deganello *et al.,* 2018). Equations 3.7, 3.8 and 3.9 depict the equations for the VO_x/MgO catalysts prepared from the fuel mixtures.

$0.02\ NH_4VO_3 + 0.25\ Mg(NO_3)_2.6H_2O + 0.25\ CO(NH_2)_2 + 0.25\ C_2H_5NO_2 + 0.33\ O_2 \rightarrow 0.01\ V_2O_5 + 0.25\ MgO + 0{,}64\ N_2 + 0.75\ CO_2 + 2.67\ H_2O$ ($\varphi > 1$) Equation 3.7

$0.02\ NH_4VO_3 + 0.25\ Mg(NO_3)_2.6H_2O + 0.25\ N_2H_4.H_2O + 0.25\ C_2H_5NO_2 + 0.2\ O_2 \rightarrow 0.01\ V_2O_5 + 0.25\ MgO + 0.64\ N_2 + 0.5\ CO_2 + 2.93H_2O$ ($\varphi > 1$) Equation 3.8

$0.02\ NH_4VO_3 + 0.25\ Mg(NO_3)_2.6H_2O + 0.25\ CO(NH_2)_2 + 0.25\ N_2H_4.H_2O + 0.01\ O_2 \rightarrow 0.01\ V_2O_5 + 0.25\ MgO + 0.76\ N_2 + 0.25\ CO_2 + 2.81\ H_2O$ ($\varphi = 1$) Equation 3.9

A stoichiometric mixture (φ=1) does not require atmospheric oxygen for complete fuel oxidation, while φ >1 (or φ <1) corresponds to fuel-rich (or lean) conditions (Riahi *et al.,* 2017). The fuel type and fuel content mainly influence the combustion behaviour, phase, morphology, and specific surface area of the as-combusted powders (Karami *et al.,* 2021). The adiabatic temperature (Tad), which is the temperature that a combustion process would reach if no heat was lost to the surroundings, depends on the fuel type and the fuel to oxidant molar ratio (φ). The stoichiometric mixture (φ =1) shows the maximum adiabatic temperatures of 2297 K and 2127 K for the glycine and urea fuels, respectively (Fathi *et al.,* 2017). However, Tad decreases steadily for either leaner or richer mixtures because of the need to heat up either the excess reactants or products (Martirosyan *and* Mukasyan*,* 2014). Furthermore, a higher fuel content and greater release of gas led to a more intense exothermic reaction, releasing more energy which can affect the porous structure and surface area (Fathi *et al.,* 2017). According to combustion chemistry, the released gaseous products are mainly CO_2, H_2O, N_2 and O_2 for φ <1 because of excess oxidants, while the O_2 gas vanishes and the H_2 and CO gases appear for φ >1 in fuel-rich environments (Martirosyan and Mukasyan*,* 2014).

The above molar amounts for the fuels were chosen to find a balance between CO_2 formation which can lead to formation of carbides. This includes oxygen production/consumption during the reactions,

therefore keeping the molar amounts of the fuels consistent across the three reactions was imperative in minimising the possibility of forming side reactions. In this study, VO_x/MgO powders were synthesized using three different fuels, glycine, urea and hydrazine hydrate. Glycine is a metal complexing agent due to the presence of a carboxylic acid group on one side of the molecule and an amino group on the other (Broeksma, 2018). The magnesium nitrate precursor and ammonium metavanadate precursor react with the amino group of the urea molecule in an acidic environment, forming a complex involving the nitrate anion (Deganello *et al.,* 2018). As the gelation suppresses the salting out of the solution's constituents during evaporation, a homogeneous solid is left behind (Deganello *et al.,* 2018).

3.1.6 Catalyst preparation

Compositions of the metal nitrates (oxidizers) and fuel (reducers) were calculated based on their total oxidizing and reducing valences. These valences contribute to stoichiometric balance, ensuring that the equivalence ratio (φ) equals unity and that the energy released during combustion is maximized (Fathi *et al.,* 2017). The SCS process begins with the dissolution of ammonium metavanadate (NH_4VO_3) in 50 ml of water, to which magnesium nitrate Mg $(NO_3)_2 \cdot 6H_2O$ is added followed by the addition of the fuel mixtures GLY/UR, GLY/HH and UR/HH. Good mixing of fuels is essential because it significantly influences the combustion dynamics and the uniformity of the final product (Fathi *et al.,* 2017). The mixture was then subjected to a thermal treatment in a muffle furnace for approximately 3 hours. This stage facilitates an exothermic reaction leading to the formation of a nanoporous powder, a process which is key for the material's microstructural development. The final step involves calcining the powder at 500 °C, which is crucial for enhancing the crystallinity of the material and modifying its physicochemical properties. After synthesis, the powder was ground to optimize its particle size. Figure 3.1 depicts the schematic flow of the catalyst sample preparation process using the mixed-fuel approach.

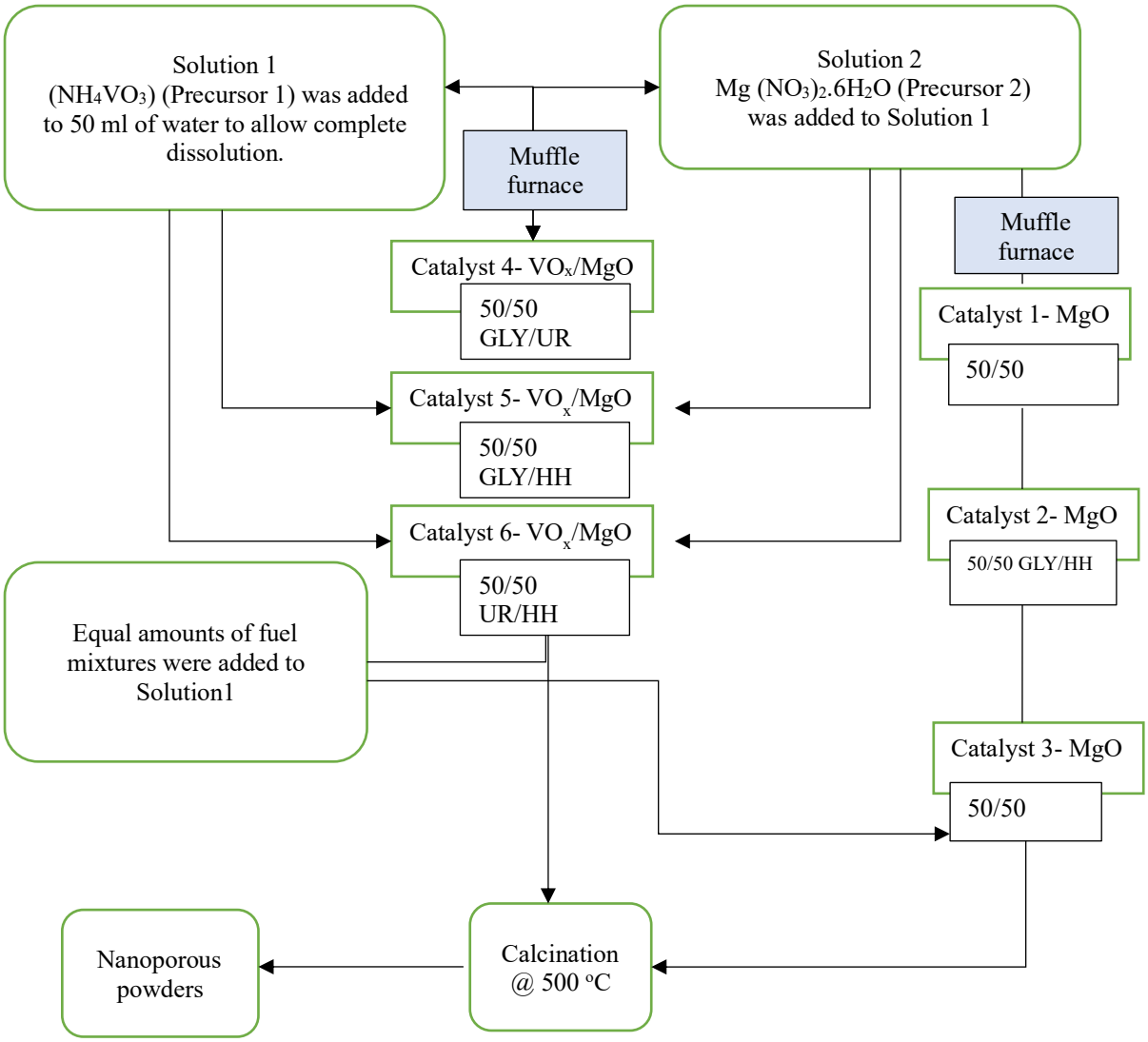

Figure 3.1**:** Schematic flow of the SCS process for the preparation of MgO and VO_x/MgO powders

3.1.7 Synthesis of the MgO supports

The MgO supports were prepared by mixing stoichiometric amounts (φ=1) of $Mg(NO_3)_2 \cdot 6H_2O$ (Merck, 99%) with stoichiometric fuel mixtures (50/50) GLY/UR, GLY/HH and UR/HH. (Figure 3.1). These mixtures were placed in a muffle furnace at 400 ºC. The solution containing the redox mixtures ignited, foamed, and burnt with a luminescent flame to form MgO, with the evolution of large amounts of gases at φ = 1.0. The catalysts were placed in a calcination furnace at 500 ºC to form a white nanoporous powder. The quantities of precursors were calculated to achieve a target of 12 g for each catalyst. Depending on the nature of the combustion reaction, the masses obtained were 11.2 g, 11.5 g and 11.5 g with a yield of 93-96%.

3.1.8 Catalyst preparation for VO_x/MgO catalysts

The VO_x/MgO catalysts with 15% (wt.) V_2O_5 were prepared by heating an aqueous redox mixture containing amounts of ammonium metavanadate (NH_4VO_3) (Sigma Aldrich, 99.99%) and magnesium nitrate hexahydrate (Mg $(NO_3)_2 \cdot 6H_2O$). The fuel mixtures used were (50/50) glycine and urea (GLY/UR), glycine and hydrazine hydrate (GLY/HH) and urea and hydrazine hydrate (UR/HH). The mixtures were placed in a muffle furnace at 400 ºC. The solution containing the above redox mixture reached the boiling point, foamed, ignited, and burned with luminescent flame-forming gases. These were then calcined at 500 ºC to form a nanoporous yellow metal oxide. The quantities of precursors were calculated to achieve a target of 15% by weight of V_2O_5, aiming to produce 12 g of the catalyst. Depending on the nature of the combustion reaction, the masses obtained were 11.5 g, 11.4 g and 11.7 g with a yield of 95-97.5%. The exact quantities of metal nitrate salts and the corresponding organic fuels that were weighed are shown in Table 3.2.

Table 3.2**:** Quantities of metal nitrate salts and fuel compositions

Catalyst	**NH_4VO_3 (g)**	**$MgNO_3.6H_2O$ (g)**	**$C_2H_5NO_2$ (g)**	**$N_2H_4.H_2O$ (g)**	**CH_4N_2O (g)**	**Fuel ratio (by moles)**
1-MgO	0	38	8.1	0	6.6	50/50
2-MgO	0	38	11.8	5.5	0	50/50
3-MgO	0	38	0	5.5	10.5	50/50
4-VO_x/MgO	2.3	64.9	18.6	0	14.9	50/50
5-VO_x/MgO	2.3	64.9	18.6	12.6	0	50/50
6-VO_x/MgO	2.3	64.9	0	12.6	14.9	50/50

The equivalence ratio represents the ratio of the actual fuel-to-oxidizer ratio to the stoichiometric fuel-to-oxidizer ratio required for complete combustion. It can be calculated using the following formula:

$$Equivalence\ ratio = \frac{Fuel-to-oxidizer\ ratio}{Stoichiometric\ fuel-to-oxidizer} \qquad \text{Equation 3.7}$$

The stoichiometric ratio is the theoretical amount of fuel needed to completely react with the oxidizer to form the desired product. If φ = 1, the mixture is stoichiometric, implying that all the fuel reacts completely with the oxidizer, leaving no excess of either component. These are presented in Table 3.3. These equivalence ratios provide insights into the stoichiometric proportions of the reactants in the combustion process. Adjusting the reactant ratios based on these values can help optimize the combustion efficiency and product yield. The reaction stoichiometry is instrumental in determining the properties of the synthesized materials according to specific application requirements, including phase composition, particle size, morphology, homogeneity, and thermal stability (Fathi *et al.,* 2017). A positive equivalence ratio indicates a fuel-rich mixture. In such cases, there is an excess of fuel relative

to the stoichiometric amount required for complete combustion with the available oxidizer. This excess of fuel can lead to incomplete combustion, where some of the fuel may remain unreacted or partially react (Varma *et al*., 2016). Table 3.3 shows that the addition of V_2O_5 slightly decreased the equivalence ratios of the fuels. A negative equivalence ratio indicates a fuel-lean mixture. Here, there is an insufficient amount of fuel relative to the stoichiometric amount required for complete combustion with the available oxidizer. In fuel-lean mixtures, the oxidizer is in excess, leading to incomplete combustion due to the lack of sufficient fuel to react with all the oxidizers present (Varma *et al*., 2016).

Table 3.3**:** Calculated values of the equivalence ratios (φ)

Precursor	**φ-V_2O_5+MgO**	**φ-MgO**
NH_4VO_3 (g)	+0.24	0
$MgNO_3.6H_2O$ (g)	-9.76	-10
$C_2H_5NO_2$(g)	1.08	1.11
$N_2H_4.H_2O$(g)	2.44	2.5
CH_4N_2O (g)	1.63	1.66

3.1.9 Adiabatic temperature

Reactions driven by combustion are characterized by their ability to reach high temperatures within a minimal time frame (Varma *et al*., 2016). Therefore, assuming that a thermally isolated system exists because there is very little time for the heat to disperse to its surroundings (Varma *et al*., 2016). Therefore, the maximum temperature achieved by the reaction products is assumed to Tad (Varma *et al*., 2016), which can be calculated using the room temperature in K, enthalpy of change for reactants (denoted as a negative value), enthalpy of change for products (denoted as a positive value), and heat capacity at constant pressure of each product formed which is expressed in Equation 3.11

$$Tad = T^0 + \frac{\Delta Hreactants - \Delta Hproducts}{\mathrm{Cp}} \qquad \text{Equation 3.8}$$

Where T_{ad} is the adiabatic temperature in K; T^0 is 298 K; $\Delta H_{reactants}$ and $\Delta H_{products}$ are the standard enthalpies of formation of reactants and reaction products in kJ/mol, respectively; and C*p* is the heat capacity of reaction products at constant pressure in kJ/molK. Cp is typically expressed as a function of temperature by a quadratic polynomial expression (Schauermann and Freund, 2015).

Equation 3.12: suggests that the heat capacity (Cp) is a function of temperature (*T*) and can change with temperature. The terms $\alpha\alpha$, $\beta\beta$, and $\gamma\gamma$ represent the coefficients of linear, quadratic, and cubic temperature dependence, respectively.

$$Cp = \alpha + \beta T + \gamma T^2$$ Equation 3.9

where **α, β** and **γ** are constants of a particular substance.

The heat capacity (Cp values) and enthalpy are critical for calculating the adiabatic temperature (Varma *et al*., 2016). The C*p*, indicates the amount of heat needed to raise the temperature of a given quantity of a substance by 1 ºC which is described by the coefficients $\alpha\alpha$, $\beta\beta$, and $\gamma\gamma$. (Siddique *et al.,* 2022). Understanding how a material will behave thermally during synthesis is essential. The enthalpy, on the other hand, refers to the total heat content of the system and is crucial for determining the heat exchange during the reaction (Siddique *et al.,* 2022). This heat exchange is directly linked to the energy required for the reaction to proceed and the stability of the powders formed. Accurately calculating these values ensures effective control and optimization of the SCS process (Rosa *et al.,* 2013).

Table 3.4: Enthalpy and heat capacity data for the calculation of the adiabatic temperature of VO_x/MgO synthesized by the SCS method (Sherikar and Umarji, 2011)

Compound	ΔHf **(25 ℃) (kJ mol⁻¹)**	Cp **(J mol⁻¹K⁻¹)**
NH_4VO_3	-1551.8	-
$MgNO_3.6H_2O$	-1322.5	-
$C_2H_5NO_2$	-528.5	-
$N_2H_4.H_2O$	50.63	-
$CO(NH_2)_2$	-333.2	-
MgO	-601.6	26.88
V_2O_5	-1551.8	33.4
H_2O	-241.8	30
CO_2	-393.5	43
N_2	0	27
O_2	0	25

3.2 Catalyst characterization

3.2.1 Inductively coupled plasma optical emission spectroscopy (ICP-OES)

Quantitative elemental analyses were performed using an ICP-OES (700 Series Agilent). Sample preparation involved the digestion of 15 mg of a powdered catalyst in 10 mL of sulphuric acid. The acid-digested samples were transferred to a 100 mL volumetric flask and diluted to the mark with double distilled water. Instrument calibration was performed using separate standards of Mg and V (ultraspec 1000 ppm standard in 0.5M H_2SO_4) and 1000 ppm in HNO_3 (Merck).

3.2.2 X-ray diffraction and Rietveld refinement (XRD)

XRD analysis was conducted using a Bruker D8 Advance X-ray diffractometer equipped with a Co-Kα X-ray source (λ = 1.78897 Å). For phase identification, Bruker DIFFRACEVA Version 2 software was used, while average crystallite sizes and relative phase abundances were obtained from Rietveld refinements using Bruker AXS Topas Version 4.1

3.2.3 Temperature programmed reduction (TPR)

For the TPR experiments, approximately 50 mg of the powdered samples were loaded into a quartz U-shaped reactor tube sandwiched between two layers of quartz wool. Sample preparation involved heating the catalyst to 400 °C under a flow of argon, followed by gradual cooling to 80 °C. For TPR analysis, the sample was gradually heated to 950 °C at a rate of 10 °C min^{-1} under a steady flow of 5% H_2 in Ar. The reduced sample was cooled under a flow of argon to 80 °C.

3.2.4 Temperature programmed desorption-CO_2-(TPD)

For CO_2-TPD, 30 mg of powdered sample was pre-treated at 350 °C under a flow of He for 1 hour. The samples were then allowed to cool down to 80 °C. Thereafter, a mixture of 5% CO_2 in He was passed over the samples at a flow rate of 30 mL min^{-1} for 1 hour. The excess CO_2 was removed by purging with He for 30 minutes. The temperature was then gradually raised to 950 °C by ramping at 10 °C min^{-1} under a flow of helium and desorption data were recorded.

3.2.5 Scanning electron microscopy (SEM)

SEM, in combination with energy-dispersive X-ray spectroscopy (EDS), was used to determine the elemental composition of the material. Images were obtained using a LEO1450 scanning electron microscope. Prior to imaging, the samples were coated with gold using a Polaron SC sputter coater.

3.2.6 Transmission electron microscopy (TEM)

TEM was performed using a double-aberration corrected JEOL ARM200F instrument operated at 200 kV. The microscope was equipped with a large angle Oxford Xmax 100 EDS detector and a Gatan Quantum 965 ERS electron energy loss (EELS) spectrometer with dual EELS capability. Imaging and diffraction of the samples were performed in TEM mode, while imaging and elemental analysis were

performed in scanning mode (STEM) using a subangstrom-sized probe with a probe current between 68 pA and 281 pA. EELS was performed using spectra of either 1024 or 2048 channels, with energy dispersions of 0.5 eV and 1 eV per channel, respectively. Similarly, the EDS spectra were collected using 2048 channels within a 2kV energy range. The dwell time for each acquisition mode was chosen to optimize the intensity of the signal acquired while minimizing the potential impact of the electron beam irradiation on the sample.

3.2.7 Brunauer-Emmett-Teller (BET) analysis

For BET analysis, approximately 200 mg of the sample was used to determine the pore volume, surface area and absorption desorption using a micrometrics Tristar II surface area and porosity analyser.

3.2.8 Catalytic testing

Testing of the catalysts was conducted on a continuous flow, fixed-bed reactor operating in vertical flow mode. The outer diameter of the reactor tube was 12.5 mm, and the tube was composed of grade 316 stainless steel, from Swagelok. The tube was then cut to 340 mm in length. The catalyst bed contained 1 mL of catalyst, which equates to approximately 0.45 g of the solid catalyst with pellet sizes in the range of 300–600 μm. These pellets were diluted with 1 mL of 40-grit carborundum. A 40-grit carborundum was used to fill all voids in the reactor tube. Feed composed of 5 vol% and 12 vol% *n*-octane in air and N_2 was used for the testing at a fixed flow rate. A gas hourly space velocity (GHSV) of 8000 h^{-1} was obtained by adjusting the catalyst volume. A C:O ratio of 8:2 was used, which corresponds to a ratio of one molecule of *n*-octane, (8 mol of C) to one O_2 molecule (2 mol of O). Mass flow controllers from Bronkhorst HIGH-TECH were used to feed the air and the diluent (N_2) into the system. The feed was introduced using a Series II HPLC pump and the mass flow rate of the feed was measured continuously using an analytical balance. A Ritter type wet gas flow meter was used to measure the total flow rates of the gaseous products. The feed was maintained in the gaseous phase by heating the reactor lines after the point of introduction at 200 °C. Catalyst testing was conducted over several days, ensuring that the results were obtained under steady-state conditions in the temperature range of 400 to 500 ºC. Several data points were obtained at each temperature with a carbon balance ranging from 98-101%. A gas-tight syringe for GC analyses was used to draw gas samples through a septum fitted into a glass bomb placed on the gas vent. A cylindrical stainless-steel catch pot set at 3 ºC was used to collect all the liquid products. A Perkin Elmer Clarus 400 GC fitted with a 30 m 530 μm Supelco Carboxen 1006 PLOT column and a thermal conductivity detector (TCD) were used to quantify carbon oxides (CO and CO_2). Liquid products were quantified using a Shimadzu GC-2021, (Kyoto, Japan), fitted with a flame ionization detector and a 50 m 200 μm PONA capillary column.

CHAPTER 4: RESULTS AND DISCUSSION

4.1 Surface and elemental properties

The SCS method is particularly effective in producing well-dispersed VO_x catalysts, which are essential for producing a number of active sites that are critical in catalytic ODH reactions (Varma *et al*., 2016). The choice of mixed fuel, which consists of a 50/50 ratio of glycine, urea and hydrazine hydrate, is imperative for tuning the catalyst's surface characteristics. The fuel mixture influences the combustion temperature and heat release during synthesis, thereby controlling the surface area, porosity, and particle size of the catalyst (Varma *et al*., 2016). A higher surface area increases the number of active sites, enhancing the catalytic activity, while the enhanced porosity impacts the diffusion of reactants and products, affecting the catalyst's efficiency and selectivity (Awan *et al.,* 2019). The ICP results suggest that the measured vanadium composition correlates with the 15 wt. % V_2O_5 loading that was targeted. The BET results are also presented in Table 4.1, together with the parameters of the synthesized catalysts derived from those results. There were slight variations in surface area, pore volume and pore size with each catalyst, with the GLY/HH catalyst having a higher surface area than the other catalysts, consistent with the results obtained by Daems *et al.* (2014).

Figure 4.1 illustrates the correlation between the crystallite size and surface area for these catalysts. The GLY/HH catalyst exhibited the highest surface area of 37.7 m^2/g and the lowest crystallite size of 3.3 nm for the magnesium orthovanadate phase, as shown in Tables 4.1 and 4.2. The crystallite size increases with decreasing available external surface area per unit (Takagi *et al.,* 2021). A high surface area exposes more active sites to the reactants, facilitating more efficient catalytic reactions (Zhu *et al.,* 2017). In contrast, a low surface area results in fewer active sites being available for catalytic reactions and can result in lower catalytic activity. Therefore, controlling the crystallite size is essential for maximizing the material surface area and catalytic efficiency.

Table 4.1**:** Nitrogen physisorption results and elemental composition obtained from BET and ICP-OES

Sample	**Vanadium loadings (Wt. %)**	**Surface area (m^2/g)**	**Pore volume (cm^3/g)**	**Pore size (nm)**
GLY/UR-MgO	-	5.3	0.001	45
UR/HH-MgO	-	18.0	0.002	53
GLY/HH-MgO	-	15.5	0.005	45
GLY/UR -VO_x/MgO	14.6	23.4	0.012	153
UR/HH -VO_x/MgO	14.0	31.2	0.021	165
GLY/HH -VO_x/MgO	14.9	37.7	0.030	163

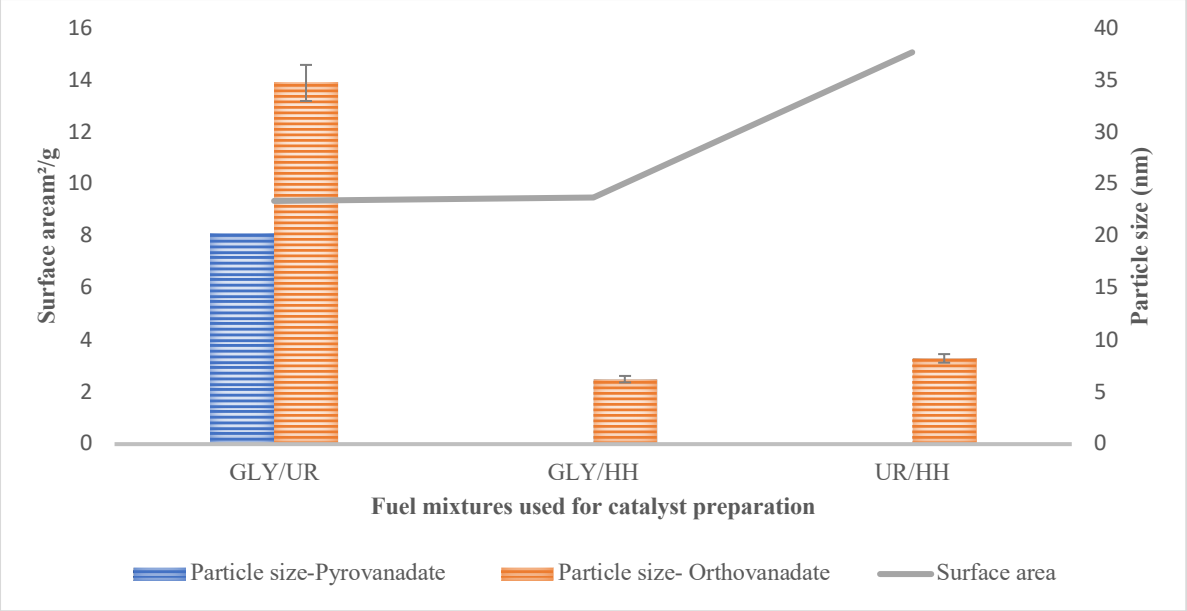

Figure 4.1**:** Correlation between crystallite size and surface area for the mixed fuel VO_x/MgO: GLY/UR, GLY/HH and UR/HH

Figure 4.2 presents the low-temperature nitrogen adsorption-desorption isotherms for the VO_x/MgO catalysts synthesized using mixed fuels. The VO_x/MgO catalysts prepared from the three fuel mixtures UR/HH, GLY/HH and GLY/UR have H4 hysteresis loops (Nayak and Nayak, 2016). The steep increase in the relative pressure region of 0.9-1.0 indicates a closed loop, which is observed when the pore size distribution of the absorbent material has a high affinity for the surface of the material (Serafin *et al.,* 2021). The amount of nitrogen physisorbed is relatively equal for all three supported catalysts; hence, the shapes of the isotherms for all catalysts prepared by SCS are the same. The observed hysteresis loops in the nitrogen adsorption-desorption isotherms for the GLY/UR, GLY/HH, and UR/HH catalysts suggest that adsorption predominantly occurs in large macropores or void spaces within the catalyst structure. These macropores facilitate rapid release of the adsorbed gas, indicating a specific porosity characteristic that can influence the catalytic behaviour and efficiency of these materials (Serafin *et al.,* 2021).

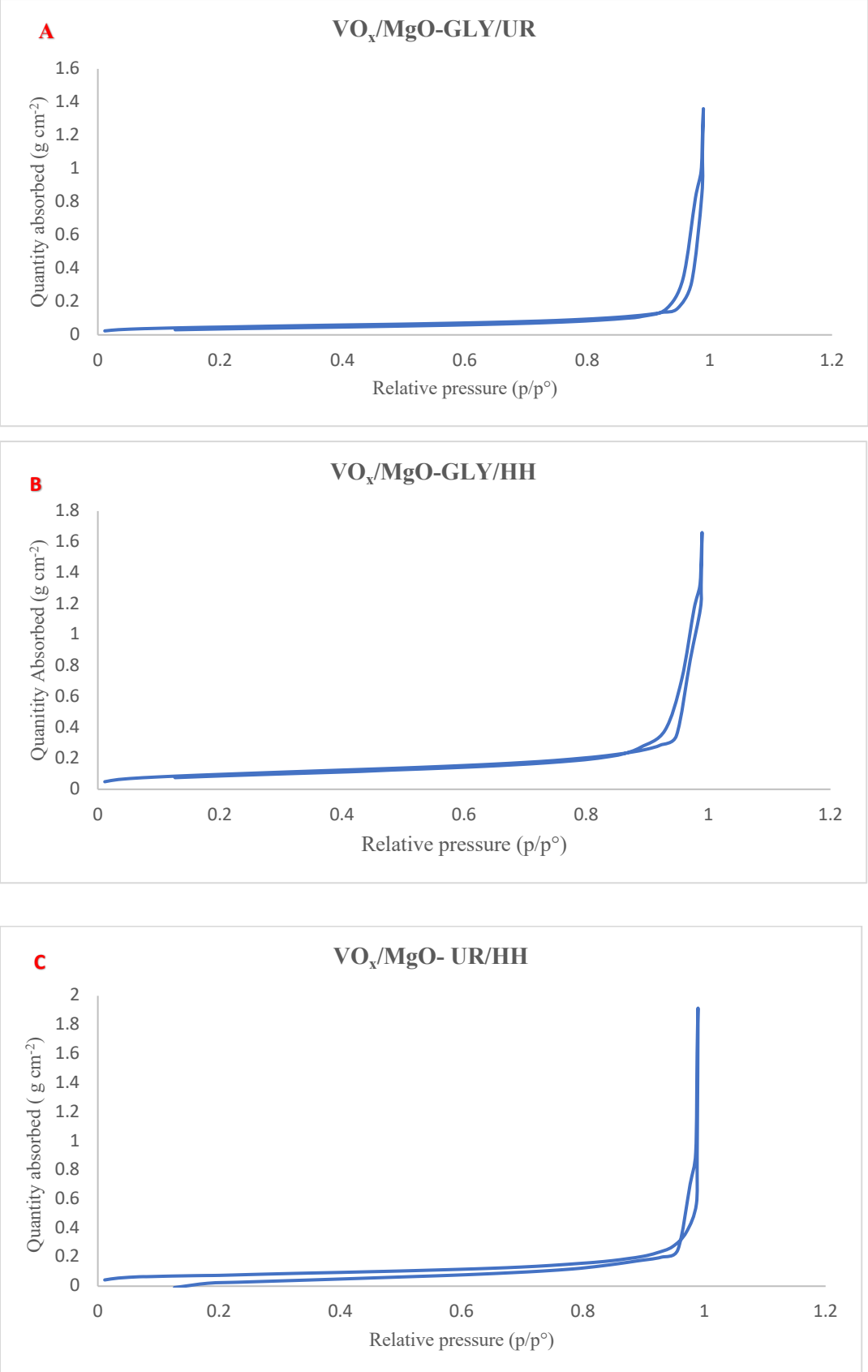

Figure 4.2**:** Low-temperature nitrogen adsorption-desorption isotherms for mixed fuel VO_x/MgO catalysts *(A)* GLY/UR, *(B)* GLY/HH and *(C)* UR/HH

4.1.1 XRD and Rietveld refinement

The XRD pattern of the GLY/UR catalyst is presented in Figure 4.3. The GLY/UR catalyst has three phases: periclase, magnesium orthovanadate and magnesium pyrovanadate. The diffractogram shows 2 theta values of 50° and 72°, which are consistent with the periclase phase. The smaller peaks prior to the periclase phase are attributed to the $Mg_3(VO_4)_2$ and $Mg_2V_2O_7$ at 2 theta values of 20° and 40°, respectively. The formation of three phases in the VO_x/MgO catalyst synthesized using fuel mixtures of GLY/UR can be attributed to two factors: the combustion reaction between these fuels and the oxidizer, leading to the formation of a high-temperature flame. A higher combustion temperature and a lower quenching rate can favour the formation of more intermediate precursors and provide more time for the crystallization process. This can result in multiple crystalline phases, as observed for the VO_x/MgO catalyst synthesized from the GLY/UR mixture (Manukyan *et al.,* 2013).

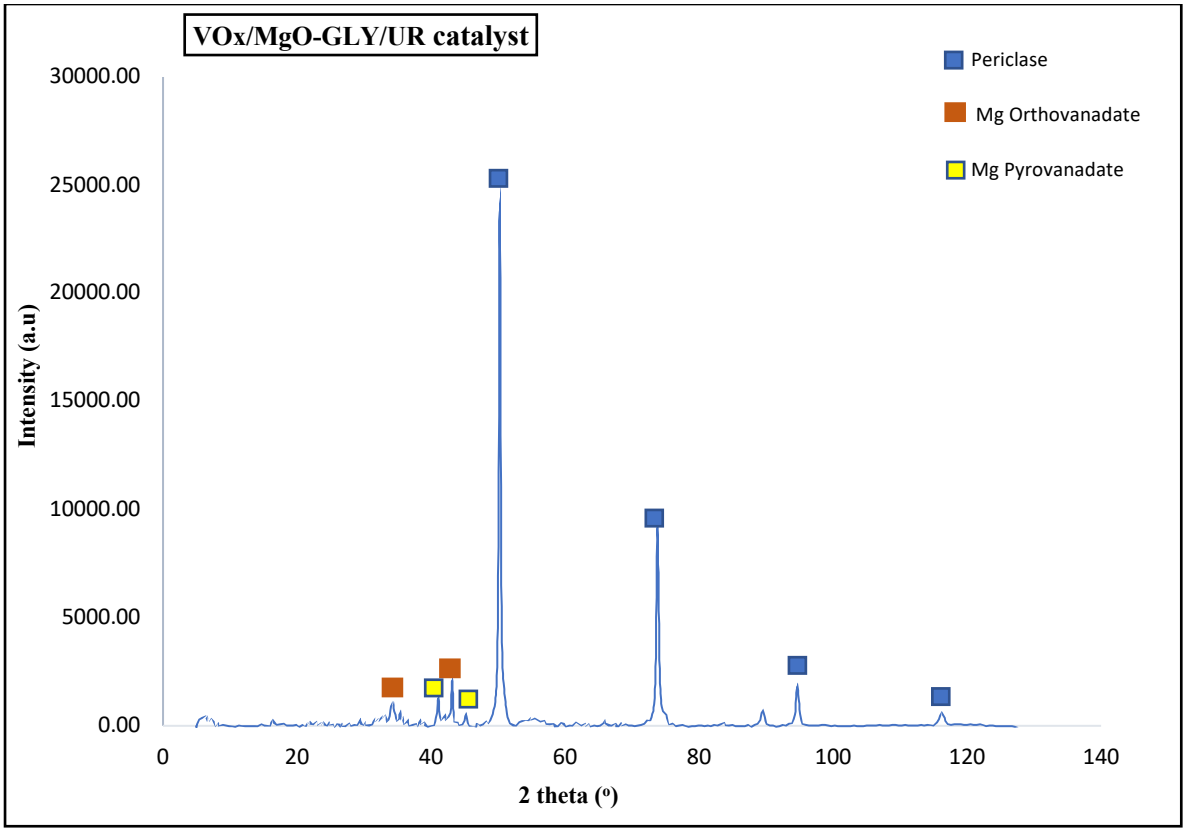

Figure 4.3**:** X-ray diffractogram for the VOx/MgO catalyst prepared by GLY/UR fuel mix

Figure 4.4 shows the XRD pattern of the GLY/HH catalyst. This catalyst exhibited two phases, the MgO and the $Mg_3(VO_4)_2$. The 2 theta values observed at 50° and 72° are attributed to the periclase phase. The smaller peaks before the periclase phase at 2 theta values of 20° and 40° are attributed to the $Mg_3(VO_4)_2$ phase. As a fuel, glycine can act as a chelating agent and form complex precursors with metal cations such as Mg^{2+} and V^{5+} during the initial gel formation stage (Ghosh *et al.,* 2010). During combustion,

these precursors can decompose to form intermediate vanadium oxide species such as vanadium oxide hydrates, which can then react with MgO to form the $Mg_3(VO_4)_2$ phase. The formation of only two crystalline phases in the VO_x/MgO catalyst during the SCS process is attributed to the mixing of glycine and hydrazine hydrate fuels, which affects the overall combustion temperature during synthesis (Sherikar and Umarji, 2013).

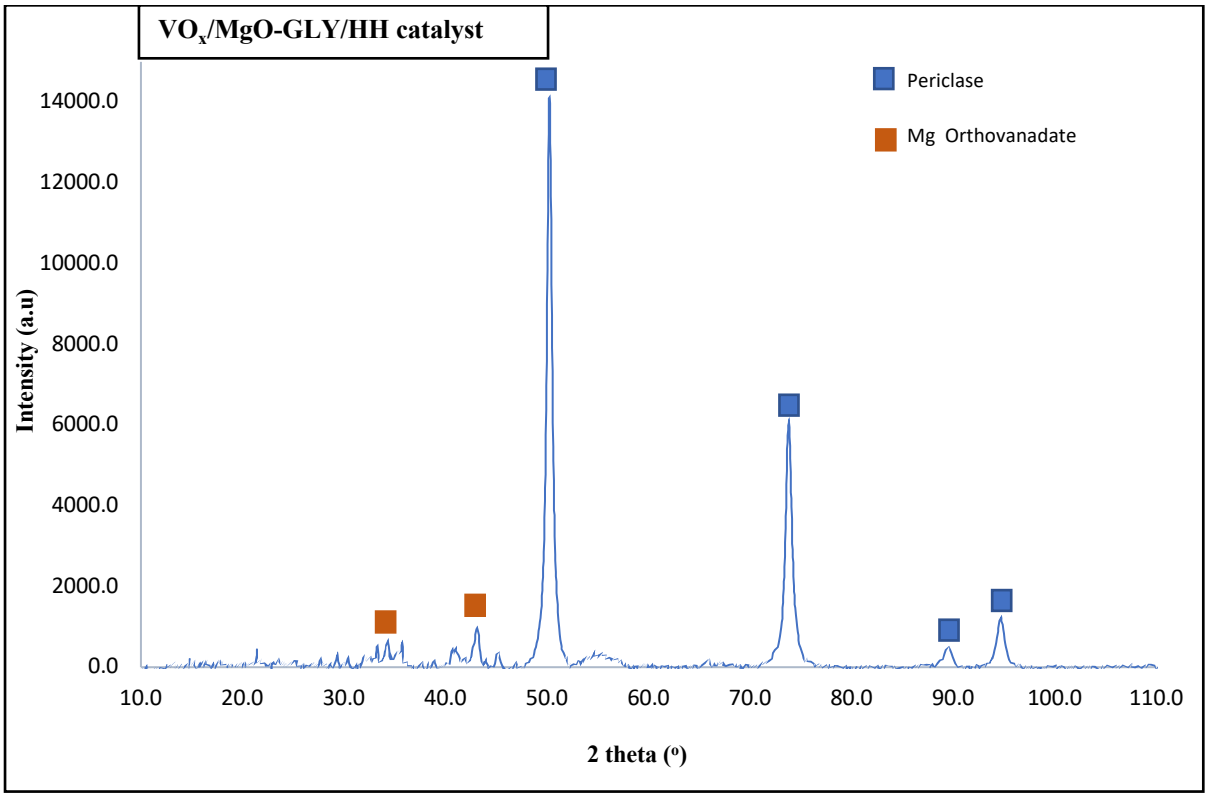

Figure 4.4**:** X-ray diffractogram for the VO_x/MgO catalyst prepared by GLY/HH fuel mix

Figure 4.5 shows the XRD pattern of the UR/HH catalyst. Two distinct phases, MgO and $Mg_3(VO_4)_2$ were observed. The two reflections at 2 theta values of 50° and 72° are associated with MgO periclase. The smaller peaks prior to the MgO phase are attributed to the $Mg_3 (VO_4)_2$ at 20° and 40°, which are similar to those of the other catalysts except for GLY/UR.

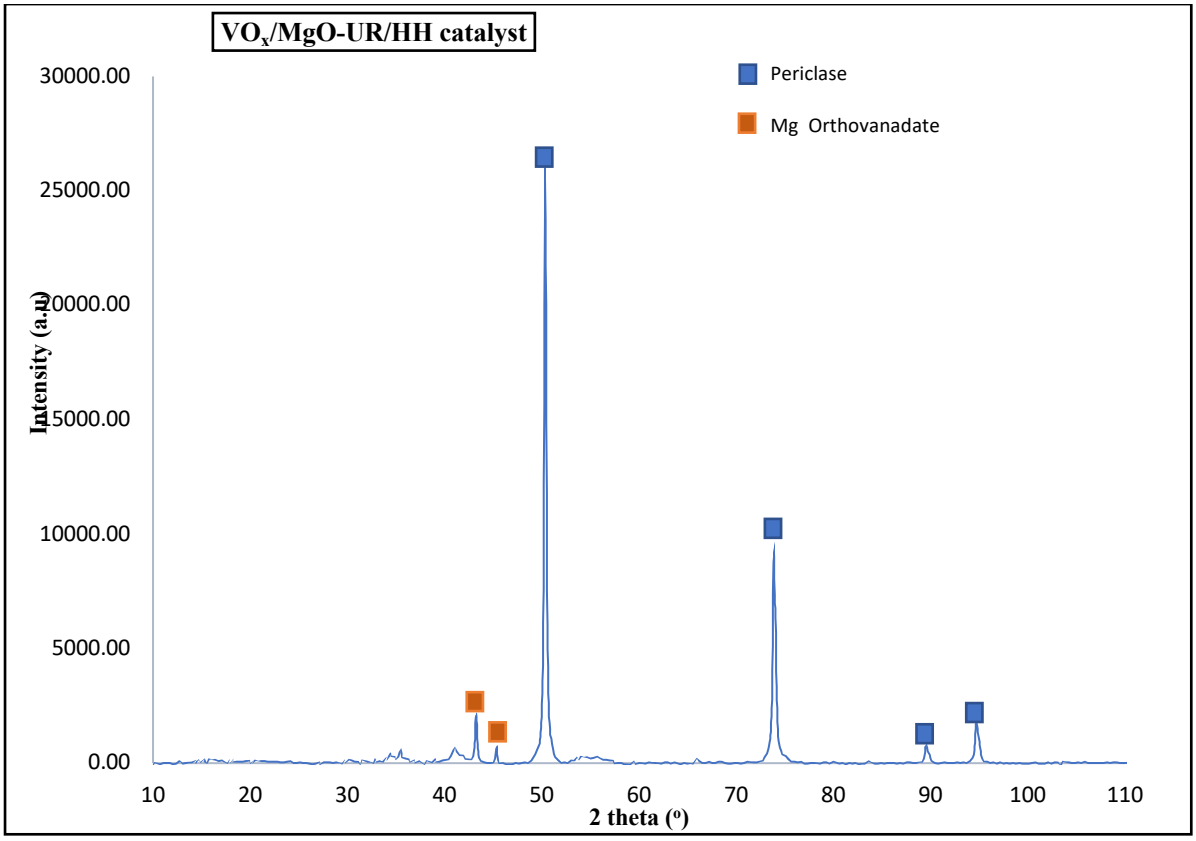

Figure 4.5: X-ray diffractogram for the VO_x/MgO catalyst prepared by UR/HH fuel mix

Table 4.2 shows the Rietveld refinement results for the unsupported and supported catalysts. The GLY/HH catalyst displayed the smallest crystallite size, followed by the GLYUR catalyst. Glycine fuel was used for the preparation of both catalysts. These results are consistent with data obtained by Ntola *et al.*, 2022, where catalysts synthesized using glycine fuel displayed the smallest crystallite size. The relative phase abundance of $Mg_3(VO_4)_2$ was observed for all the supported VO_x/MgO catalysts prepared with the three fuel mixtures in the following order: 24.1 > 17 > 15.6 nm for the UR/HH, GLY/HH and GLY/UR catalysts respectively. The formation of the magnesium pyrovanadate phase is consistent with findings from Ntola *et al.,* 2022, where catalysts prepared using the glycine fuel showed the presence of this phase (Ntola *et al.,* 2022). Tenorite and silicon were found in trace concentrations (up to 1%).

Table 4.2: XRD and Rietveld refinement

Sample	Catalyst phases	Relative phase Abundance (mass %)[a]	Phase	The crystallite size. (nm)[b*]
GLY/UR-MgO	MgO	99	Periclase	51
UR/HH-MgO	MgO	99	Periclase	81
GLY/HH-MgO	MgO	99	Periclase	30
GLY/UR-VO_x/MgO	MgO	78	Periclase	31
	$Mg_3(VO_4)_2$	15	Orthovanadate	14
	$Mg_2V_2O_7$	5	Pyrovanadate	8.3
UR/HH-VO_x/MgO	MgO	75	Periclase	44
	$Mg_3(VO_4)_2$	24	Orthovanadate	2.5
GLY/HH-VO_x/MgO	MgO	82	Periclase	14
	$Mg_3(VO_4)_2$	17	Orthovanadate	3.3

[a] Error less than 1%, [b*] volume weighted averaged crystallite size (Lvol-IB) - Rietveld

4.1.2 Transmission electron microscopy

TEM provides detailed insights into the catalyst's nanostructure, allowing for the determination of crystallite size, shape, and dispersion. This information is crucial for understanding catalytic performance. SEM complements TEM by providing a macroscopic view of the catalyst's surface and its distribution on the support. These techniques enable researchers to assess the quality of catalyst particles, investigate catalyst-support interactions, and optimize the synthesis process for VO_x/MgO catalysts, ultimately leading to improved catalytic efficiency and stability in various applications.

4.1.2.1 EDS

Figure 4.6 *(A), (B)* and *(C)* shows the EDS spectra of the VOx/MgO catalysts. The spectra confirm the weight loadings as determined by ICP. The measured loadings are in close agreement with the targeted amount of 15 wt. % V_2O_5.

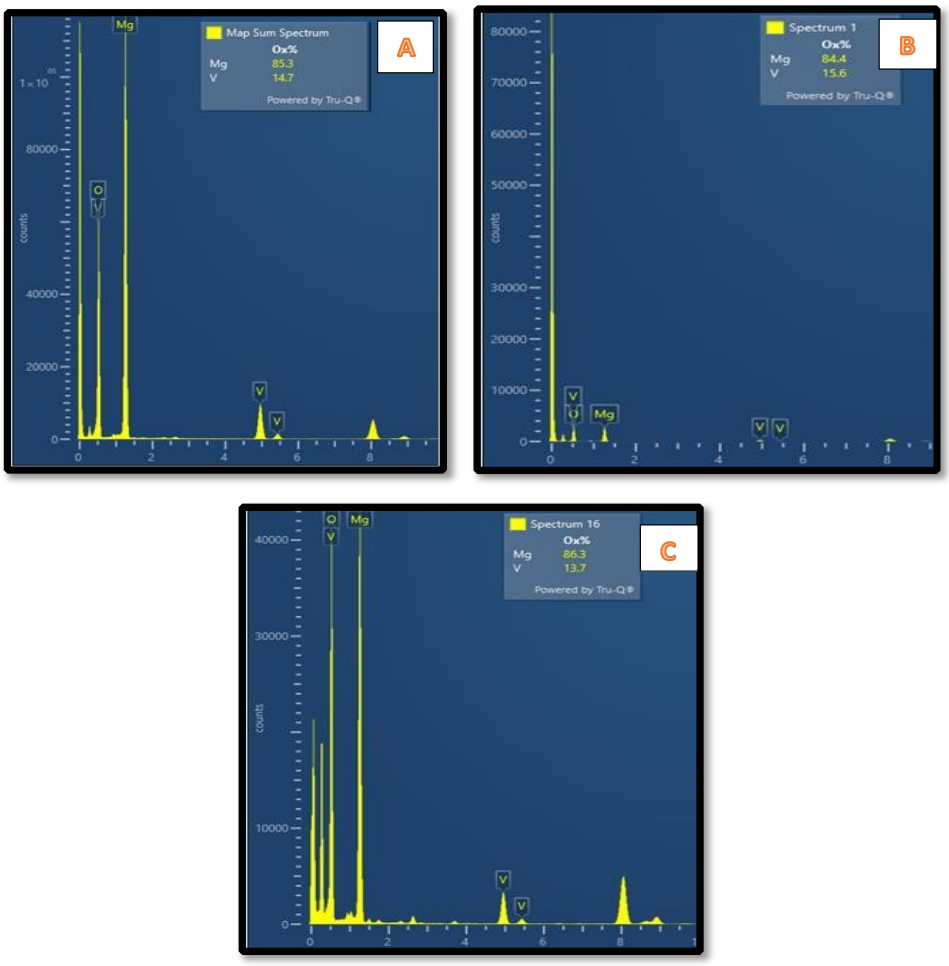

Figure 4.6*(A)* EDS spectrum of the catalyst GLY/UR *(B)* EDS spectrum of sample GLY/HH *(C)* EDS spectrum of catalyst UR/HH.

4.1.2.2 TEM

Figure 4.7 *(A)* shows a Bright-field TEM image of the GLY/UR catalyst. The catalyst shows particles with a round morphology, along with clusters of smaller and larger nanoparticles. The larger particles are attributed to MgO which was evident in the XRD data. The presence of small and large crystalline domains within the particles suggests the occurrence of multiple crystal growth stages or sintering during the combustion process (Sánchez-Jiménez *et al*., 2021). The smaller nanoparticles could most likely be attributed to the $Mg_3(VO_4)_2$ and $Mg_2V_2O_7$ phases. According to the XRD Rietveld refinement results, crystallite sizes of 13.9 and 8.1 nm were obtained for these phases.

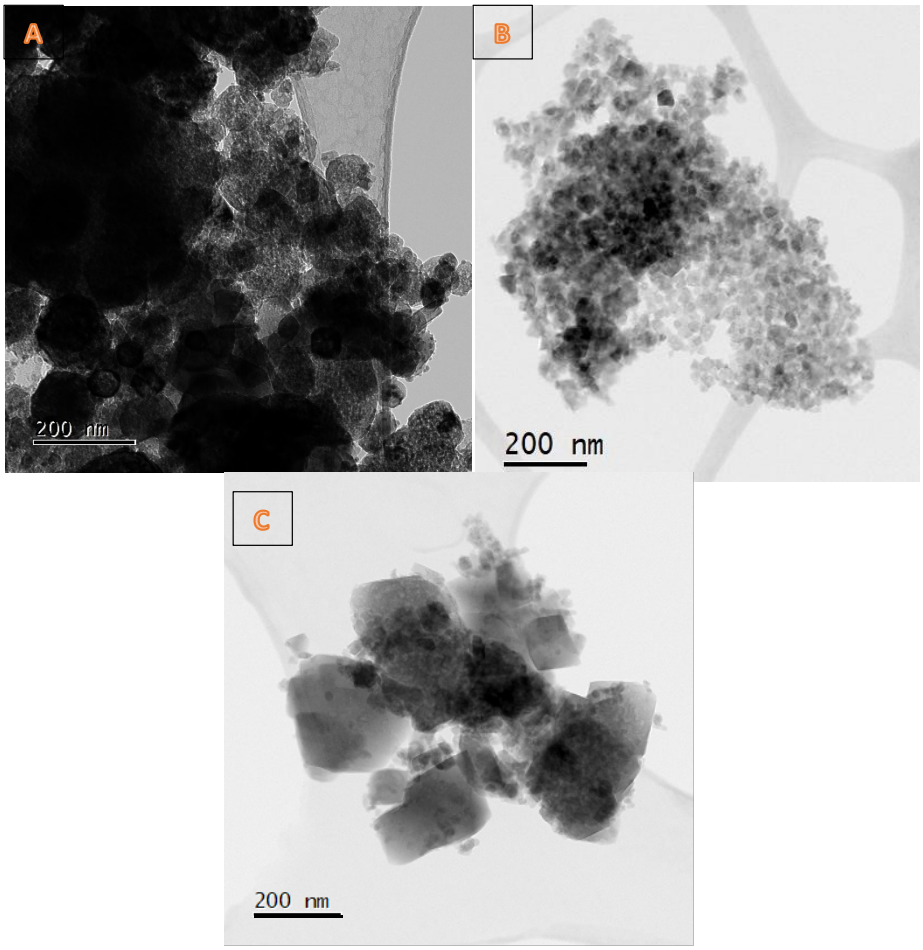

Figure 4.7 *(A)* Bright-field TEM image of catalyst GLY/UR. *(B)* Bright-field TEM image of sample GLY/HH. *(C)* Bright-field TEM image of sample UR/HH

Figure 4.7 *(B)* shows a Bright-field TEM image of the GLY/HH catalyst. Particles with a spherical morphology were observed. This sample shows a narrow size distribution as compared to that of the GLY/UR catalyst. The images also display differences between the particles, which may indicate differences in mass density or thicker regions of particles. Structural heterogeneity may also result from differences in crystallinity. According to the XRD data with Rietveld refinement, the periclase sample had the highest crystallite size of 13.8 nm, with an 80.3 % phase composition. The $Mg_3(VO_4)_2$ phase revealed a crystallite size of 3.3 nm, indicating that the combustion temperature was rapid, which did not allow crystal growth greater than 3.3 nm for the $Mg_3(VO_4)_2$.

Figure 4.7 *(C)* is a Bright-field TEM image of the UR/HH catalyst, showing large crystals among irregularly shaped regions. Generally, a slow reaction rate promotes the formation and growth of MgO. However, if the time spent at high temperatures to form magnesium vanadates is limited, there will be no formation of the magnesium vanadates, specifically the $Mg_3(VO_4)_2$ phase. The crystal sizes for MgO are larger for the UR/HH catalyst than for the other two catalysts.

Figure 4.8 *(A)-(C)* displays the SAED-TEM patterns of the GLY/UR, GLY/HH and UR/HH catalysts. For all three catalysts, the diffraction patterns are consistent with those materials that are nanocrystalline in nature.

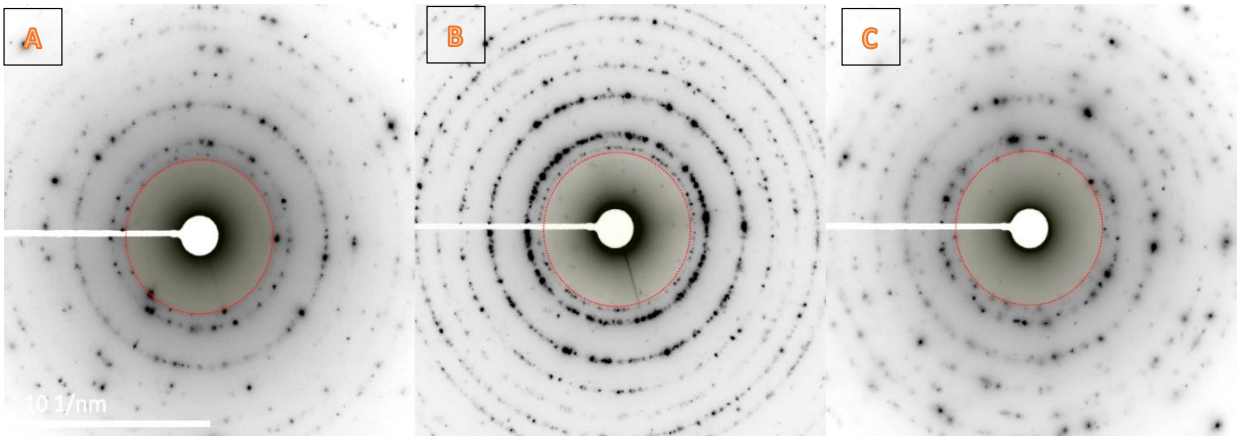

Figure 4.8 *(A)* SAED-TEM pattern of catalyst GLY/UR. *(B)* SAED-TEM pattern of catalyst GLY/HH *(C)* SAED-TEM pattern of catalyst UR/HH

The main reflections observed in Figure 4.8 are those expected to be due to the MgO phase. In the case of the GLY/HH catalyst, the closeness of the spots indicates the presence of smaller crystallites of MgO, which is consistent with the XRD findings and observations from TEM imaging (Ntola *et al*., 2023). The presence of isolated diffraction spots is also observed closer to the centre of the diffraction pattern for the GLY/HH catalyst (annotated yellow shaded area). These spots are consistent with the presence of magnesium vanadate phases, which correlate with the XRD and Rietveld refinement data and are also observed to a lesser extent in the pattern for the GLY/UR catalyst but not in the pattern for the UR/HH catalyst (Ntola *et al*., 2022). This could be due to the comparatively slower burning flame conditions of the UR/HH fuel mix, which would have led to an incomplete crystallization of the magnesium vanadate phase regions, as indicated in Figure 4.9.

Figure 4.9 shows a high-resolution TEM image of a region in which the magnesium vanadate phase is observed, attached to a larger MgO crystal. The right of the image shows a Fast Fourier transform (FFT) obtained from the magnesium vanadate phase region (red square). From the FFT, incomplete crystallization of the phase region may be deduced since no evidence of preferential orientation is observed from the FFT.

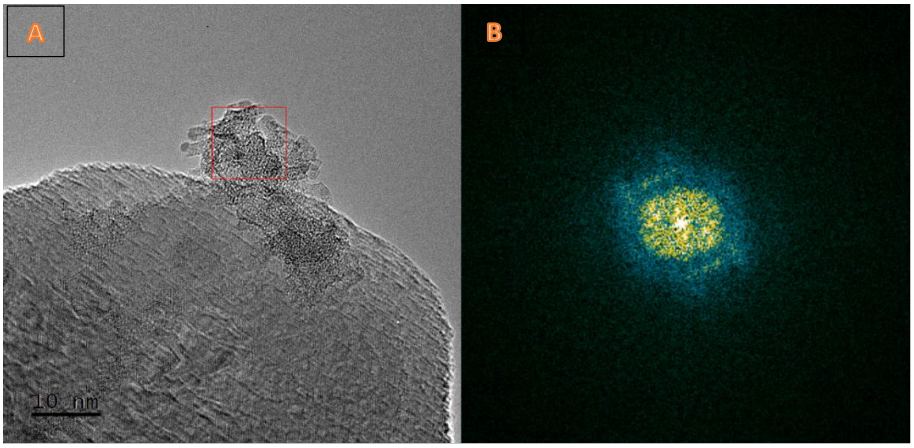

Figure 4.9**:** *(A)* High-resolution TEM image of a region of GLY/HH magnesium vanadate phase, *(B)* FFT indicated by the red square of a region on magnesium the vanadate phase *(A)* of GLY/HH catalyst

4.1.3 Scanning Transmission Electron Microscopy - Electron Energy Loss Spectroscopy

Figure 4.10 shows the STEM-EELS spectrum imaging study of an area in the GLY/UR catalyst. Elemental distribution maps, along with a false colour overlay, are shown. The distribution of V is concentrated in areas previously identified as smaller particle regions, as depicted in the Bright-field image in Figure 4.7.

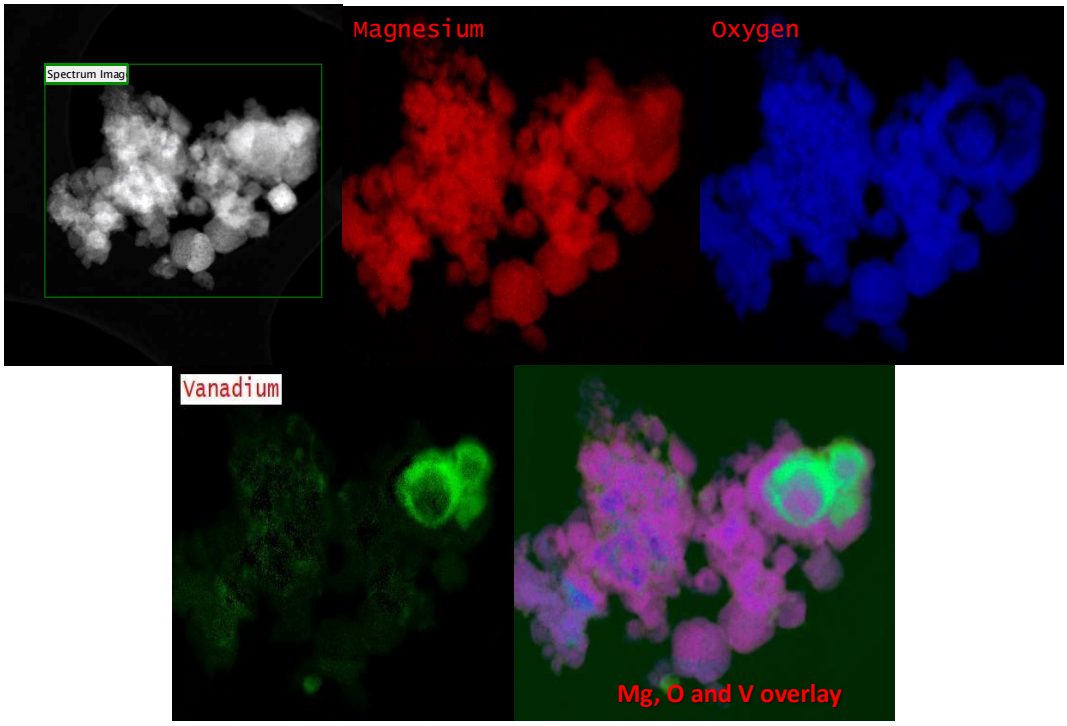

Figure 4.10: Elemental distribution maps of catalyst GLY/UR generated using STEM-EELS

Figure 4.11 shows the elemental mapping for the GLY/HH catalyst. This catalyst shows a rather more uniform distribution of vanadium than the GLY/UR catalyst. Additionally, this catalyst that had displayed the highest surface area of 37.7 m^2/g and could possess non-uniform surface defects (Xie *et al.,*2020). These defects can serve as nucleation sites for the accumulation of vanadium species. Surface defects could be prominent in this specific sample due to it having the lowest concentration of Brønsted acid sites. An increase in the chances of selective adsorption of other species over vanadium can lead to the preferential localization of vanadium in certain areas (Ganjkhanlou *et al.,* 2020). In addition to the high surface area and lowest concentration of acidic sites, the GLY/HH catalyst has the highest adiabatic temperature, with an increased amount of gas expulsion, which is attributed to the localization of specific areas on the MgO support (Pacchioni and Freund. 2013).

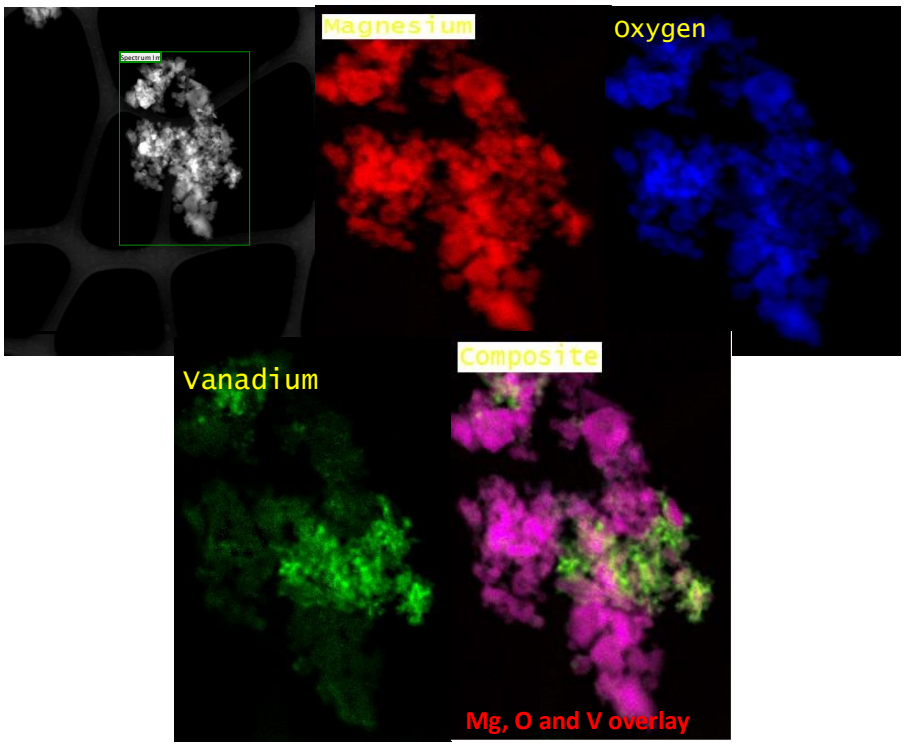

Figure 4.11: Elemental distribution maps of catalyst GLY/HH generated using STEM-EELS

Figure 4.12 shows the STEM-EELS elemental mapping of the UR/HH catalyst. The findings suggest that localized areas of high vanadium density are distributed rather more uniformly than in the other two catalysts, on the surface of the MgO crystals. The UR/HH catalyst contains a relatively high concentration of Brønsted acid sites. This is likely because the vanadium containing phase regions have incomplete crystallization as identified previously, leading to areas that contain a high concentration of Brønsted acid sites. The surface vanadium could be attributed to both crystalline and amorphous

magnesium orthovanadate or magnesium pyrovanadate phases, which is consistent with the XRD and Rietveld refinement results.

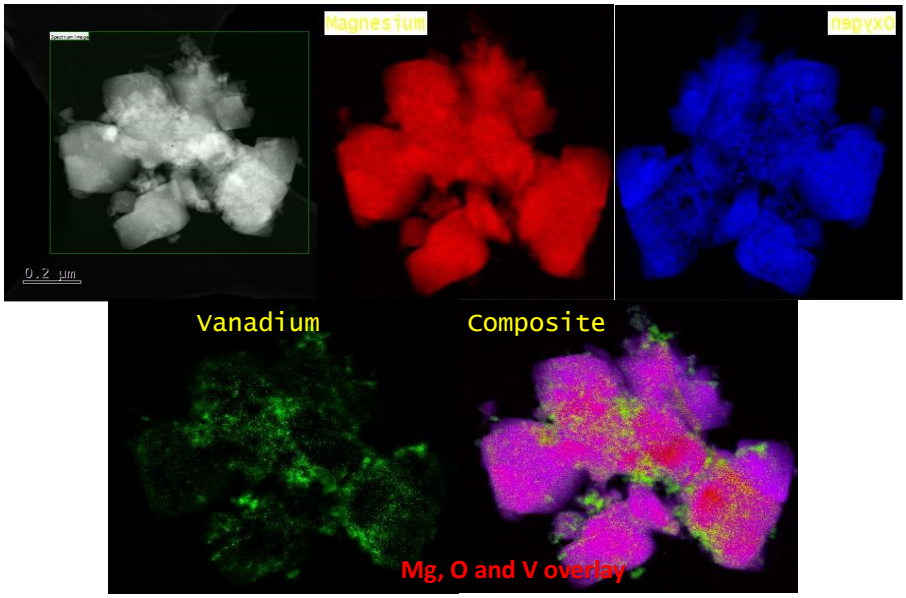

Figure 4.12: Elemental distribution maps of catalyst UR/HH generated using STEM-EELS

Figure 4.13 *(A)* shows the HCD (hollow cone diffraction) images of the GLY/UR, GLY/HH and UR/HH catalysts. HCD was used to indicate the distribution, abundance and positions of crystalline magnesium vanadate phases in the samples. Dark-field diffraction contrast was used since normal bright field diffraction was not suitable for highlighting the positions of these regions. This enables better matching of the crystallite sizes to the Rietveld refinement data. The bright contrast regions in this image show zones where crystalline magnesium vanadate phases have formed. Some diffraction contrast in these images is also visible. GLY/UR was the only catalyst containing the magnesium orthovanadate and magnesium pyrovanadate phases, as determined by XRD and Rietveld refinement. This is consistent with the findings of Ntola *et al.,* where both the magnesium orthovanadate and magnesium pyrovanadate phases were identified when glycine was used as a fuel (Ntola *et al.,* 2023). This is therefore attributed to the properties of the glycine fuel. The crystalline structure of vanadium is confirmed and is observed in the STEM-EELS spectrum. Figure 4.13 *(B)* shows the HCD image of the GLY/HH catalyst. The bright regions indicate the positions of phases indicating magnesium vanadate formation, which is a crystalline magnesium orthovanadate (Ntola *et al*., 2022). These bright regions can indicate areas where the combustion reaction was more vigorous and resulted in the formation of larger and more agglomerated nanoparticles. Nanocrystallinity and an even distribution of vanadium are evident. Figure 4.13 *(C)* is an HCD image of the UR/HH area, with minimal bright regions. However, there are variations in the concentration of the VO_x nanoparticles, however to a lesser extent than in the other two catalysts.

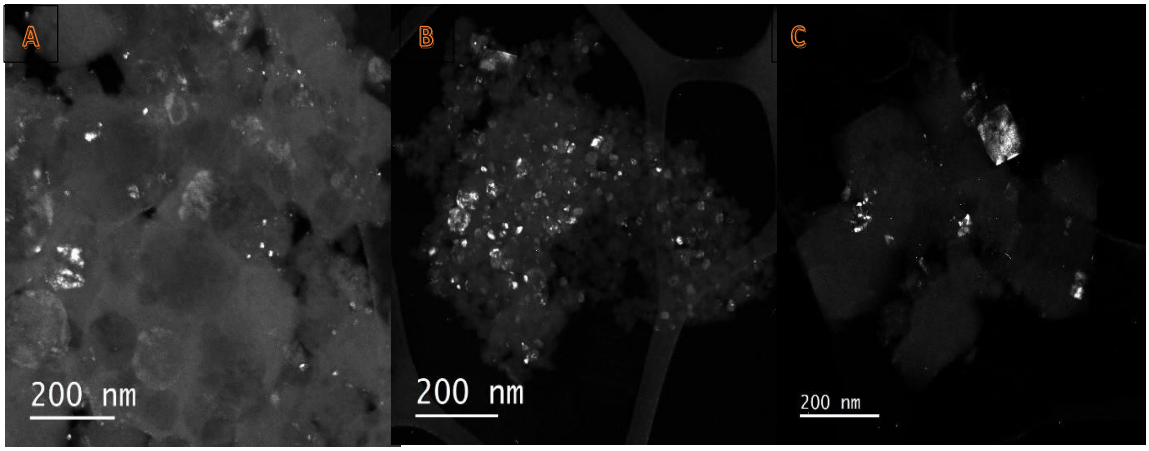

Figure 4.13**:** *(A)* HCD image of catalyst GLY/UR. *(B)* HCD image of catalyst GLY/HH. *(C)* HCD image of sample UR/HH

4.1.4 Temperature programmed reduction (TPR)

The VO_x species on the catalyst surface undergo redox reactions during the ODH process. This involves the transfer of electrons between the VO_x species and the alkane molecule, resulting in the oxidation of the alkane and the reduction of the VO_x (Ntola *et al.,* 2023). The reduced VO_x species can then be re-oxidized by molecular oxygen, regenerating the active catalyst species and releasing water as a by-product (Ntola *et al.,* 2023). The TPR data presented in Table 4.3 are key for understanding the redox properties of mixed fuel VO_x/MgO catalysts and show H_2 consumption for each fuel mixture, with the GLY/UR catalyst showing the highest total H_2 consumption, followed by the GLY/HH catalyst.

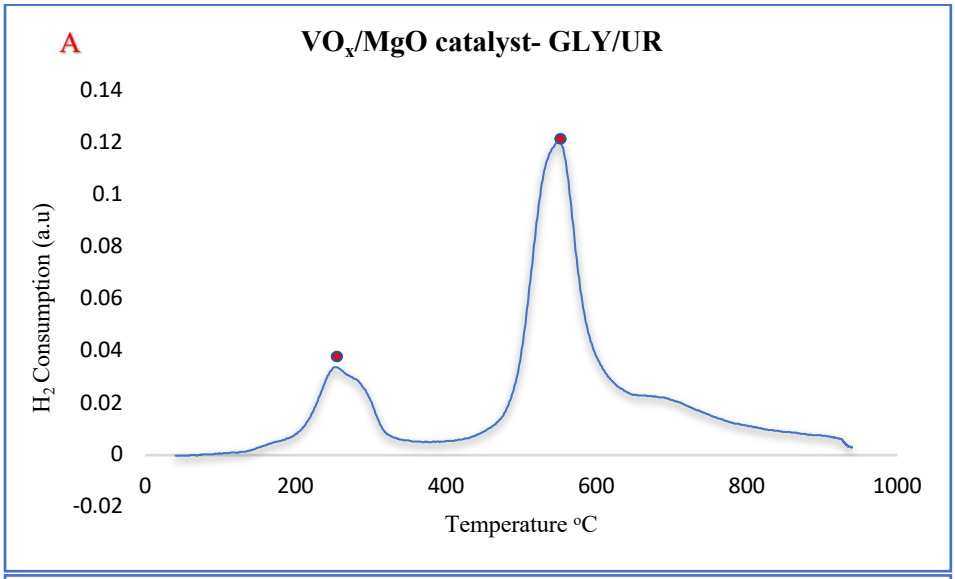

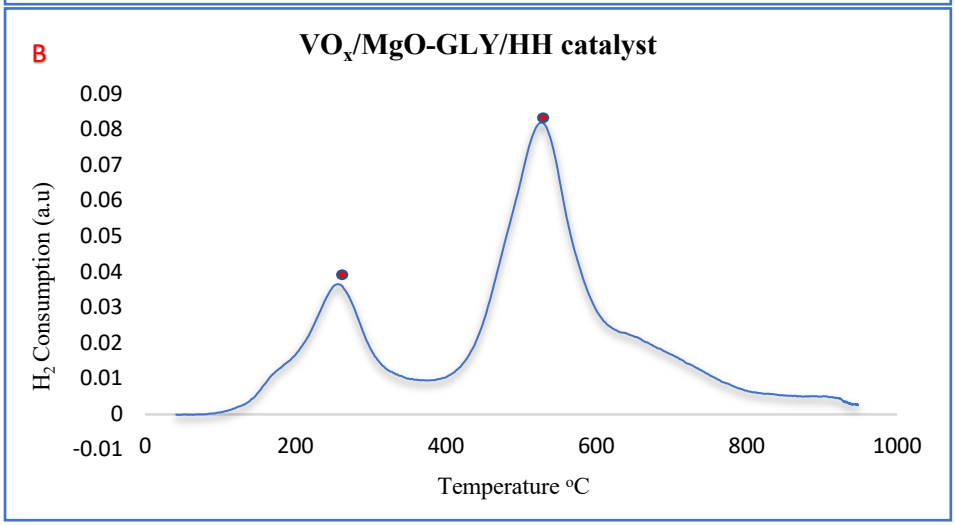

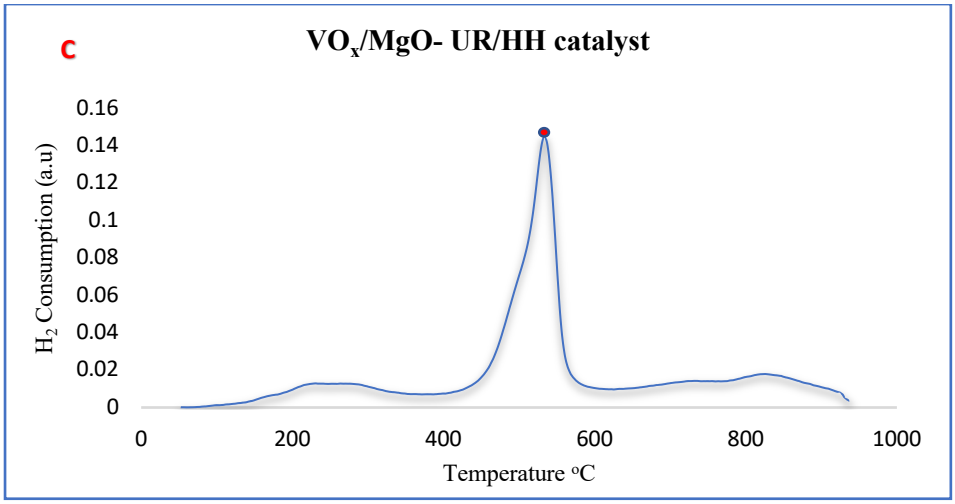

Figure 4.14**:** H_2-TPR profiles of the VO_x/MgO catalysts prepared with (A) GLY/UR, (B) GLY/HH and (C) UR/HH

Table 4.3**:** TPR data for mixed fuel VO_x/MgO catalysts

Catalyst	**T (°C)**	**Total H_2 consumption (cm^3/g/STP)**
GLY/UR-VO_x/MgO	254	0.3
	549	1.5
GLY/HH-VO_x/MgO	229	0.1
	264	0.1
	534	0.9
UR/HH-VO_x/MgO	256	0.4
	528	1.3

According to the above figures, the total H_2 consumption at approximately 250 °C and 500 °C is due to the oxide species on the catalyst surface being in different oxidation states (Zhong *et al.,* 2019). Figure 4.14 shows the H_2-TPR profiles of the GLY/UR, GLY/HH and UR/HH catalysts. The 1st and 2nd reduction peaks observed for the GLY/UR and GLY/HH catalysts are attributed to the monomeric VO_x species. In contrast, the 2nd reduction peak is attributed to the VO_x species present in the magnesium orthovanadate phase. The GLY/HH catalyst showed the highest H_2 consumption compared with the other two catalysts, which indicates a higher reduction potential. The UR/HH catalyst showed the lowest H_2 consumption, according to the XRD data, with the lowest crystallinity for the magnesium orthovanadate phase.

The GLY/HH and GLY/UR catalysts displayed two distinct reduction peaks, suggesting that vanadium is present in two distinct phases. These phases are $Mg_3V_2O_8$ and $Mg_2V_2O_7$, and their presence is consistent with the XRD results obtained using the Rietveld refinement. A temperature of 250 °C marked the beginning of the reduction of VO_x/MgO. According to Blasco *et al.,* the low-temperature

peak can be assigned to the reduction of isolated V^{5+} species in distorted VO_4 tetrahedral environments on the catalyst surface. On the other hand, the high-temperature peak at 500 °C corresponds to the reduction of V^{5+} species belonging to the bulk structure of $Mg_3V_2O_8$ (Laurenti et al., 2017). Both peaks can be related to the reduction of isolated V^{5+} species because the magnesium pyrovanadate phase exists in an amorphous state. The distinct reduction peak in the UR/HH catalyst indicates that the formation of the vanadate phases may have been hampered by the volatile reaction, which sparked sintered particle growth, decreased the surface area by pore clogging, and formed a small crystallite size magnesium orthovanadate phase (Di Salvia *et al.,* 2015).

4.1.5 Temperature-programmed desorption

An active and selective catalyst for ODH should have a suitable combination of acid-base and redox properties. Vanadium catalysts can be both basic and acidic, depending on the conditions under which they are used (Kainthla *et al.,* 2015). The degree of basicity of vanadium catalysts supported on MgO depends on the preparation method and the V/MgO ratio (Elkhalifa *et al*., 2014). In some cases, adding MgO can create Lewis acid-base pairs between vanadium and oxygen atoms in the MgO support, which can enhance the basicity of the catalyst (Elkhalifa *et al*., 2014). However, the basicity of the catalyst can also be influenced by other factors, such as the temperature and pressure of the reaction, the nature of the reactants, and the specific reaction mechanism involved (Kalz *et al*., 2017). In addition to basic sites, acid sites on a catalyst play a crucial role in catalytic activity because they are responsible for facilitating the adsorption of the reactant molecule and promoting its reactivity (Zhang *et al.,* 2020). Acid sites are regions within the catalyst that are characterized by a deficit of electrons, which results in a positive charge. This positive charge attracts polar or charged reactant molecules, allowing them to bind to the acid site and undergo chemical transformation (Kalz *et al*., 2017). Additionally, the type of Brønsted acid site can affect the reaction mechanism and product distribution (Zhang *et al.,* 2020). Therefore, controlling the properties of acid sites on the catalysts is crucial for optimizing catalytic performance (Ntola *et al.,* 2022). To calculate the concentration of Brønsted acid sites and evaluate the effect of these sites on the selectivity of the catalysts in the ODH of *n*-octane, chemisorption of isopropylamines, followed by temperature-programmed desorption (TPD) combined with mass spectrometry (MS) analysis of propylene, was performed. Table 4.4 provides a detailed overview of the TPD-MS results for the GLY/UR, UR/HH and GLY/HH catalysts. The data were obtained using TPD of *n*-propylamine, with a mass spectrometer (MS) providing quantitative analysis.

Table 4.4 shows the desorption temperature, which was used in the calculation of the concentration of Brønsted acid sites. The GLY/UR catalyst has the highest concentration of Brønsted acid sites, while the GLY/HH catalyst has the lowest. According to Ntola *et al*., the sample prepared using glycine

exhibited the highest concentration of Brønsted acid sites, which was ascribed to the co-existence of magnesium vanadate phases with a high VO_x content available for reactions at elevated temperatures (Ntola *et al*., 2023). The presence of VO_x species on the magnesium support modifies the acidity distribution in the catalyst by interacting with the vanadium sites in the bulk of the catalyst (Sánchez-García *et al.,* 2020). The desorption temperatures for all the catalysts are comparable, indicating that there are slight to no differences in the Brønsted acid strengths of the catalysts.

Table 4. 4*:* TPD-MS of the GLY/UR, GLY/HH and UR/HH catalysts

Catalysts	**Desorption temperature (°C) (m/z =41)[a,c]**	**N_{as}[b,d] (µmole/ g)**
GLY/UR-VO_x/MgO	99	264
GLY/HH-VO_x/MgO	100	232
UR/HH -VO_x/MgO	100	119

[a]based on Hofmann Elimination the adsorption of propylamine on the Brønsted acidic sites causes C-N bond cleavage, which results in propylene (m/z =41) and ammonia, which were measured using an MS detector in this experiment and [b] the amount of desorbed propylene from the Brønsted acidic sites quantified using an MS detector. [C]+/- 5 °C, [d]+/- 50 µmol/g

Table 1B under Appendix B depicts the calculated Brønsted acid sites for the above-mentioned catalysts, where N_{as} is the concentration of the Brønsted acid sites. GLY/UR was the only catalyst that had two distinct crystalline phases, the magnesium orthovanadate and magnesium pyrovanadate phases. UR/HH depicted only one crystalline phase, with a relatively high concentration of Brønsted acid sites, which could be attributed to the urea fuel undergoing thermal decomposition and forming amine groups that coordinate with metal ions, leading to a higher concentration of sites. The combination of glycine which is a high combustion fuel and urea which is a low combustion fuel, leads to the formation of a catalyst with the highest N_{as} value, indicating the strongest absorption, followed by the UR/HH and GLY/HH catalysts. The greater the concentration of Brønsted acid sites, the lower the energy required to retain the adsorbate on the catalyst surface. This can lead to enhanced catalytic activity due to its ability to withstand high temperatures (Zhang *et al.,* 2017).

4.1.6 Thermodynamics

There are three main thermodynamic processes during the combustion synthesis, namely heat generation due to the exothermic reaction, gas expulsion, and powder crystallization (Saghir *et al.,* 2021). All three of these processes affect the size of the resultant powders. Thus, the heat of reaction and gas expulsion are competing effects (Amirkhanyan *et al*., 2020). The enthalpy of combustion is the amount of heat generated when one mole of a substance is completely burned in the presence of oxygen at constant pressure (Toniolo *et al*., 2010). The enthalpy of combustion is typically expressed in terms of units of energy per mole, such as joules per mole (J/mol) or kilojoules per mole (kJ/mol)

(Amirkhanyan *et al*., 2020). It can be calculated by subtracting the enthalpy of the reactants from the enthalpy of the products, as shown by Equation 4.1.

$$\Delta H_{comb}^{o} = \Delta H_{f}^{o} \text{ (products)} - \Delta H_{f}^{o} \text{ (reactants)} \qquad \text{Equation 4. 1}$$

The difference in enthalpy of formation among the different fuels is one of the main reasons for the varied performance of these fuels during the combustion process since they produce different amounts of heat during the reaction (Sherikar and Umarji, 2011). For example, glycine and urea have enthalpies of formation of −529 and −332 kJ/mol, respectively, representing the ΔH_f (Saghir *et al.,* 2021). Thus, the enthalpy of combustion, ΔH-combustion, is lower for the glycine fuel, resulting in smaller crystals for the glycine-produced powders, assuming that all other factors can be ignored or minimized. The samples prepared using glycine exhibited smaller crystallite sizes of approximately 10 nm (Ntola *et al*., 2023), while the samples prepared using urea had agglomerates with crystals that had coalesced into each other. Thus, the extra heat from the urea combustion promoted sintering through enhanced diffusion. The hydrazine hydrate with the lowest ΔH_f, followed a combustion process that involved slow burning; this, in turn, formed large amorphous crystals (Varma *et al*., 2016).

Although a high combustion temperature is required for the synthesis of multicomponent compounds, the specific surface areas decrease at high synthesis temperatures due to particle growth and sintering, which was evident in the BET data (Kang *et al*., 2018). Table 4.5 shows the physical characteristics of the VO_x/MgO catalysts. The phase composition and the colour of the powders are mainly determined by the chosen fuel mixture and implicitly by the combustion mode. In the GLY/HH catalyst, the combustion reaction propagated throughout the reaction container, and the powder was voluminous with a uniform light-yellow powder. In the case of the GLY/UR catalyst, the combustion reaction was found to be localized and the powder obtained was less voluminous. The colour of the powder was yellow. The UR/HH catalyst reaction showed a slow combustion rate with minimal evolution of gases. The evolved gases also have a pronounced effect during combustion. These gases break up the agglomerates formed during the reaction, thus reducing the particle size (Lyagaeva *et al*., 2017). Therefore, there is a link between the adiabatic flame temperature and the gases that evolve due to the combustion reaction.

Table 4.5**:** Physical characteristics of the flames and catalysts

Catalysts	Flame characteristic	Colour of the synthesized catalyst
GLY/UR-MgO	No gas evolution	White
GLY/HH-MgO	No gas evolution	White
UR/HH-MgO	No gas evolution	White
GLY/UR -VO_x/MgO	Smouldering	Yellow
GLY/HH -VO_x/MgO	No gas evolution	Yellow
UR/HH -VO_x/MgO	Smouldering	Yellow

To investigate the evolution of the energy and flame temperature that was reached during combustion, the theoretical enthalpies of combustion and the theoretical adiabatic flame temperatures were calculated as a function of the fuel-to-oxidant ratio and are presented in Table 4.6. To calculate the adiabatic flame temperature of the SCS reaction, the change in enthalpy (ΔH) for the reaction is calculated using the balanced chemical equation for the combustion reaction and the enthalpy of formation. For the calculations of the estimation of adiabatic flame temperatures, a procedure and formulae were adopted from the supplementary information of Ntola *et al*., (2022). Products (p), *n,* the amount of each compound, $C_{p,Tad}$ and $C_{p,To}$ the heat capacities of the products at the adiabatic temperature and initial temperature T_o were used (Ntola et al., 2022). Based on the theoretical calculations, the GLY/UR-VO_x/MgO catalyst had the lowest burning flame, while the UR/HH-VO_x/MgO catalyst had the highest burning flame.

Table 4.6: Flame characteristics of the catalysts

Catalysts	Adiabatic flame temperature (K)	No moles formed
GLY/UR-MgO	800	14.0
GLY/HH-MgO	1450	28.3
UR/HH-MgO	1532	28.6
GLY/UR -VO_x/MgO	2021	34.7
GLY/HH -VO_x/MgO	3662	38.0
UR/HH -VO_x/MgO	3780	38.4

In Table 4.6, the adiabatic temperatures for the reactions of the VO_x/MgO and MgO catalysts are compared. The results show how the incorporation of vanadium into MgO affects the adiabatic temperature. The GLY/HH catalyst has the highest adiabatic temperature of 3780 K, which is directly attributed to the large gas evolution during the combustion process. The large gas evolution resulted in an increase in surface area, with the greatest increase linked to the GLY/HH catalyst and better homogeneity of VO_x on the surface of the MgO support (Ntola *et al.,* 2023). The GLY/UR and the UR/HH catalysts exhibited lower adiabatic temperatures, 2021 K and 3663 K respectively, which correlates with the lower surface areas for both.

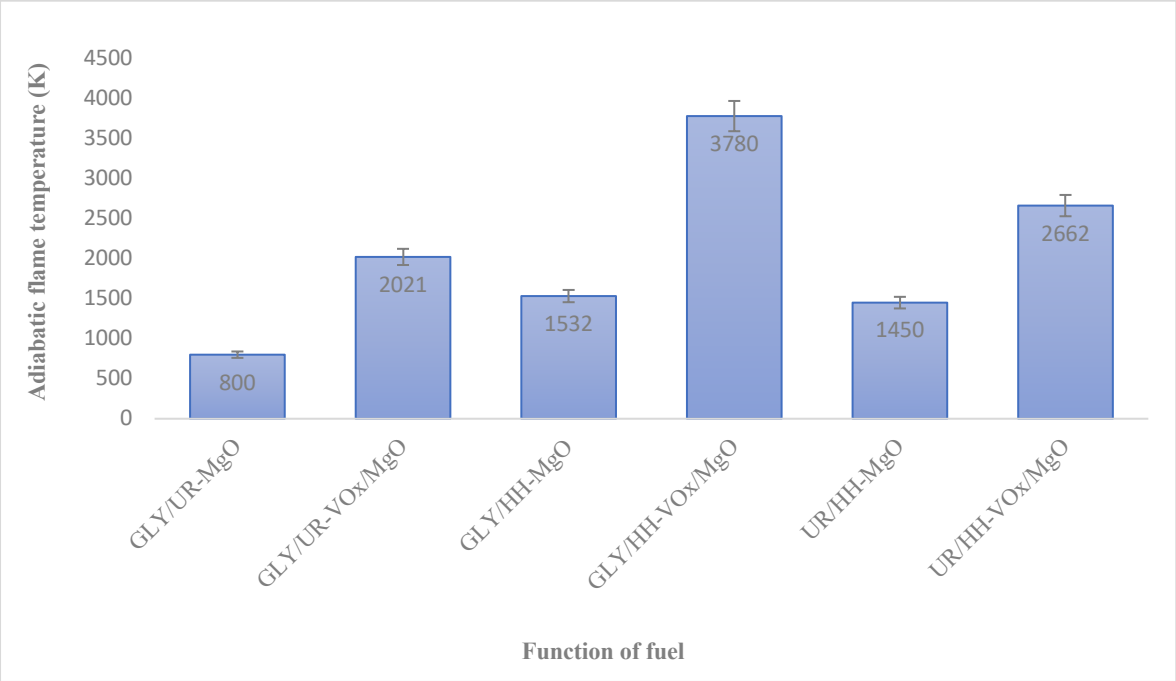

Figure 4.15: Adiabatic temperature as a function of fuel of VO_x/MgO and MgO catalysts

Figure 4.16 shows that fuels with a high carbon content tend to produce more carbon dioxide during combustion. Additionally, fuels with higher densities may release more energy during combustion, which leads to greater gas evolution.

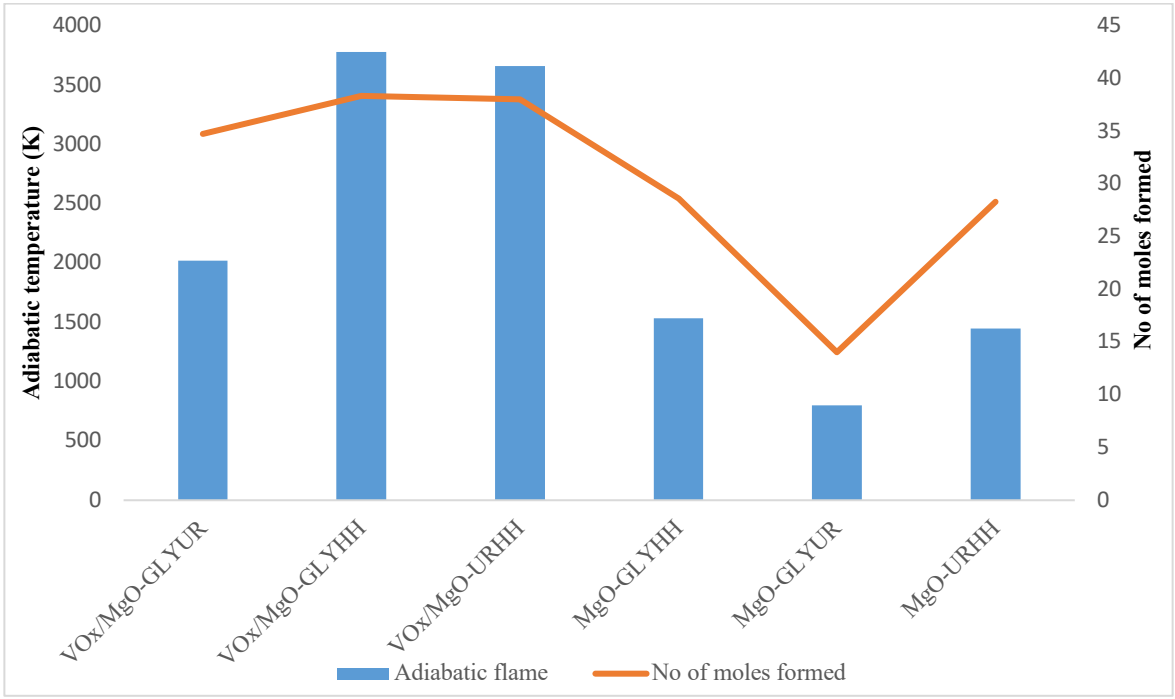

Figure 4.16: Adiabatic temperature as a function of number of moles released

The GLY/HH catalyst showed the highest number of gases released during combustion. Gas evolution creates a convective flow that enhances particle dispersion and prevents particle agglomeration, which is also correlated with the highest adiabatic temperature (Ramirez *et al*., 2019). The number of gas molecules released is controlled by the phase composition and a resulting product is formed with more characteristics of a foam-like structure, consisting of small, spherical, or ellipsoidal particles that are void-filled (Ramirez *et al*., 2019). Gas produced during the SCS process can lead to fragmentation and redistribution of the VO_x species on the surface of the MgO to the bulk of the catalyst, which leads to enhanced catalytic performance. The GLY/UR catalyst showed lower gas evolution than the GLY/HH catalyst. The UR/HH catalyst had the lowest gas evolution. This is attributed to the low reactivity of urea and hydrazine hydrate, which minimize the amount of gas released. These low-temperature conditions promote the formation of faceted structures, enabling the uneven distribution of VO_x species and creating amorphous, large, faceted particles for the UR/HH catalyst (Levchenko *et al.,* 2023).

4.1.7 Phase formation of VO_x/MgO

In the case of magnesium and vanadium oxide phases, the temperature and air-to-fuel ratio can significantly impact the phase, formation, and crystallization. VO_x/MgO catalysts are an important class of materials that have been widely investigated for their use in ODH reactions. One of the key features of these catalysts is the ability to form three different phases, which can influence their catalytic performance (Dasireddy *et al*., 2015). VO_x/MgO catalysts can cycle from the MgO phase to the magnesium pyrovanadate phase through a series of transitions. The initial phase formation of VO_x/MgO catalysts typically involves the synthesis of MgO and VO_x nanoparticles. For example, at temperatures between 600 and 700 °C, the reaction of MgO and VO_x nanoparticles can lead to the formation of $Mg_2V_2O_7$ nanoparticles (Ntola *et al*., 2022). This phase formation occurs via a solid-state reaction pathway, as shown in Equation 4.2 below:

$$4MgO + 2V_2O_5 \rightarrow 2Mg_2V_2O_7 + O_2\,(g) \qquad \text{Equation 4. 2}$$

As the reaction proceeds, the formation of the $Mg_2V_2O_7$ phase is favoured. At higher reaction temperatures above 800 °C, another phase transition can occur, leading to the formation of $Mg_3(VO_4)_2$ nanoparticles. This phase formation can also occur via a solid-state reaction between MgO and V_2O_5 nanoparticles, which can be represented by Equation 4.2.

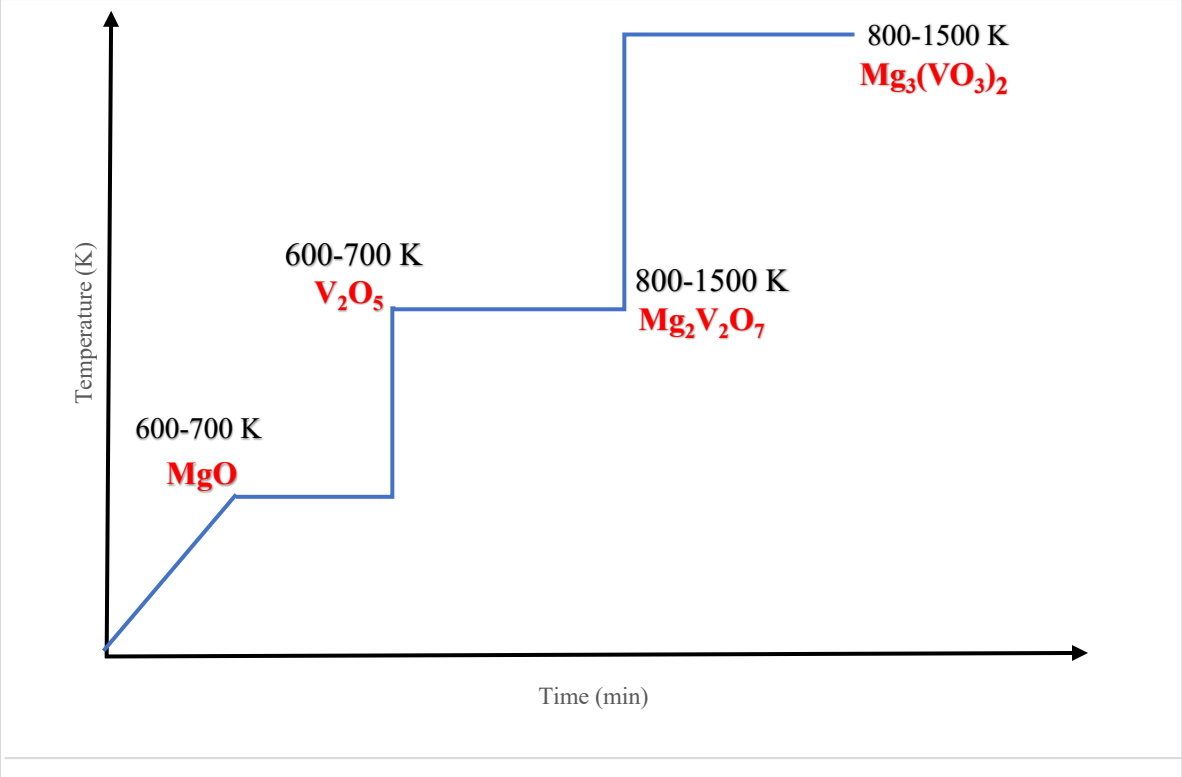

Figure 4.17: Phase change graph showing the formation of the different phases in VO_x/MgO

CHAPTER 5: CATALYTIC TESTING

This chapter focuses on the testing of the catalysts. The results obtained from the characterization are correlated with the catalysts' performance.

5.1 MgO supports

Figure 5.1 shows the *n*-octane conversion over a temperature range of 400-500 ºC. The GLY/HH sample ***(A)*** showed conversions of 2%, 2.4% and 8.1% at 400, 450 and 500 ºC respectively, while the GLY/UR sample (***B)*** showed conversions of 2.4%, 3.4% and 6.9% at 400, 450 and 500 ºC, respectively. The UR/HH sample ***(C)*** displayed lower conversions of 2%, 2.3%, and 6.6% at 400, 450 and 500 ºC, respectively, compared to those of the other MgO supports. The GLY/HH catalyst showed the highest conversion at 500 ºC, followed by the GLY/UR catalysts at ±7.0% conversion. The UR/HH catalyst showed the lowest conversion of 6.4-6.7% at 500 ºC. These conversion values are comparable to the values that were obtained by Elkhalifa and Friedrich, even though the catalysts used were prepared using a different synthesis method (Elkhalifa and Friedrich, 2014).

According to Elkhalifa and Friedrich (2014), the low conversion over MgO is attributed to its low or non-existent redox cycle compared to that of VO_x/MgO. MgO is classified as a basic support and is known to exhibit surface defects such as edges, corners, and kinks and has a degree of hydration and hydroxylation which is also resistant to reduction during TPR experiments (Elkhalifa and Friedrich, 2014). The UR/HH catalyst displayed the largest crystallite size for the periclase phase, which is consistent with the results from Elkhalifa and Friedrich who observed the same phase composition. In addition, Elkhalifa and Friedrich, observed a higher conversion over MgO at 550 ºC, which indicates that the conversion increases with increasing temperature (Elkhalifa and Friedrich, 2014).

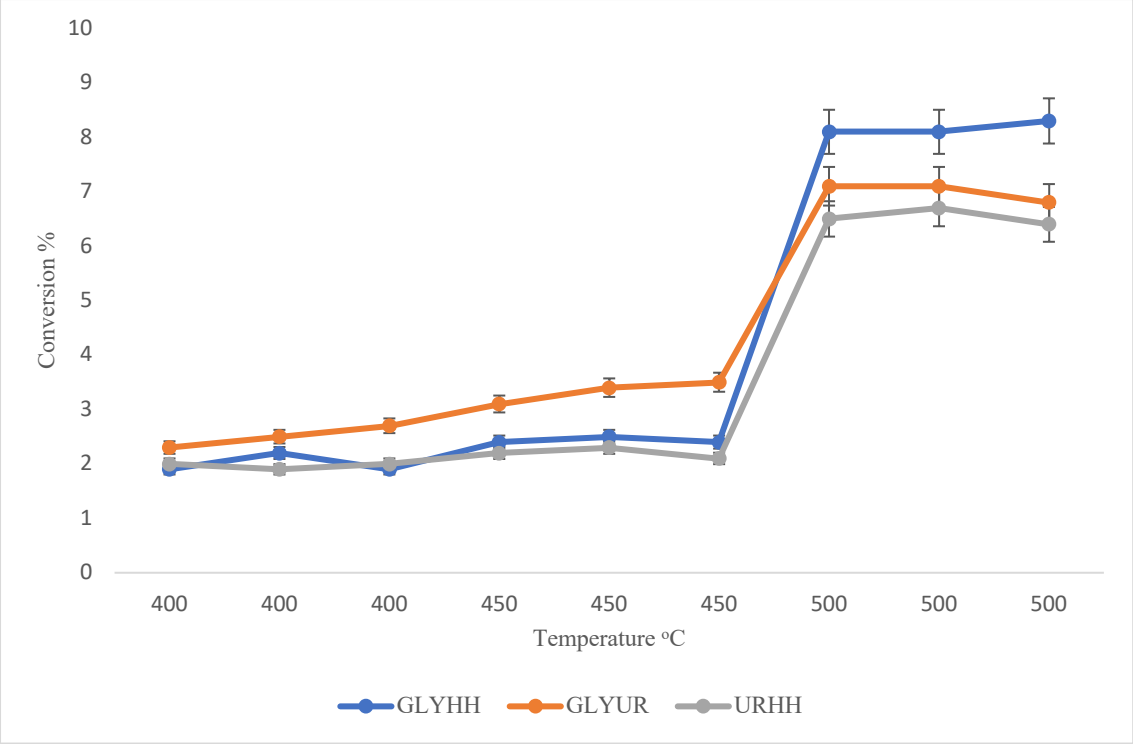

Figure 5.1**:** Conversion of *n*-octane over MgO catalysts. *(A)* GLY/HH, *(B)* GLY/UR and *(C)* UR/HH **(**Reaction conditions: Temperature = (400-500 °C), Feed = 12% *n*-octane, C: O = 8:2 and GHSV = 8005 h^{-1})

Figure 5.2 shows the selectivity profiles of the MgO catalysts. The GLY/HH catalysts showed an increase in octene formation (±4% at 400 °C to ±9% at 500 °C). This was attributed to the shorter residence time of *n*-octane on the surface of the catalyst, resulting in enhanced octene formation (Elkhalifa *et al*., 2014). At 500 °C, there was an increase in the octene selectivity for all three catalysts. This is attributed to adsorption and desorption kinetics. Higher temperatures can enhance the rates of both adsorption and desorption processes, leading to more efficient utilization of active catalytic sites and faster turnover of reactants into products (Dasireddy *et al.,* 2012). For the GLY/UR and UR/HH catalysts, the octene selectivity was ±13% and ±7%, respectively, at 500 °C. The slight increase in octene selectivity is likely due to the contribution of homogeneous gas phase reactions (Elkhalifa and Friedrich, 2014). The aromatization of *n*-octane over MgO is poor, which further suggests that the reduction–oxidation cycle over MgO is slow or unfavourable. This is consistent with the fact that Mg^{2+} is a very electropositive cation (Dasireddy *et al*., 2014). The strong basicity of the MgO catalysts allows them to facilitate the oxidation of hydrocarbons to produce oxygenated compounds, which, apart from CO_x were also present. The selectivity towards oxygenates increased with increasing temperature, suggesting that gas phase cracking of *n*-octane via collisions with gaseous oxygen radicals could have occurred. MgO is usually classified as a basic support that promotes gas phase cracking at higher temperatures (Padayachee *et al*., 2015). The same type of pattern was observed in this study. Carbon oxides were the dominant products at all temperatures tested.

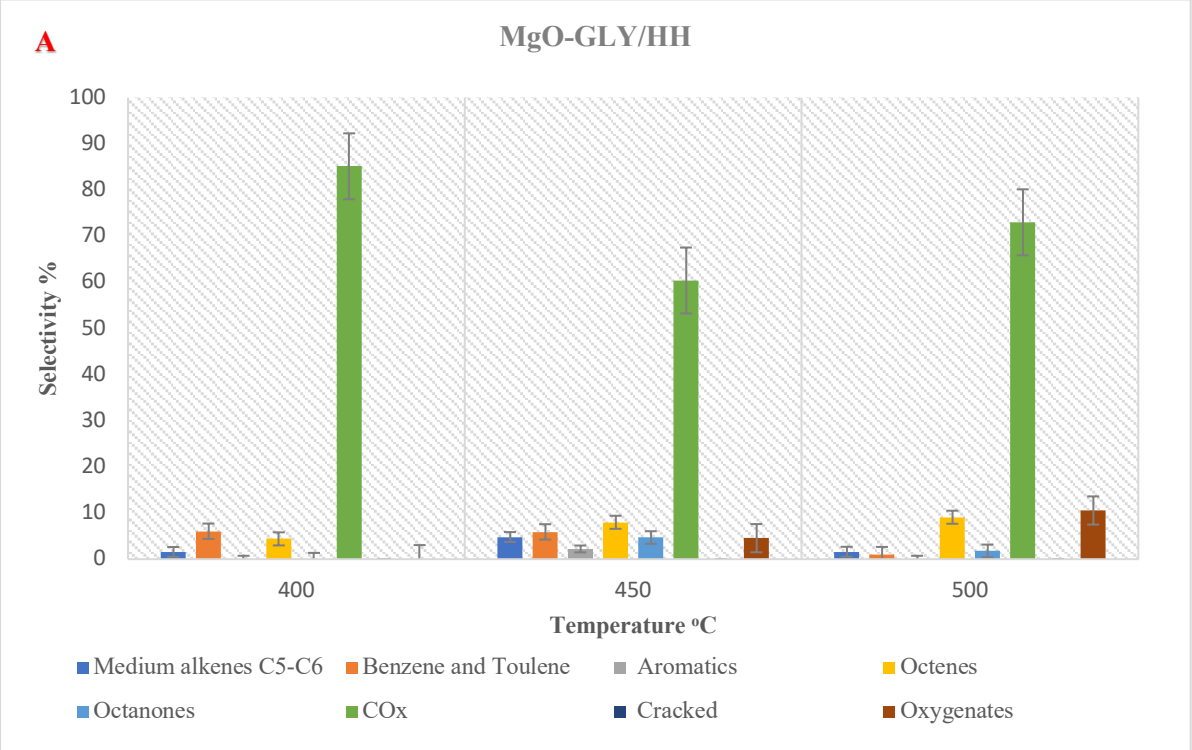
A
MgO-GLY/HH
Selectivity %
100
90
80
70
60
50
40
30
20
10
0
400
450
500
Temperature °C
Medium alkenes C5-C6
Benzene and Toulene
Aromatics
Octenes
Octanones
COx
Cracked
Oxygenates

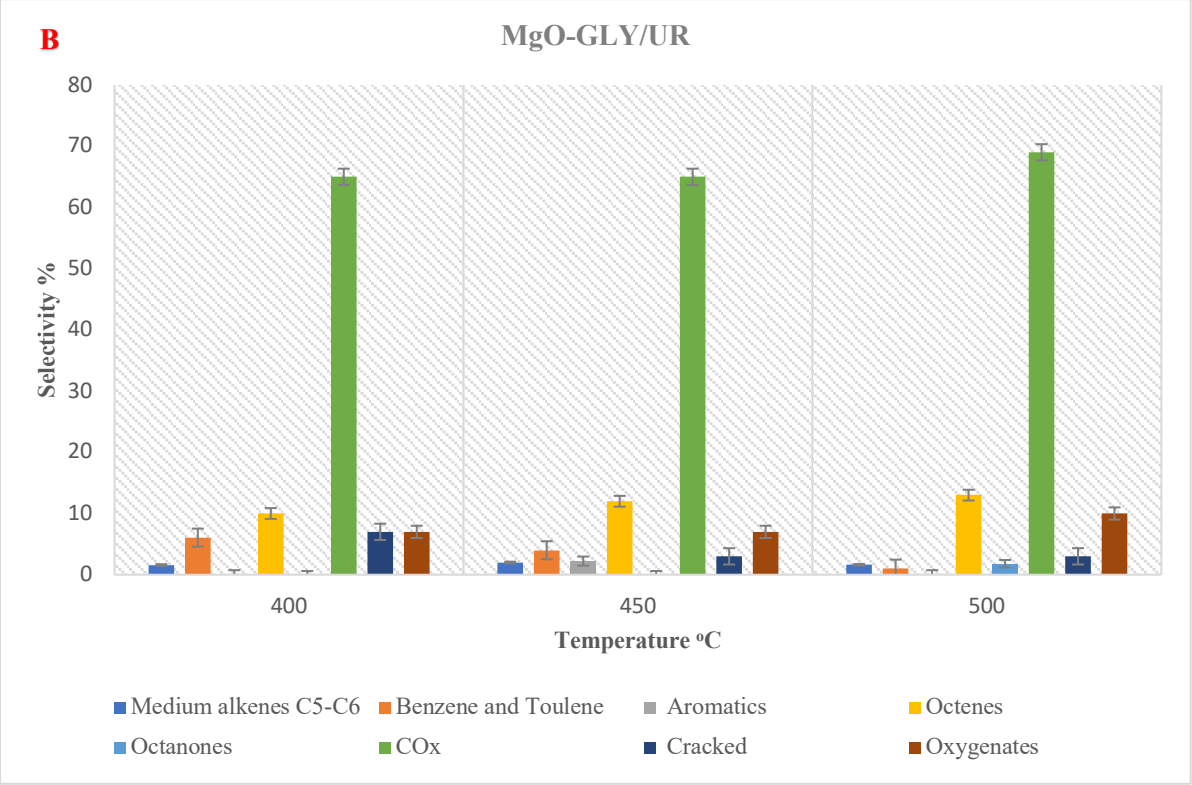
B
MgO-GLY/UR
Selectivity %
80
70
60
50
40
30
20
10
0
400
450
500
Temperature °C
Medium alkenes C5-C6
Benzene and Toulene
Aromatics
Octenes
Octanones
COx
Cracked
Oxygenates

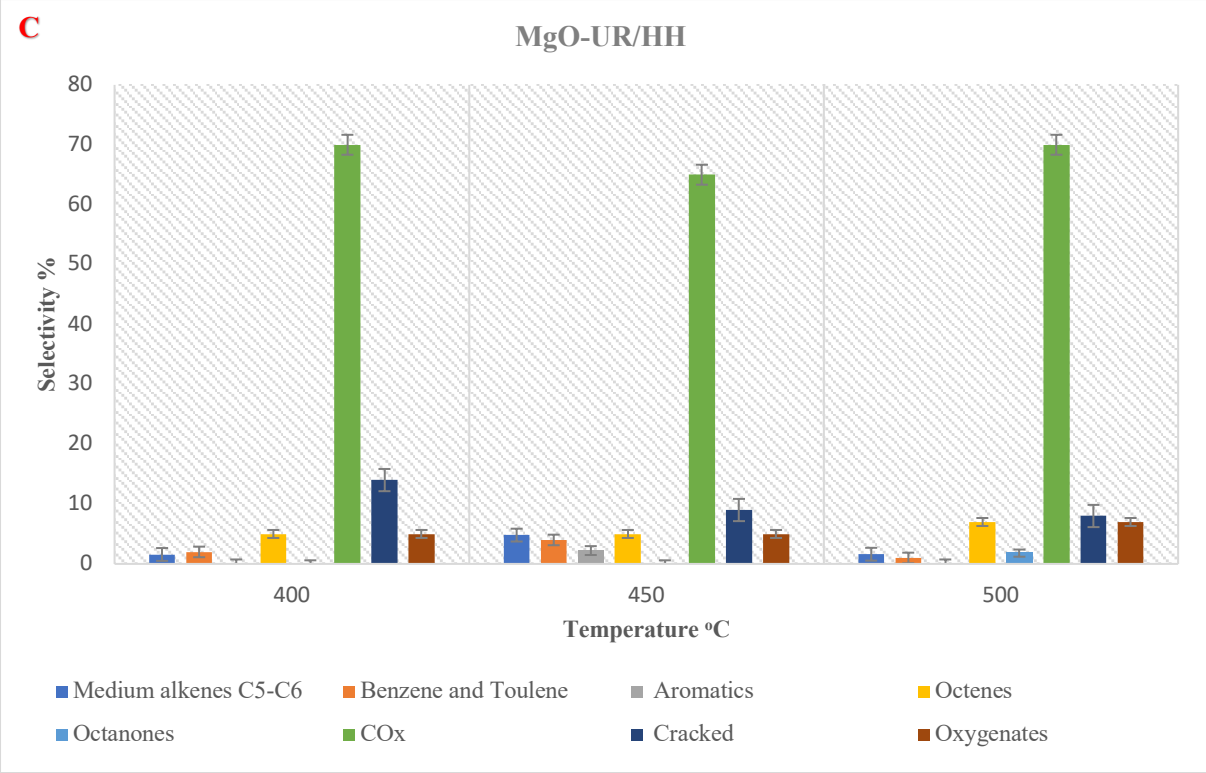

Figure 5.2**:** Selectivity as a function of temperature over MgO catalysts. *(A)* GLY/HH, *(B)* GLY/UR and *(C)* UR/HH (Reaction conditions: Temperature = (400-500 °C), Feed = 12% *n*-octane, C: O = 8:2 and GHSV = 8005 h^{-1})

5.2 VO_x/MgO catalysts

Figure 5.3 displays the *n*-octane conversion over the VO_x/MgO catalysts at 400, 450 and 500 ºC. The increase in conversion as a function of temperature was slightly more pronounced for the VO_x/MgO catalyst that was tested under the same reaction conditions used for the MgO catalysts. The GLY/HH catalyst ***(A)*** and GLY/UR catalyst ***(B)*** catalysts had the highest conversions of 15-16% at 500 ºC. The addition of 15 wt% V_2O_5 to MgO allowed for the availability of active sites, which are attributed to multiple stable oxidation states that increase redox properties during ODH reactions.

At low temperatures, the thermal activation of *n*-octane does not occur, which reduces the catalytic activity of the catalyst and further lowers the conversion over each VO_x/MgO (Elkhalifa *et al*., 2019). The UR/HH catalyst has the lowest conversion at 400 ºC. This is attributed to fewer active sites being present on the catalyst surface. The conversion gradually increased from 450 ºC to 500 ºC for all three VO_x/MgO catalysts. This is directly related to the phase composition of each catalyst, more specifically, the magnesium vanadate phases present in each catalyst. The different phases of these magnesium vanadate phases are known to influence the rate of conversion. Both magnesium orthovanadate and

magnesium pyrovanadate can exist in different crystalline phases, including different polymorphs and crystal structures (Elkhalifa *et al*., 2019). In general, the catalytic activity and conversion rate of these materials can be influenced by the crystalline phase. For example, a study of magnesium orthovanadate polymorphs demonstrated that the γ-phase had a higher activity than the α-phase, leading to a higher conversion rate (Elkhalifa *et al*., 2019). All catalysts displayed an increase in % conversion, but the highest % conversion was shown for the GLY/UR catalyst. The GLY/UR catalyst was also the only catalyst that displayed crystalline phases for both magnesium orthovanadate and pyrovanadate according to the XRD refinement data. The catalytic activity and conversion rates are directly associated with the phases formed in each VO_x/MgO catalyst. The other two catalysts showed one crystalline phase (magnesium orthovanadate), hence the lower conversions.

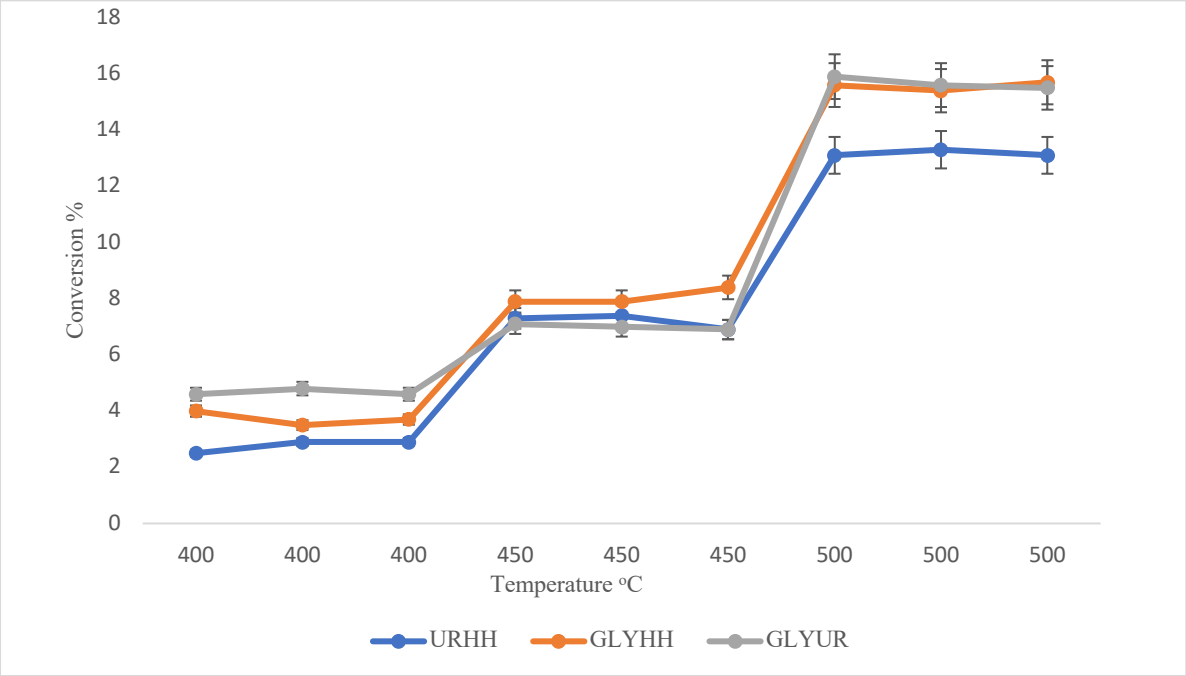

Figure 5.3**:** Conversion of *n*-octane over VO_x/MgO catalysts. *(A)* GLY/HH, *(B)* GLY/UR and *(C)* UR/HH **(**Reaction conditions: Temperature = (400-500 °C), Feed = 12% *n*-octane, C:O = 8:2 and GHSV = 8005 h^{-1})

Figure 5.4 shows the selectivity profiles of the VO_x/MgO catalysts, with octene isomers and CO_x being the dominant products in the GLY/HH catalyst ***(A)***, with minimal contributions from C7 aromatics, cracked products and cracked oxygenates. The selectivity profile of the GLY/UR catalyst ***(B)*** showed that octenes and CO_x were the dominant products, with minimal contributions from C7 aromatics, cracked products and oxygenates. The same was observed for the UR/HH catalyst (***C***). The selectivity for octene was 54% over GLY/HH and GLY/UR and lower for UR/HH at 49%.at 500 °C. The low selectivity towards cracked oxygenates over the GLY/HH and GLY/UR catalysts suggested that activated octenes formed on the surface of these catalysts favoured the dehydrocyclization mechanism

(Fadalla *et al.,* 2018). This led to the formation of aromatics, while in the UR/HH catalyst, an oxygen insertion reaction occurred, which led to the formation of cracked oxygenated compounds (Padayachee *et al.,* 2012). Its redox properties, particularly the morphological structure of the phases formed, are all associated with the catalyst selectivity.

According to the TPR results, the GLY/HH catalyst displayed two reduction peaks and was easily reducible. These easily reduced sites can promote the activation of the reactants, enabling them to undergo the ODH reactions more efficiently. The VO_x in the VO_x/MgO catalyst can exist in different oxidation states, viz., V^{5+} and V^{4+}. In addition to its redox properties, its larger surface area could be used to explain its high selectivity for octenes and aromatics at high temperatures. In addition, higher selectivities are associated with alkenes being adsorbed onto the catalyst surface at a shorter residence time, decreasing the chances for undesirable reactions, such as the formation of secondary combustion products and cracking or secondary combustion of CO_x (Ntola *et al.,* 2023*)*. Due to the quick reaction time during the SCS reaction, there was only the formation of a single magnesium orthovanadate phase formed in both the GLY/HH and UR/HH catalysts, which agrees with the XRD data and Rietveld refinement. Thus, VO_x/MgO catalysts with higher V^{4+}/V^{5+} ratios can have higher catalytic activity and conversion (Ilyina *et al.,* 2013). The SCS method creates a highly dispersed distribution of the VO_x species on the MgO support surface. This homogeneous distribution of vanadium and magnesium species provides an optimal ratio of active sites for support, allowing for an efficient *n*-octane conversion process (Elkhalifa and Friedrich, 2018). The highly dispersed VO_x on the MgO support surface results in a greater number of exposed vanadium species (Ntola *et al*., 2023). Compared to other products, these exposed vanadium species selectively react with *n*-octane to form octenes.

The GLY/UR catalyst also had a selectivity of 54% for octenes at 500 ºC, which is attributed to it being the only VO_x/MgO catalyst that formed both the magnesium orthovanadate and magnesium pyrovanadate phases. During the oxidative dehydrogenation of alkanes, thermal cracking leads to the formation of CO_x. Unfortunately, this process reduces the selectivity of the catalyst towards the desired olefins and aromatics. Additionally, the VO_x species on the catalyst surface can react with alkanes, resulting in the production of carbon dioxide instead of the desired double bond formation. As a consequence, the yields of olefins and aromatics decrease. This is evident in the catalytic data, which show a low selectivity for lower alkenes across all three mixed fuel VO_x/MgO catalysts. The GLY/HH catalyst ***(A)*** showed a selectivity of ±10% for lower alkenes, more specifically at 400 ºC and 500 ºC, respectively, and ± 5% for the UR/HH catalyst ***(C)***. The selectivity of aromatics in the ODH process is generally greater than that of lower alkenes but lower than that of octenes due to the structural morphology of the reactant molecules and the catalyst. The GLY/HH catalyst ***(A)*** and the GLY/UR catalyst ***(B)*** had a selectivity of above 10% for aromatics, while for the UR/HH catalyst ***(C),*** this was again observed at ± 5%. The oxygen selectivity increased with temperature for the UR/HH catalyst ***(C)***

only, which suggested that these ODH products underwent oxygen functionalization, possibly through an ER-type mechanism, followed by cracking, thus forming oxygenates. There was no observable variation in the selectivity towards octenes for the UR/HH catalyst ***(C)***. The main products formed included 2-octenes as the dominant isomer.

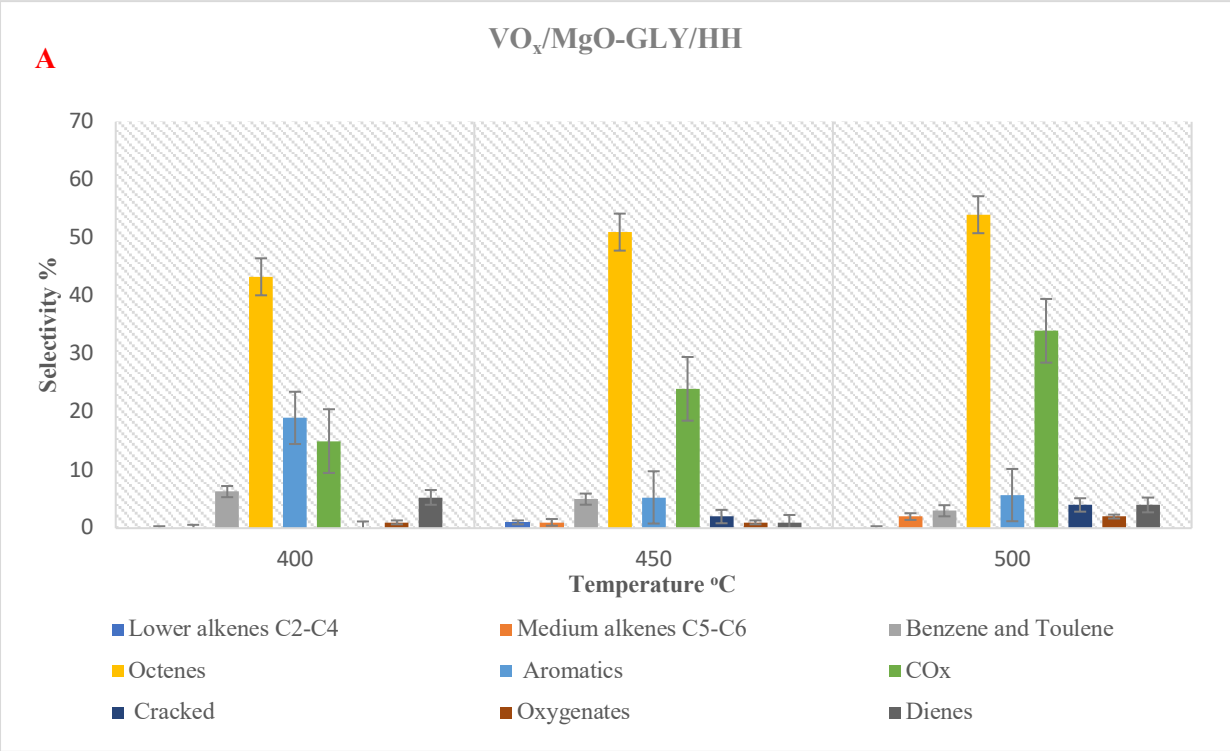

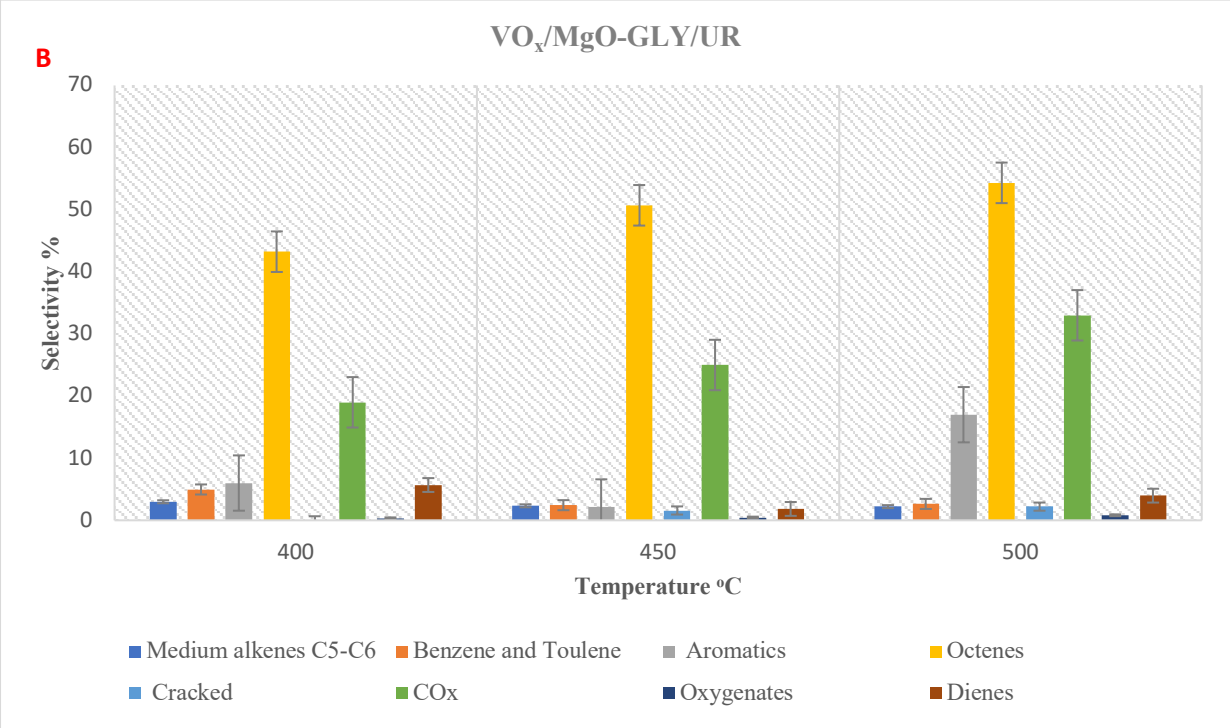

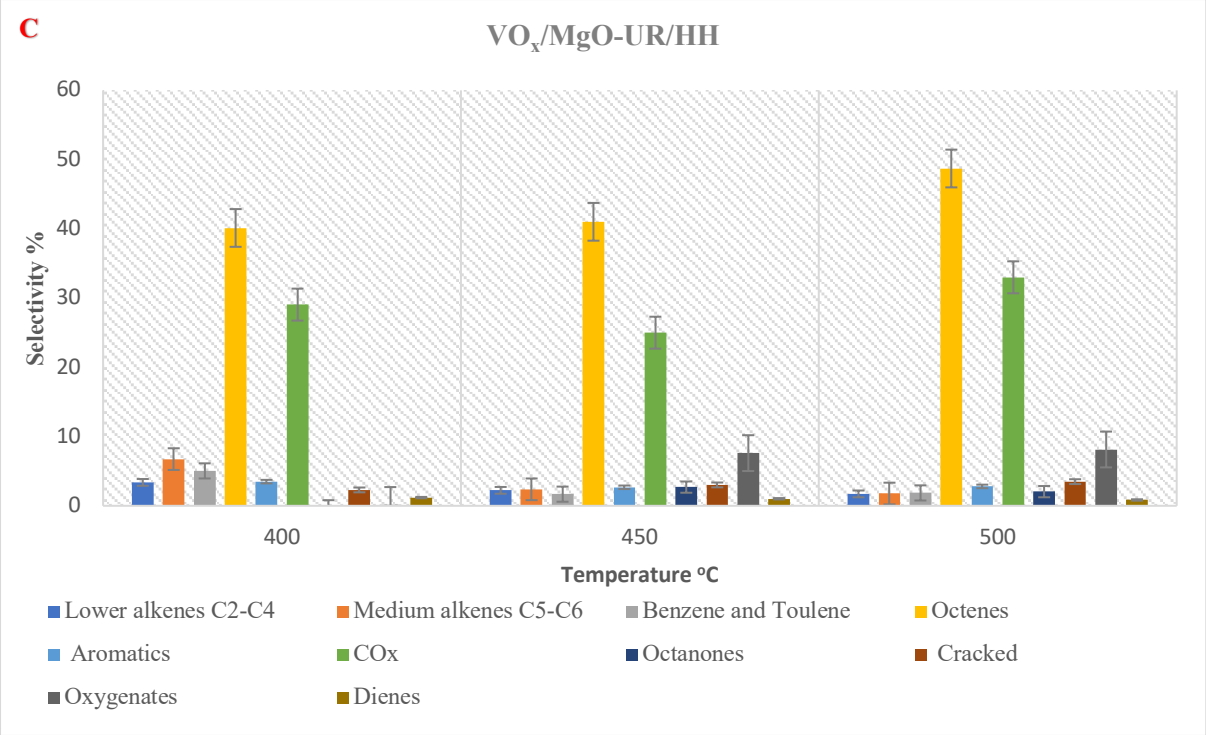

Figure 5.4: Selectivity as a function of temperature of *n*-octane conversion over VO_x/MgO catalysts prepared by mixed fuels *(A)* GLY/HH, *(B)* GLY/UR and *(C)* UR/HH (Reaction conditions: Temperature = (400-500 °C), Feed = 12% *n*-octane, C:O = 8:2 and GHSV = 8005 h^{-1})

5.3 Influence of the feed ratio

Figure 5.5 displays the variation in the conversion with temperature over a dilute feed. 1-2% was obtained over all three VO_x/MgO catalysts at 350 °C. At higher temperatures, the conversion increased. However, if the temperature is too high, the catalyst may undergo deactivation due to thermal instability or metal sintering. The feed concentration, which was decreased from 12% to 5% *n*-octane in air and diluted with nitrogen, was the only parameter that was varied. This was used to determine the effect of feed concentration on the conversion of *n*-octane. At a 5% feed composition and 450 °C, the conversion was 8% for the GLY/UR catalyst and 10% for the GLY/HH catalyst. Under the same reaction conditions with 12% *n*-octane, conversions of 7% for the GLY/UR catalyst and 8% for the GLY/HH catalyst were obtained. At low feed concentrations, the reaction rate decreases since fewer reactants are available to participate in the reaction. Beyond a specific concentration, the reaction rate plateaus since the catalyst becomes saturated and cannot absorb further reactants (Padayachee *et al*., 2019).

In this study, a 5% feed concentration suggested an optimal reaction rate in conjunction with the operating temperature. In addition to the factors mentioned above, redox properties play a critical role in the *n*-octane conversion. In this catalytic system, vanadium oxide exists in the +4-oxidation state,

which is reduced to the +3-oxidation state during the reaction (Elkhalifa *et al*., 2019). Acid-base properties also influence the conversion of *n*-octane. Magnesium oxide has several Lewis acid sites that enhance the acidity of the catalyst (Padayachee *et al*., 2015). These acidic sites can interact with negatively charged functional groups of reactants to activate them and facilitate their reaction with other species (Padayachee *et al*., 2015). The basic sites on the catalyst, such as hydroxyl groups, can abstract protons from the reacting species, thereby promoting the reaction. Therefore, the VO_x/MgO catalyst can exhibit both acidic and basic properties. The greater conversion achieved over the GLY/HH catalyst can be related to the greater dispersion of VO_x on the surface of the catalyst and hence the greater availability of gaseous *n*-octane molecules. The active VO_x species would have been distributed throughout the structural lattice of the GLY/UR catalyst and as a result, not all of these species would have been available to the reactant (Padayachee *et al.,* 2015). Even though the GLY/HH catalyst showed the highest conversion, it was still relatively low, considering that the highest temperature was 450 °C.

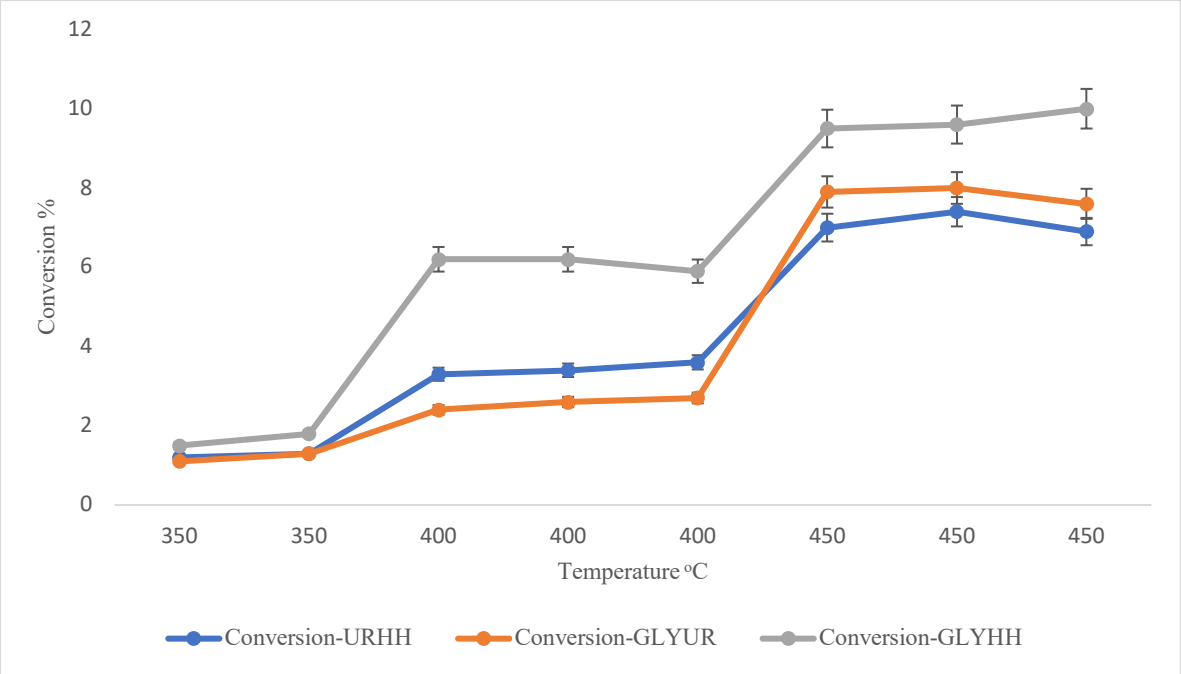

Figure 5.5**:** Conversion of *n*-octane over the VO_x/MgO catalysts. *(A)* GLY/HH, *(B)* GLY/UR and *(C)* UR/HH **(**Reaction conditions: Temperature = (350-450 °C), Feed = 5% *n*-octane, C: O = 8:2 and GHSV = 8005 h^{-1})

Figure 5.6 shows the selectivity for octenes as a function of temperature. At temperatures between 350 °C and 400 °C, low conversions were recorded, but these rapidly increased from 400 °C to 450 °C. At temperatures between 400 °C and 450 °C, the thermal energy provided enables more efficient activation of reactant molecules, facilitating their interaction with the catalyst surface (Dasireddy *et al*., 2012). The selectivity to octenes was greater over the GLY/UR and GLY/HH catalysts and almost comparable over the UR/HH catalyst, when comparing the 5% and 12% *n*-octane concentrations, especially at 450 °C. The formation of C8 aromatics was observed over the GLY/UR catalyst, with a selectivity of ±10%

and was observed only at 350 ºC. The dominant products of the GLY/HH and UR/HH catalysts were octenes, carbon oxides and cracking products. The selectivity for CO_x decreased from 350 to 450 ºC for the GLY/HH and GLY/UR catalysts, in contrast to an increase at the temperatures 350 ºC and 450 ºC for the UR/HH catalyst. The high Brønsted acidity for all three supported VO_x/MgO catalysts resulted in a longer residence time of the adsorbate, facilitating secondary combustion of the formed C8 alkenes or aromatics to increase the CO_x selectivity. On such surfaces, the formed alkenes or aromatics are likely to be held for a longer time on the catalyst surface, increasing the likelihood of the combustion of these products to produce CO_x. The selectivity for cracking products (C1 to C7 alkanes and alkenes) was minimal at ±5% in the temperature range of 350-450 ºC.

The 5% (v/v) *n*-octane-in air and N_2 show better selectivity for octenes than the 12% (v/v) ratio due to the lower likelihood of side reactions, faster reaction kinetics, and better diffusion and mixing of reactants. These factors contribute to the selectivity of the reaction towards the desired products (Ramirez *et al.,* 2019). Based on this, the catalysts prepared from the fuel mixtures GLY/HH and GLY/UR had the highest selectivity for octenes at 450 ºC, which were 59% and 62%, respectively, with the UR/HH catalyst displaying a selectivity of 48%. The enhanced selectivity towards octenes observed over VO_x/MgO catalysts synthesized using glycine can be attributed to several factors. First, a smaller particle size and increased surface area can provide more active sites for the reaction (Ntola *et al*., 2023). Second, the use of glycine can help stabilize certain crystal structures, such as the orthorhombic phase of VO_x, which is known to be responsible for high selectivities towards octenes (Valenzuela *et al*., 2000). At 350 ºC, all three catalysts showed selectivity for octenes. This again can be attributed to the distribution of VO_x over the MgO support, which allowed sufficient active sites. Even with the enhanced octene selectivity, the percentages of lower alkenes, medium alkenes, and aromatics were ±10% for all three catalysts. The UR/HH catalyst showed a decrease in selectivity towards octenes with increasing temperature. Once hydrogen abstraction from *n*-octane occurred, the resultant octenes could have either desorbed from the surface of the catalyst or served as reaction intermediates for the formation of other ODH products.

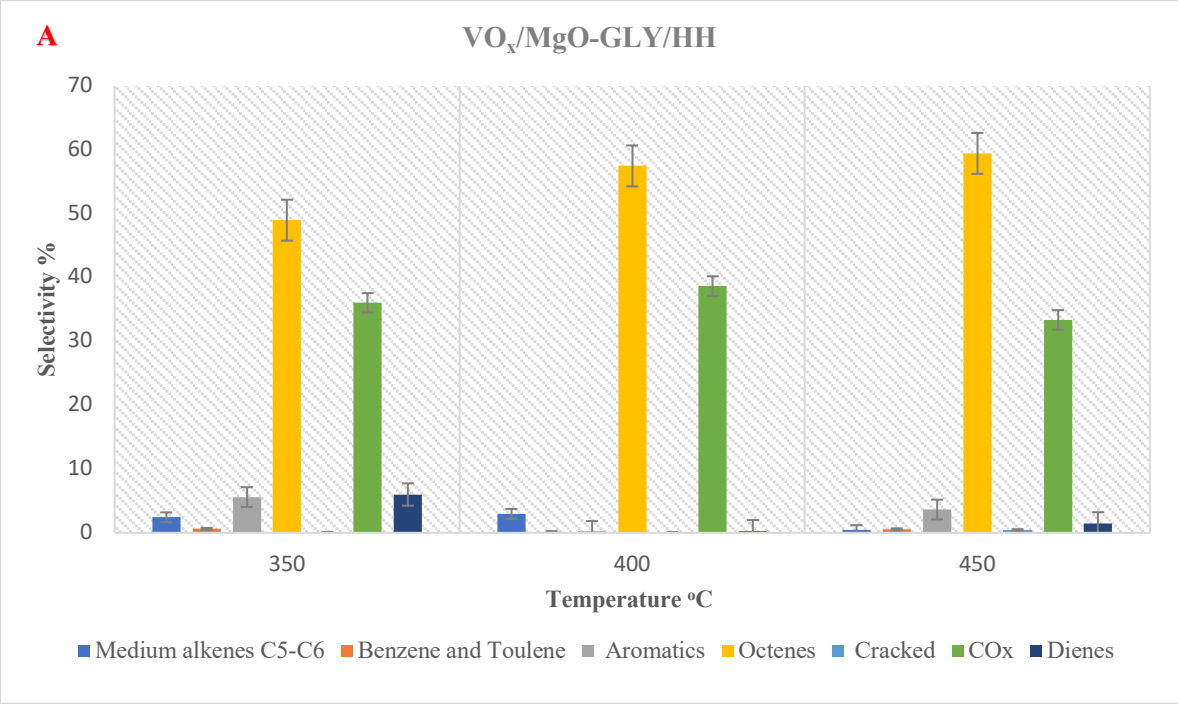
A
VOx/MgO-GLY/HH
Selectivity %
70
60
50
40
30
20
10
0
350
400
450
Temperature °C
Medium alkenes C5-C6
Benzene and Toulene
Aromatics
Octenes
Cracked
COx
Dienes

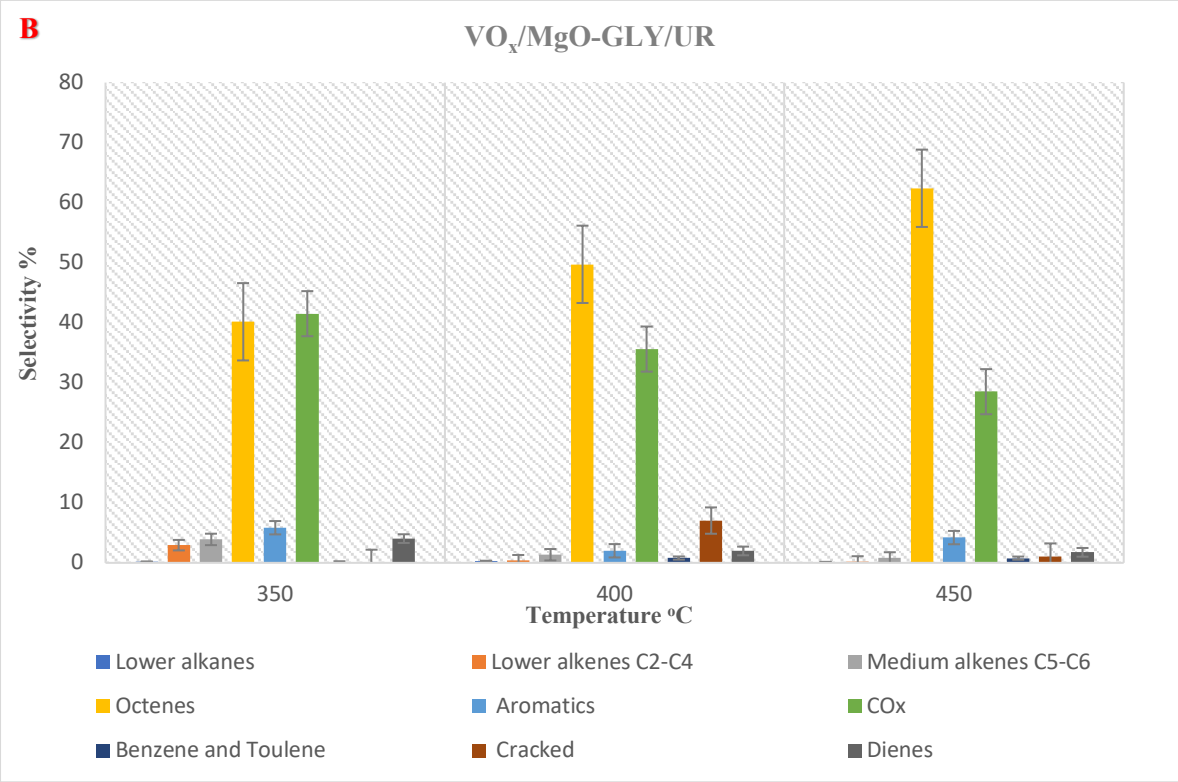
B
VOx/MgO-GLY/UR
Selectivity %
80
70
60
50
40
30
20
10
0
350
400
450
Temperature °C
Lower alkanes
Lower alkenes C2-C4
Medium alkenes C5-C6
Octenes
Aromatics
COx
Benzene and Toulene
Cracked
Dienes

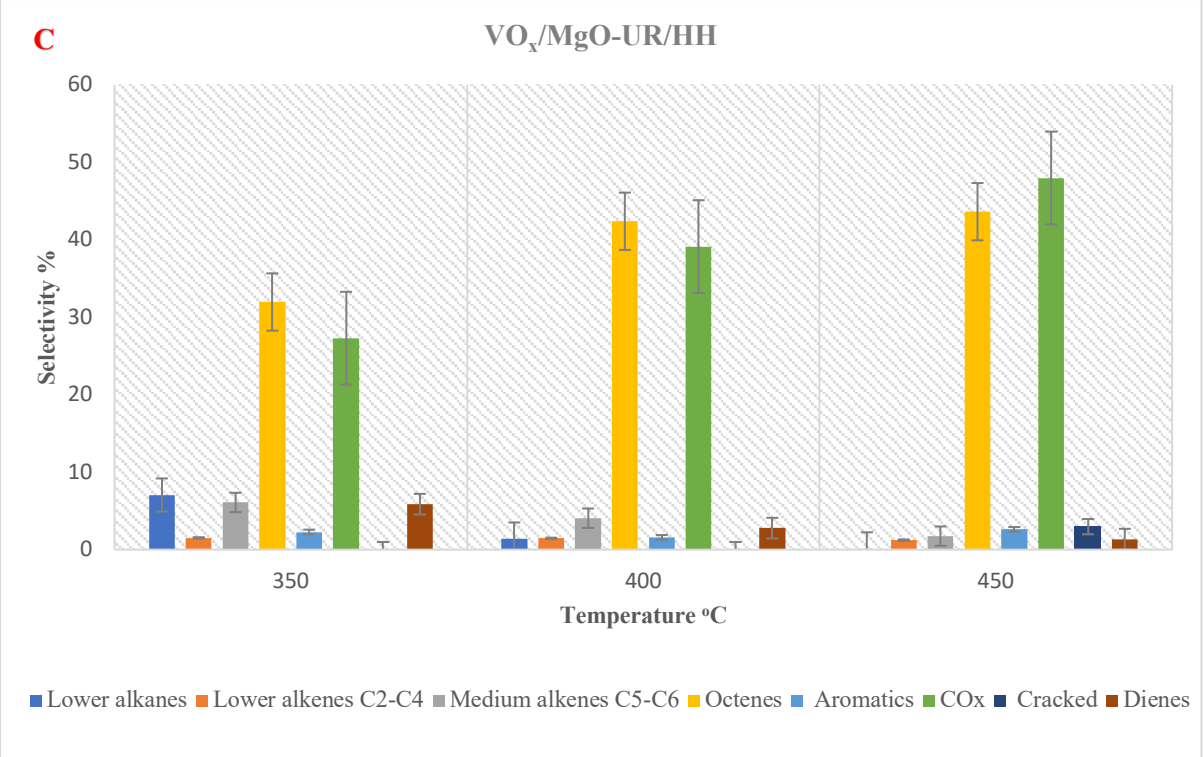

Figure 5.6**:** Selectivity as a function of temperature over the VO_x/MgO catalysts**.** *(A)* GLY/HH, *(B)* GLY/UR and *(C)* UR/HH (Reaction conditions: Temperature = (350-500 °C), Feed = 5% *n*-octane, C:O = 8:2 and GHSV = 8005 h^{-1})

Figure 5.7 shows the octene selectivity at 5% (v/v) *n*-octane feed for all three supported VO_x/MgO catalysts. The highest octene selectivity was observed for the GLY/UR and GLY/HH catalysts, while the UR/HH catalyst displayed the lowest octene formation. However, all three catalysts showed an increase in octene selectivity as the temperature increased. A lower *n*-octane concentration in the system will minimize the probability of forming side products, leading to enhanced selectivity towards octenes (Bugler, 2017). Second, the reaction kinetics of octene formation from *n*-octane are relatively fast; as such, it can proceed effectively with a lower *n*-octane concentration (Bugler, 2017). At high *n*-octane concentrations, the rate of the reaction may decrease due to mass transfer limitations, which can cause the reaction intermediates to build up excessively and can lead to side reactions (Pruker *et al.,* 2022). Lower *n*-octane concentrations can help overcome these limitations, thereby facilitating faster reactions and leading to higher octene selectivity. Finally, the mixing and diffusion of reactants are crucial factors that affect the selectivity of the reaction. With a lower concentration of reactants, the mixing of the reactants becomes easier, allowing for better contact between the reactants and the catalyst (Schwarze et al., 2015).

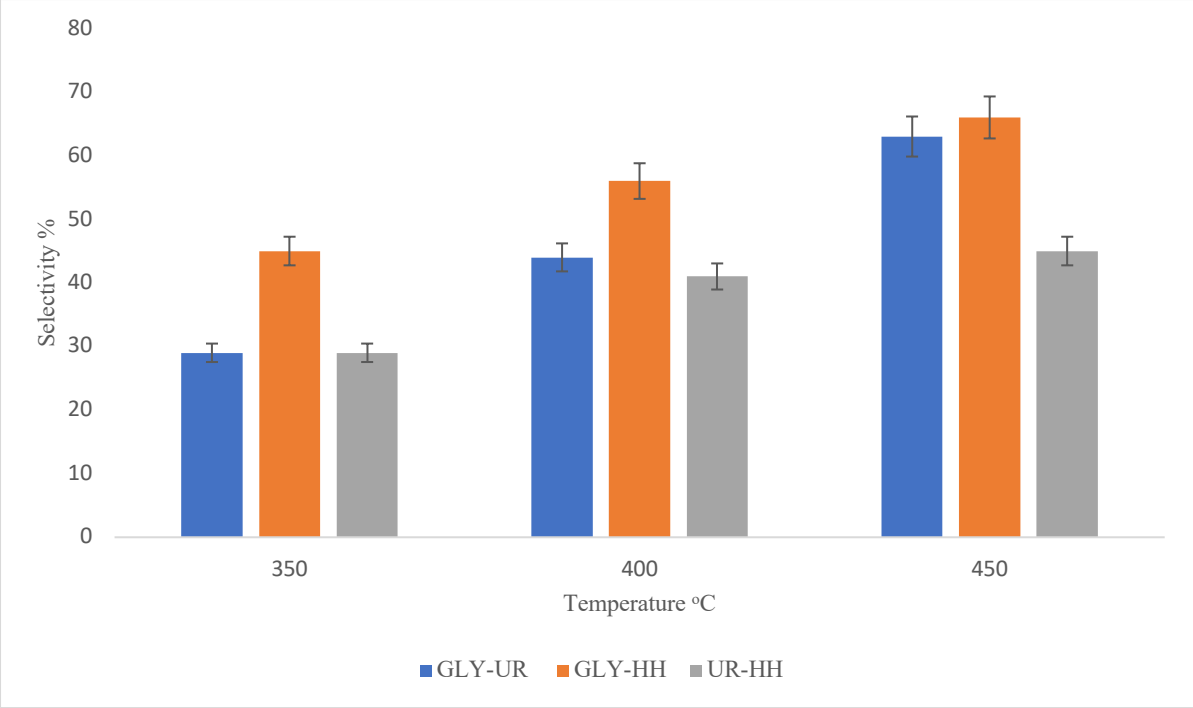

Figure 5.7**:** Octene **s**electivity over the VO_x/MgO catalysts with the 5% *n*-octane feed as a function of temperature (Reaction conditions: Temperature = (350 °C-450 °C), Feed = 5% n-octane, C:O = 8:2 and GHSV = 8002 h^{-1}

Figure 5.8 shows iso-conversion data of the GLY/UR and GLY/HH catalysts, which allows the comparison of the materials without conversion or thermal effects. To achieve an isothermal iso-conversion, the GHSV of the reactions were varied until conversions were within a 1% range of each other. The selectivity to octenes was 40% and 45% for the GLY/UR and GLY/HH catalysts respectively. At the higher GHSV, both catalysts showed an increase in selectivity towards aromatics, although the GLY/UR catalyst showed a higher selectivity of 25%. According to Elkhalifa and Friedrich *et al*. (2011), a relatively slow desorption of the (basic) octenes from the catalyst surface lowers their selectivity but at the same time causes the aromatics selectivity to increase. This is done by providing more chance for the formed octenes to be oxidized further to give the corresponding aromatics (Elkhalifa and Friedrich *et al*., 2011). The slow desorption of the octenes from the catalyst surface for the GLY/UR catalyst was attributed to the strong Brønsted acid sites and its phasic composition. An increase in the selectivity to C-8 products was seen as the temperature was increased from 450 °C-500 °C. This is consistent with literature suggesting that an increase in temperature favours the formation of aromatic compounds (Ntola *et al*., 2023). This increase is reported to be due to the fact that the non-selective oxygen species are usually more active at lower temperatures than the selective oxygen species (Elkhalifa *et al*., 2011).

Aromatic compounds are attributed to cyclization, which would lead to the formation of aromatics, providing an energetically favourable pathway for the reaction, minimizing CO_x formation (Ntola *et al*., 2023). This correlates to the low formation of CO_x as seen in Figure 5.8.

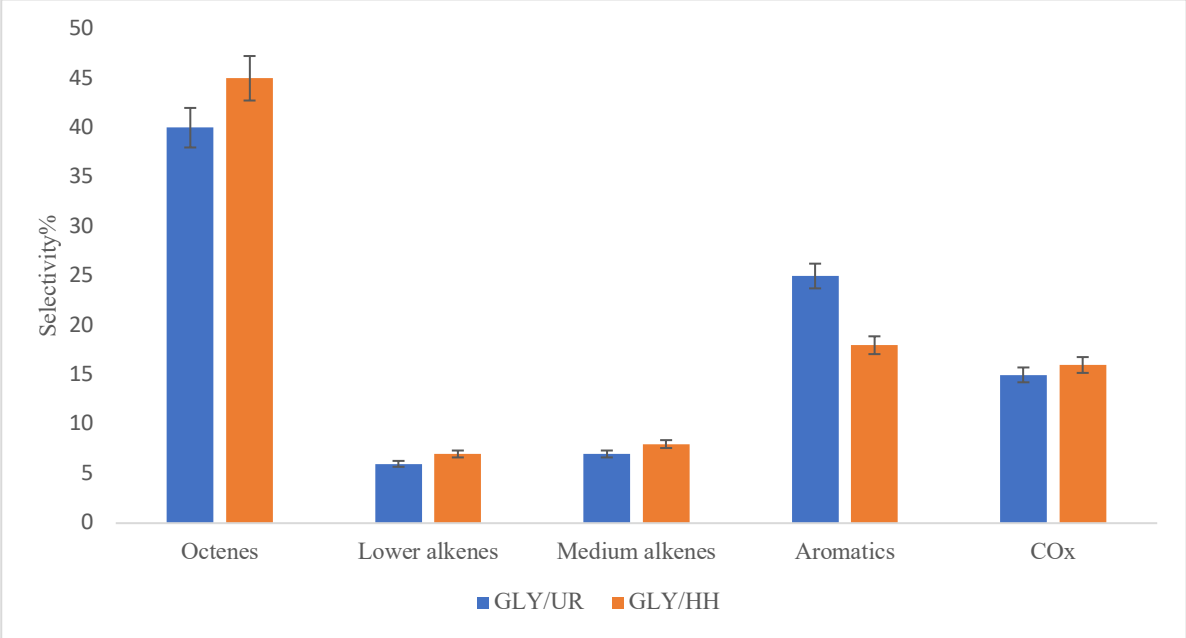

Figure 5.8: Selectivity at iso-conversion at 450 °C over the VO_x/MgO catalysts prepared by mixed fuels (A) GLY/HH, (B) GLY/UR (Reaction conditions: Temperature = 450 °C, Feed = 12% *n*-octane, C:O: 8:2 and GHSV: GLY/UR = 10082 h^{-1} and GLY/HH =11139 h^{-1}

CHAPTER 6: CONCLUSIONS AND RECOMMENDATIONS

The aim of this study was to synthesize supported vanadium catalysts for the ODH of *n*-octane to value-added olefins and aromatics. VO_x/MgO and MgO catalysts were prepared using the SCS method with fuel mixtures of 50/50 using GLY/UR, GLY/HH and UR/HH. ICP-OES was used to confirm the wt. % V_2O_5 loading. X-ray diffraction (XRD) and Rietveld refinement analysis of the VO_x/MgO catalysts showed a relative phase abundance of 82% for the periclase phase and 17% for the magnesium orthovanadate phase in the GLY/HH, while the UR/HH catalyst displayed a relative phase abundance of 75% periclase and 24% magnesium orthovanadate. The GLY/UR catalyst displayed a relative phase abundance of 78% for the periclase phase and 15.6% for the magnesium orthovanadate phase, and it was the only catalyst that contained the pyrovanadate phase with a relative abundance of 5.3%. The rapid combustion of the GLY/HH and UR/HH catalysts could be attributed to the absence of the crystalline pyrovanadate phase. BET analysis showed a decrease in the surface area and pore volume of the VO_x/MgO catalysts compared to those of the MgO supports.

Transmission electron microscopy (TEM) was used to determine the structural morphology. The results showed that the GLY/HH catalyst had uniformly packed small porous particles, followed by larger particles for the GLY/UR catalyst, and large faceted particles for the UR/HH catalyst. SEM-EDX analysis was used to determine the distribution of VO_x on the MgO support and showed evenly distributed VO_x species for the GLY/HH catalyst and cluster formation for the GLY/UR and UR/HH catalysts. TPR studies were performed to investigate the redox nature of the VO_x species present in the catalysts, which showed reduction properties similar to those of single fuel materials. TPR analysis of the GLY/UR and GLY/HH catalysts further showed two reduction peaks of the V^{4+} and V^{5+} species, whereas UR/HH displayed one reduction peak. TPD-MS was used to determine the acid/base properties of each catalyst. All three supported VO_x/MgO materials showed strong Brønsted acid sites. The UR/HH catalyst showed the highest concentration of Brønsted acid sites.

The catalytic testing results of the MgO supports showed that carbon oxides (CO_x) were dominant products over the temperature range of 400–500 °C. The highest selectivity of ± 13% was observed for octenes using the GLY/UR catalyst while the GLY/HH catalyst showed a selectivity of ±9%. The VO_x/MgO catalysts showed an increase in *n*-octane conversion and selectivity towards value-added octenes for all three catalysts at all the temperatures tested. Other products formed included lower alkenes and medium chain alkenes, with selectivities of ±5%, and the conversion and selectivity of these catalysts were found to be sensitive to the reaction conditions. A decrease in the feed concentration from 12% to 5% led to an increase in the amount of octenes, specifically at 450 °C, which was observed only for the VO_x/MgO catalysts. The results further showed that the morphology and the crystallite size of the catalysts were dependent on the flame temperature during the combustion. For example, the

addition of urea to glycine decreased the combustion temperature, which resulted in different the structural morphologies, surface areas, phase compositions and the acid/base properties for all three VO_x/MgO catalysts. These differences were evident in the catalytic testing.

In future investigations, various fuel-to-oxidizer ratios can be explored to optimize the catalyst properties, including morphological characteristics, compositional variations, and crucial redox features. By carefully tuning these parameters, one can uncover the underlying chemical processes driving these transformations. Furthermore, a thorough characterization of the used catalysts would provide critical insights. The use of tools such as XRD and electron microscopy enables a comprehensive examination of catalyst composition and structural intricacies. Additionally, the integration of thermocouple technology facilitates real-time monitoring of temperature fluctuations during catalyst preparation, providing valuable insights into their profound impact on phase development and composition, as opposed to estimating adiabatic flame temperatures. These analyses serve as the foundation of our research efforts, facilitating informed decision-making and strategic enhancement of catalyst synthesis methodologies.

REFERENCES

Al-Ghamdi, S.A. and de Lasa, H.I., 2014. Propylene production via propane oxidative dehydrogenation over VO_x/γ-Al_2O_3 catalyst. *Fuel*, *128*, pp.120-140.

Amirkhanyan, N., Kharatyan, S., Manukyan, K. and Aprahamian, A., 2020. Thermodynamics and kinetics of solution combustion synthesis: $Ni(NO_3)_2$+ fuels systems. *Combustion and Flame*, *221*, pp.110-119.

Arias, P.L., Cecilia, J.A., Gandarias, I., Iglesias, J., Granados, M.L., Mariscal, R., Morales, G., Moreno-Tost, R. and Maireles-Torres, P., 2020. Oxidation of lignocellulosic platform molecules to value-added chemicals using heterogeneous catalytic technologies. *Catalysis Science & Technology*, *10*, pp. 2721-2757.

Awan, I.Z., Tanchoux, N., Quignard, F., Albonetti, S., Cavani, F. and Di Renzo, F., 2019. Heterogeneous catalysis as a tool for production of aromatic compounds from lignin. *Studies in Surface Science and Catalysis*, *178(13),* pp. 257-275.

Bai, J., Meng, F., Wei, C., Zhao, Y., Tan, H. and Liu, J., 2011. Solution combustion synthesis and characteristics of nanoscale MgO powders. *Ceramics-Silikaty*, *55* (1), pp.20-25.

Basso, A. and Serban, S., 2019. Industrial applications of immobilized enzymes. A review. *Molecular Catalysis*, *479 (5)*, pp.110607.

Bijani, P.M., Sohrabi, M. and Sahebdelfar, S., 2014. Nonoxidative aromatization of CH_4 using C_3H_8 as a coreactant: thermodynamic and experimental analysis. *Industrial & Engineering Chemistry Research*, *53* (2), pp 572-581.

Bond, J.Q., Upadhye, A.A., Olcay, H., Tompsett, G.A., Jae, J., Xing, R., Alonso, D.M., Wang, D., Zhang, T., Kumar, R. and Foster, A., 2014. Production of renewable jet fuel range alkanes and commodity chemicals from integrated catalytic processing of biomass. *Energy & Environmental Science*, *7* (4), pp.1500-1523.

Broeksma, C.P., 2018. *Evaluating the applicability of an alkaline amino acid leaching process for base and precious metal leaching from printed circuit board waste* (Doctoral dissertation, Stellenbosch University).

Bugler, K., 2017. *The catalytic oxidative dehydrogenation of n-octane over iron and other metal molybdates*, 676 (Doctoral dissertation, Cardiff University).

Carlos, E., Martins, R., Fortunato, E. and Branquinho, R., 2020. Solution combustion synthesis: towards a sustainable approach for metal oxides. *Chemistry–A European Journal*, *26* (42), pp.9099-9125.

Carter, J.H., Bere, T., Pitchers, J.R., Hewes, D.G., Vandegehuchte, B.D., Kiely, C.J., Taylor, S.H. and Hutchings, G.J., 2021. Direct and oxidative dehydrogenation of propane: from catalyst design to industrial application. *Green Chemistry*, *23* (24), pp.9747-9799.

Cavani, F. and Trifiro, F., 1999. Selective oxidation of light alkanes: interaction between the catalyst and the gas phase on different classes of catalytic materials. *Catalysis Today*, *51*(34), pp.561-580.

Chao, Z.S. and Ruckenstein, E., 2004. Noncatalytic and catalytic conversion of ethane over VMgO catalysts prepared via solid reaction or mesoporous precursors. *Journal of Catalysis*, *222* (1), pp.17-31.

Che, M. and Védrine, J.C. eds., 2012. Characterization of solid materials and heterogeneous catalysts: From structure to surface reactivity. John Wiley & Sons. *Catalysts*, *8 (17),* pp.567.

Chen, S., Chang, X., Sun, G., Zhang, T., Xu, Y., Wang, Y., Pei, C. and Gong, J., 2021. Propane dehydrogenation: catalyst development, new chemistry, and emerging technologies. *Chemical society reviews*, *50* (5), pp.3315-3354.

Chetty, J., Dasireddy, V.D., Singh, S. and Friedrich, H.B., 2017. The oxidative aromatization of n-hexane over VMgO catalysts. *Reaction Kinetics, Mechanisms and Catalysis*, *120*, pp.307-321.

Chieregato, A., Nieto, J.M.L. and Cavani, F., 2015. Mixed-oxide catalysts with vanadium as the key element for gas-phase reactions. *Coordination Chemistry Reviews*, *301*, pp.3-23.

Climent, M.J., Corma, A. and Iborra, S., 2012. Homogeneous and heterogeneous catalysts for multicomponent reactions. *RSC advances*, *2*(1), pp.16-58.

Cornils, B., Herrmann, W.A., Beller, M. and Paciello, R. eds., 2017. *Applied homogeneous catalysis with organometallic compounds: a comprehensive handbook in four volumes* (Vol. 4). John Wiley & Sons. *345 (8),* pp. 17260.

Daems, N., Sheng, X., Vankelecom, I.F. and Pescarmona, P.P., 2014. Metal-free doped carbon materials as electrocatalysts for the oxygen reduction reaction. *Journal of Materials Chemistry A*, *2* (12), pp.4085-4110.

Dasireddy, V.D., Friedrich, H.B. and Singh, S., 2015. A kinetic insight into the activation of *n*-octane with alkaline-earth metal hydroxyapatites. *South African Journal of Chemistry*, *68*, pp.195-200.

Dasireddy, V.D., Khan, F.B., Singh, S. and Friedrich, H.B., 2014. Activation of *n*-heptane: a study with VMgO catalysts. *Catalysis letters*, *144*, pp.590-597.

Dasireddy, V.D., Singh, S. and Friedrich, H.B., 2012. Oxidative dehydrogenation of *n*-octane using vanadium pentoxide-supported hydroxyapatite catalysts. *Applied Catalysis A: General*, *421*, pp.58-69.

Dasireddy, V.D., Singh, S., and Friedrich, H.B., 2015. Effect of the support on the oxidation of heptane using vanadium supported on alkaline earth metal hydroxyapatites. *Catalysis Letters*, *145*, pp.668-678.

De, S., Dokania, A., Ramirez, A. and Gascon, J., 2020. Advances in the design of heterogeneous catalysts and thermocatalytic processes for CO_2 utilization. *ACS Catalysis*, *10* (23), pp.14147-14185.

Deganello, F. and Tyagi, A.K., 2018. Solution combustion synthesis, energy and environment: Best parameters for better materials. *Progress in Crystal Growth and Characterization of Materials*, *64* (2), pp.23-61.

Del Campo, P., Martínez, C. and Corma, A., 2021. Activation and conversion of alkanes in the confined space of zeolite-type materials. *Chemical Society Reviews*, *50* (15), pp.8511-8595.

Di Salvia, N., Malavasi, M.P., Di Salvia, G. and Vaccari, A., 2015. Formation of Ni and Mg vanadates during the flameless oxy-combustion of heavy fuels. *Fuel Processing Technology*, *138*, pp.534-539.

Dibenedetto, A., Angelini, A. and Stufano, P., 2014. Use of carbon dioxide as feedstock for chemicals and fuels: homogeneous and heterogeneous catalysis. *Journal of Chemical Technology & Biotechnology*, *89* (3), pp.334-353.

Dobrota, A.S. and Pašti, I.A., 2020. Chemisorption as the essential step in electrochemical energy conversion. *Journal of Electrochemical Science and Engineering*, *10* (2), pp.141-159.

Dreimann, J., Lutze, P., Zagajewski, M., Behr, A., Górak, A. and Vorholt, A.J., 2016. Highly integrated reactor–separator systems for the recycling of homogeneous catalysts. *Chemical Engineering and Processing: Process Intensification*, *99*, pp.124-131.

Dry, M.E., 1982. Catalytic aspects of industrial Fischer-Tropsch synthesis. *Journal of Molecular Catalysis*, *17* (2-3), pp.133-144.

Elkhalifa, E.A. and Friedrich, H.B., 2010. Oxidative dehydrogenation of *n*-octane using vanadium-magnesium oxide catalysts with different vanadium loadings. *Applied Catalysis A: General*, *373* (1-2), pp.122-131.

Elkhalifa, E.A. and Friedrich, H.B., 2011. On the effect of hydrocarbon/oxygen ratios during the dehydrogenation of *n*-octane over a VMgO catalyst. *Catalysis letters*, *141*, pp.554-564.

Elkhalifa, E.A. and Friedrich, H.B., 2014. Oxidative dehydrogenation and aromatization of *n*-octane over VMgO catalysts obtained by using different MgO precursors and different precursor treatments. *Journal of Molecular Catalysis A: Chemical*, *392*, pp.22-30.

Elkhalifa, E.A. and Friedrich, H.B., 2014. Oxidative dehydrogenation and aromatization of n-octane over VMgO catalysts obtained by using different MgO precursors and different precursor treatments. *Journal of Molecular Catalysis A: Chemical*, *392*, pp.22-30.

Elkhalifa, E.A. and Friedrich, H.B., 2018. Magnesium oxide as a catalyst for the dehydrogenation of *n*-octane. *Arabian journal of chemistry*, *11* (7), pp.1154-1159.

Elkhalifa, E.A. and Friedrich, H.B., 2019. Oxidative dehydrogenation *of n*-octane over a vanadium–magnesium oxide catalyst: Influence of the gas hourly space velocity. *Arabian Journal of Chemistry*, *12* (8), pp.2464-2469.

Fadlalla, M.I. and Friedrich, H.B., 2014. The effect of the oxidation environment on the activity and selectivity to aromatics and octenes over cobalt molybdate in the oxidative dehydrogenation of *n*-octane. *Catalysis Science & Technology*, *4* (12), pp.4378-4385.

Fadlalla, M.I., Farahani, M.D. and Friedrich, H.B., 2018. Three inter-linked active sites in the dehydrogenation of *n*-octane over magnesium molybdate based catalysts and their influences on coking and cracking side reactions. *Molecular Catalysis*, *461*, pp.86-96.

Fathi, H., Masoudpanah, S.M., Alamolhoda, S. and Parnianfar, H., 2017. Effect of fuel type on the microstructure and magnetic properties of solution combusted Fe_3O_4 powders. *Ceramics International*, *43* (10), pp.7448-7453.

Frikha, K., Bennici, S., Bouaziz, J., Chaari, K. and Limousy, L., 2020. Influence of the fuel/oxidant ratio on the elaboration of binary oxide catalyst by a microwave-assisted solution combustion method. *Energies*, *13* (12), p.3126.

Ganjkhanlou, Y., Janssens, T.V., Vennestrøm, P.N., Mino, L., Paganini, M.C., Signorile, M., Bordiga, S. and Berlier, G., 2020. Location and activity of VOx species on TiO_2 particles for NH_3-SCR catalysis. *Applied Catalysis B: Environmental*, *278*, p.119337

Gärtner, C.A., van Veen, A.C. and Lercher, J.A., 2013. Oxidative dehydrogenation of ethane: common principles and mechanistic aspects. *ChemCatChem*, *5* (11), pp.3196-3217.

González-Cortés, S.L. and Imbert, F.E., 2013. Fundamentals, properties and applications of solid catalysts prepared by solution combustion synthesis (SCS). *Applied Catalysis A: General*, *452*, pp.117-131.

Gotoh, T., Jeem, M., Zhang, L., Okinaka, N. and Watanabe, S., 2020. Synthesis of yellow persistent phosphor garnet by mixed fuel solution combustion synthesis and its characteristics. *Journal of Physics and Chemistry of Solids*, *142*, pp.109436.

Gounden, N., Friedrich, H.B., Mahadevaiah, N. and Fadlalla, M.I., 2014. Octenes and Aromatics from the Oxidative Dehydrogenation of *n*-Octane over Co/TiO_2 Catalysts. *Catalysis letters*, *144*, pp.2043-2051.

Govender, N., 2007. *A comparative study of mixed metal oxide catalysts for the oxidation of C4, C6 and C8 linear alkanes* (Doctoral dissertation, University of KwaZulu-Natal, Durban).

Grant, J.T., Venegas, J.M., McDermott, W.P. and Hermans, I., 2017. Aerobic oxidations of light alkanes over solid metal oxide catalysts. *Chemical reviews*, *118* (5), pp.2769-2815.

Huber, F., Berwanger, J., Polesya, S., Mankovsky, S., Ebert, H. and Giessibl, F.J., 2019. Chemical bond formation showing a transition from physisorption to chemisorption. *Science*, *366* (6462), pp.235-238.

Ikram, M., Raza, A., Hassan, J.Z., Rafi, A.A., Rafiq, A., Altaf, S. and Ashfaq, A., 2021. Rational Design and Advance Applications of Transition Metal Oxides'. *Transition Metal Compounds: Synthesis, Properties, and Application*, *3*. pp.8373

Ilyina, E.V., Mishakov, I.V., Vedyagin, A.A., Bedilo, A.F. and Klabunde, K.J., 2013. Promoting effect of vanadium on CF_2Cl_2 destructive sorption over nanocrystalline mesoporous MgO. *Microporous and mesoporous materials*, *175*, pp.76-84.

Ivanković, A., Dronjić, A., Bevanda, A.M. and Talić, S., 2017. Review of 12 principles of green chemistry in practice. *International Journal of Sustainable and Green Energy*, *6 (3),* pp.39-48.

James, O.O., Mandal, S., Alele, N., Chowdhury, B. and Maity, S., 2016. Lower alkanes dehydrogenation: Strategies and reaction routes to corresponding alkenes. *Fuel Processing Technology*, *149*, pp.239-255.

Johnson, G.R. and Bell, A.T., 2016. Effects of Lewis acidity of metal oxide promoters on the activity and selectivity of Co-based Fischer–Tropsch synthesis catalysts. *Journal of Catalysis*, *338*, pp.250-264.

Kainthla, I., Bhanushali, J.T., Keri, R.S. and Nagaraja, B.M., 2015. Activity studies of vanadium, iron, carbon and mixed oxides-based catalysts for the oxidative dehydrogenation of ethylbenzene to styrene: A review. *Catalysis Science & Technology*, *5* (12), pp.5062-5076.

Kalz, K.F., Kraehnert, R., Dvoyashkin, M., Dittmeyer, R., Gläser, R., Krewer, U., Reuter, K. and Grunwaldt, J.D., 2017. Future challenges in heterogeneous catalysis: understanding catalysts under dynamic reaction conditions. *ChemCatChem*, *9* (1), pp.17-29.

Kang, W., Ozgur, D.O. and Varma, A., 2018. Solution combustion synthesis of high surface area CeO_2 nanopowders for catalytic applications: reaction mechanism and properties. *ACS Applied Nano Materials*, *1* (2), pp.675-685.

Kang, Y.S., Lu, Y., Chen, K., Zhao, Y., Wang, P., and Sun, W.Y., 2019. Metal–organic frameworks with catalytic centers: From synthesis to catalytic application. *Coordination chemistry reviews*, *378*, pp.262-280.

Karaba, A., Dvořáková, V., Patera, J. and Zámostný, P., 2020. Improving the steam-cracking efficiency of naphtha feedstocks by mixed/separate processing. *Journal of Analytical and Applied Pyrolysis*, *146*, p.104768.

Karami, M., Masoudpanah, S.M. and Rezaie, H.R., 2021. Solution combustion synthesis of hierarchical porous $LiFePO_4$ powders as cathode materials for lithium-ion batteries. *Advanced Powder Technology*, *32* (6), pp.1935-1942.

Kopp Alves, A., Bergmann, C.P. and Berutti, F.A., 2013. Combustion synthesis. In *Novel synthesis and characterization of nanostructured materials*, *102* (9), pp. 11-22.

Lambert, R.M. and Pacchioni, G. eds., 2013. Chemisorption and Reactivity on Supported Clusters and Thin Films: Towards an Understanding of Microscopic Processes in Catalysis (Vol. 331). *Springer Science & Business Media*, *14(18),* pp-456-540.

Langeslay, R.R., Kaphan, D.M., Marshall, C.L., Stair, P.C., Sattelberger, A.P. and Delferro, M., 2018. Catalytic applications of vanadium: a mechanistic perspective. *Chemical reviews*, *119* (4), pp.2128-2191.

Laurenti, M., Castellino, M., Perrone, D., Asvarov, A., Canavese, G. and Chiolerio, A., 2017. Lead-free piezoelectrics: V^{3+} to V^{5+} ion conversion promoting the performances of V-doped Zinc Oxide. *Scientific Reports*, *7* (1), p.41957.

Levchenko, I., Baranov, O., Riccardi, C., Roman, H.E., Cvelbar, U., Ivanova, E.P., Mohandas, M., Ščajev, P., Malinauskas, T., Xu, S. and Bazaka, K., 2023. Nanoengineered Carbon-Based Interfaces for Advanced Energy and Photonics Applications: A Recent Progress and Innovations. *Advanced Materials Interfaces*, *10* (1), p.2201739.

Lyagaeva, J., Danilov, N., Korona, D., Farlenkov, A., Medvedev, D., Demin, A., Animitsa, I. and Tsiakaras, P., 2017. Improved ceramic and electrical properties of $CaZrO_3$-based protonconducting materials prepared by a new convenient combustion synthesis method. *Ceramics International*, *43* (9), pp.7184-7192.

Manukyan, K.V., Cross, A., Roslyakov, S., Rouvimov, S., Rogachev, A.S., Wolf, E.E. and Mukasyan, A.S., 2013. Solution combustion synthesis of nano-crystalline metallic materials: mechanistic studies. *The Journal of Physical Chemistry C*, *117* (46), pp.24417-24427.

Marcu, I.C., Urdă, A., Popescu, I. and Hulea, V., 2017. Layered double hydroxides-based materials as oxidation catalysts. *Sustainable Nanosystems Development, Properties, and Applications, (3),* pp. 59-121.

Mars, P.D.W.V.K. and Van Krevelen, D.W., 1954. Oxidations carried out by means of vanadium oxide catalysts. *Chemical Engineering Science*, *3*, pp.41-59.

Martirosyan, K.S. and Mukasyan, A.S., 2014. Combustion synthesis of nanomaterials. *Dekker encyclopedia of nanoscience and nanotechnology* , *55* (11). pp. 983-1001.

Meima, G.R. and Menon, P.G., 2001. Catalyst deactivation phenomena in styrene production. *Applied Catalysis A: General*, *212* (1-2), pp.239-245.

Misra, S.K. and Andronenko, S.I., 2018. PR of the V^{4+} ion in single crystals of pyrovanadates β-$Mg_2V_2O_7$, α-$Zn_2V_2O_7$: Spin-Hamiltonian parameters. *Magnetic Resonance in Solids. Electronic Journal*, *20* (1), p.18101.

Munnik, P., De Jongh, P.E. and De Jong, K.P., 2015. Recent developments in the synthesis of supported catalysts. *Chemical reviews*, *115* (14), pp.6687-6718.

Najari, S., Saeidi, S., Concepcion, P., Dionysiou, D.D., Bhargava, S.K., Lee, A.F. and Wilson, K., 2021. Oxidative dehydrogenation of ethane: catalytic and mechanistic aspects and future trends. *Chemical Society Reviews*, *50* (7), pp.4564-4605.

Nayak, N.B. and Nayak, B.B., 2016. Temperature-mediated phase transformation, pore geometry and pore hysteresis transformation of borohydride derived in-born porous zirconium hydroxide nanopowders. *Scientific Reports*, *6* (1), p.26404.

Ntola, P., Friedrich, H.B., Mahomed, A.S., Olivier, E.J., Govender, A. and Singh, S., 2022. Exploring the role of fuel on the microstructure of VO_x/MgO powders prepared using solution combustion synthesis. *Materials Chemistry and Physics*, *278*, p.125602.

Ntola, P., Friedrich, H.B., Singh, S., Olivier, E.J., Farahani, M. and Mahomed, A.S., 2023. Effect of the fuel on the surface VO_x concentration, speciation, and physico-chemical characteristics of solution combustion synthesized VO_x/MgO catalysts for *n*-octane activation. *Catalysis Communications*, *174*, p.p.106571.

Pacchioni, G. and Freund, H., 2013. Electron transfer at oxide surfaces. The MgO paradigm: from defects to ultrathin films. *Chemical reviews*, *113* (6), pp.4035-4072.

Padayachee, D., Dasireddy, V.D.B.C., Bharuth-Ram, K., Singh, S. and Friedrich, H.B., 2015. Phase transformation of iron in hydroxyapatite in the activation of *n*-octane. *Hyperfine Interactions*, *231*, pp.131-136.

Padayachee, D., Mahomed, A.S., Singh, S. and Friedrich, H.B., 2019. Selected metal oxides for CH bond activation of n-octane and propensity for COx formation: An empirical study. *Molecular Catalysis*, *464*, pp.1-9.

Parauha, Y.R., Sahu, V. and Dhoble, S.J., 2021. Prospective of combustion method for preparation of nanomaterials: A challenge. *Materials Science and Engineering: B*, *267*, p.115054.

Pathak, T.K. and Swart, H.C., 2019. Structural and Luminescence Properties of ZnO Nanoparticles Synthesized by Mixture of Fuel Approach in Solution Combustion Method. *Zinc Oxide Based Nano Materials and Devices*, *65* (6), pp.34-39.

Pedentchouk, N. and Turich, C., 2018. Carbon and hydrogen isotopic compositions of n-alkanes as a tool in petroleum exploration. *Geological Society, London, Special Publications*, *468* (1), pp.105-125.

Pellizzeri, T.M.S., McMillen, C.D., Pellizzeri, S., Wen, Y., Getman, R.B., Chumanov, G. and Kolis, J.W., 2017. Strontium manganese vanadates from hydrothermal brines: Synthesis and structure of Sr_2Mn_2 (V_3O_{10}) (VO_4), Sr_3Mn (V_2O_7)$_2$, and Sr_2Mn (VO_4)$_2$ (OH). *Journal of Solid-State Chemistry*, *255*, pp.225-233.

Prucker, T., Lamberty, A., Thiessen, J., König, M. and Jess, A., 2022. Kinetics of dehydrogenation of *n*-octane on a promoted Pt-catalyst. *Chemical Engineering Journal*, *442*, p.136233.

Ramirez, A., Dutta Chowdhury, A., Dokania, A., Cnudde, P., Caglayan, M., Yarulina, I., Abou-Hamad, E., Gevers, L., Ould-Chikh, S., De Wispelaere, K. and Van Speybroeck, V., 2019. Effect of zeolite topology and reactor configuration on the direct conversion of CO_2 to light olefins and aromatics. *ACS Catalysis*, *9* (7), pp.6320-6334.

Ran, T., 2017. Versatile multi-faceted bimetallic catalysts for Benzylic CH oxidation. *Chemical Society Reviews*, *45* (7), pp.295.

Riahi, Z., Bounaouara, H., Hraiech, I., Mergheni, M.A., Sautet, J.C. and Nasrallah, S.B., 2017. Combustion with mixed enrichment of oxygen and hydrogen in lean regime. *International Journal of Hydrogen Energy*, *42* (13), pp.8870-8880.

Rosa, R., Veronesi, P. and Leonelli, C., 2013. A review on combustion synthesis intensification by means of microwave energy. *Chemical Engineering and Processing: Process Intensification*, *71*, pp.2-18.

Rostom, S., 2018. Propane Oxidative Dehydrogenation Under Oxygen-free Conditions Using Novel Fluidizable Catalysts: *Reactivity, Kinetic Modelling and Simulation Study Journal of Solid-State Chemistry*, *287*, pp.546-555.

Saghir, A.V., Beidokhti, S.M., Khaki, J.V. and Salimi, A., 2021. One-step synthesis of single-phase (Co, Mg, Ni, Cu, Zn) O High entropy oxide nanoparticles through SCS procedure: Thermodynamics and experimental evaluation. *Journal of the European Ceramic Society*, *41* (1), pp.563-579.

Samantaray, M.K., D'Elia, V., Pump, E., Falivene, L., Harb, M., Ould Chikh, S., Cavallo, L. and Basset, J.M., 2019. The comparison between single atom catalysis and surface organometallic catalysis. *Chemical reviews*, *120* (2), pp.734-813.

Sánchez-García, J.L., Handy, B.E., Ávila-Hernández, I.N., Rodríguez, A.G., García-Alamilla, R. and Cardenas-Galindo, M.G., 2020. Structure, acidity, and redox aspects of $VO_x/ZrO_2/SiO_2$ catalysts for the n-butane oxidative dehydrogenation. *Catalysts*, *10* (5), p.550.

Sánchez-Jiménez, P.E., Valverde, J.M., Perejón, A., de la Calle, A., Medina, S. and Pérez-Maqueda, L.A., 2016. Influence of ball milling on CaO crystal growth during limestone and dolomite calcination: effect on CO_2 capture at calcium looping conditions. *Crystal Growth & Design*, *16* (12), pp.7025-7036.

Sasikumar, S. and Vijayaraghavan, R., 2008. Solution combustion synthesis of bioceramic calcium phosphates by single and mixed fuels—a comparative study. *Ceramics International*, *34* (6), pp.1373-1379.

Satyanarayana, C.V., Srikant, D. and Gurav, H.R., 2016. Catalyst deactivation and regeneration. *Industrial Catalytic Processes for Fine and Specialty Chemicals*, *657*, pp. 187-219.

Schauermann, S. and Freund, H.J., 2015. Model approach in heterogeneous catalysis: kinetics and thermodynamics of surface reactions. *Accounts of Chemical Research*, *48* (10), pp.2775-2782.

Serafin, J., Ouzzine, M., Cruz Jr, O.F., Sreńscek-Nazzal, J., Gómez, I.C., Azar, F.Z., Mafull, C.A.R., Hotza, D. and Rambo, C.R., 2021. Conversion of fruit waste-derived biomass to highly microporous activated carbon for enhanced CO_2 capture. *Waste Management*, *136*, pp.273-282.

Sherikar, B.N. and Umarji, A.M., 2011. Effect of adiabatic flame temperature on nano alumina powders during solution combustion process. *Transactions of the Indian Ceramic Society*, *70* (3), pp.167-172.

Sherikar, B.N. and Umarji, A.M., 2013. Synthesis of γ-alumina by solution combustion method using mixed fuel approach (urea+ glycine fuel). *International Journal of Research in Engineering and Technology, 5*.

Shinde, P.A. and Jun, S.C., 2020. Review on recent progress in the development of tungsten oxide-based electrodes for electrochemical energy storage. *ChemSusChem*, *13* (1), pp.11-38.

Siddiqui, M., Azam, M.A. and Ali, H.M., 2022. Parametric evaluation of condensate water yield from plain finned tube heat exchangers in atmospheric water generation. *Arabian Journal for Science and Engineering*, *47* (12), pp.16251-16271.

Sushchenko, E.D., Kharlamova, T.S., Izaak, T.I. and Vodyankina, O.V., 2017. Supported MgO–V_2O_5/Al_2O_3 catalysts for oxidative propane dehydration: Effect of the molar Mg: V ratio on the phase composition and catalytic properties of samples. *Kinetics and Catalysis*, *58*, pp.630-641.

Taghavinezhad, P., Haghighi, M. and Alizadeh, R., 2018. Sonosynthesis of VO_x/MCM-41 nanocatalyst enhanced by various metal oxides (Mg, AL, Zr) for CO_2-oxidative dehydrogenation of ethane to ethylene. *Microporous and Mesoporous Materials*, *261*, pp.63-78.

Takagi, F., Kageshima, Y., Teshima, K., Domen, K. and Nishikiori, H., 2021. Enhanced photoelectrochemical performance from particulate ZnSe:Cu(In, Ga)Se_2 photocathodes during solar hydrogen production via particle size control. *Sustainable Energy & Fuels*, *5* (2), pp.412-423.

Tang, R., Li, Y., Xie, S., Li, N., Chen, J., Gao, C., Zhu, P. and Wang, X., 2016. Exploring the coordination change of vanadium and structure transformation of metavanadate MgV_2O_6 under high pressure. *Scientific Reports*, *6*(1), p.38566.

Thoda, O., Xanthopoulou, G., Vekinis, G. and Chroneos, A., 2018. Review of recent studies on solution combustion synthesis of nanostructured catalysts. *Advanced Engineering Materials*, *20* (8), p.1800047.

Toniolo, J.C., Takimi, A.S. and Bergmann, C.P., 2010. Nanostructured cobalt oxides (Co_3O_4 and CoO) and metallic Co powders synthesized by the solution combustion method. *Materials Research Bulletin*, *45* (6), pp.672-676.

Valenzuela, R.X. and Cortés Corberán, V., 2000. On the intrinsic activity of vanadium centres in the oxidative dehydrogenation of propane over V–Ca–O and V–Mg–O catalysts. *Topics in Catalysis*, *11*, pp.153-163.

Varma, A., Mukasyan, A.S., Rogachev, A.S. and Manukyan, K.V., 2016. Solution combustion synthesis of nanoscale materials. *Chemical reviews*, *116* (23), pp.14493-14586.

Védrine, J.C. and Fechete, I., 2016. Heterogeneous partial oxidation catalysis on metal oxides. *Comptes Rendus Chimie*, *19* (10), pp.1203-1225.

Védrine, J.C., 2015. Acid–base characterization of heterogeneous catalysts: an up-to-date overview. *Research on Chemical Intermediates*, *41*, pp.9387-9423.

Védrine, J.C., 2017. Heterogeneous catalysis on metal oxides. *Catalysts*, 7 (11), pp.341.

Védrine, J.C., 2019. Recent developments and prospectives of acid-base and redox catalytic processes by metal oxides. *Applied Catalysis A: General*, *575*, pp.170-179.

Wachs, I.E., 2013. Catalysis science of supported vanadium oxide catalysts. *Dalton transactions, 42 (33)*, pp.11762-9.

Wang, A., Li, J. and Zhang, T., 2018. Heterogeneous single-atom catalysis. *Nature Reviews Chemistry*, *2* (6), pp.65-81.

Wang, H., 2022. Metal Oxide Catalysts for the CO_2-Assisted Propane Oxidative *Dehydrogenation (Doctoral dissertation, Rutgers the State University of New Jersey, School of Graduate Studies. 1178*, pp.1637-1625.

Wang, J., Wang, J., Wang, S., Li, H., Yan, Q. and Xu, K., 2021. High-energy Al/graphene oxide/$CuFe_2O_4$ nanocomposite fabricated by self-assembly: Evaluation of heat release, ignition behavior, and catalytic performance. *Energetic Materials Frontiers*, *2* (1), pp.22-31.

Wang, Y., Hu, P., Yang, J., Zhu, Y.A. and Chen, D., 2021. C–H bond activation in light alkanes: a theoretical perspective. *Chemical Society Reviews*, *50* (7), pp.4299-4358.

Wang, Y., Hu, P., Yang, J., Zhu, Y.A. and Chen, D., 2021. C–H bond activation in light alkanes: a theoretical perspective. *Chemical Society Reviews*, *50* (7), pp.4299-4358.

Wei, Y.S., Zhang, M., Zou, R. and Xu, Q., 2020. Metal–organic framework-based catalysts with single metal sites. *Chemical Reviews*, *120* (21), pp.12089-12174.

Wen, W. and Wu, J.M., 2014. Nanomaterials via solution combustion synthesis: a step nearer to controllability. *RSC Advances*, *4* (101), pp.58090-58100.

Wu, Q., Wang, L., Zhao, B., Huang, L., Yu, S. and Ragauskas, A.J., 2022. Highly selective hydrogenation of phenol to cyclohexanone over a Pd-loaded N-doped carbon catalyst derived from chitosan. *Journal of Colloid and Interface Science*, *605*, pp.82-90.

Xanthopoulou, G., Thoda, O., Roslyakov, S., Steinman, A., Kovalev, D., Levashov, E., Vekinis, G., Sytschev, A. and Chroneos, A., 2018. Solution combustion synthesis of nano-catalysts with a hierarchical structure. *Journal of catalysis*, *364*, pp.112-124.

Xie, C., Yan, D., Li, H., Du, S., Chen, W., Wang, Y., Zou, Y., Chen, R. and Wang, S., 2020. Defect chemistry in heterogeneous catalysis: recognition, understanding, and utilization. *ACS Catalysis*, *10* (19), pp.11082-11098.

Yun, D., Wang, Y., and Herrera, J.E., 2018. Ethanol Partial Oxidation over VO_x/TiO_2 Catalysts: The Role of Titania Surface Oxygen on Vanadia Reoxidation in the Mars–van Krevelen Mechanism. *ACS Catalysis*, *8* (5), pp.4681-4693.

Zhang, X., Zhang, X., Liu, H., Li, W., Xiao, M., Gao, H. and Liang, Z., 2017. Reduction of energy requirement of CO_2 desorption from a rich CO_2-loaded MEA solution by using solid acid catalysts. *Applied energy*, *202*, pp.673-684.

Zhang, Z., Xiang, L., Lin, F., Wang, Z., Yan, B. and Chen, G., 2021. Catalytic deep degradation of Cl-VOCs with the assistance of ozone at low temperature over MnO_2 catalysts. *Chemical Engineering Journal*, *426*, pp.130814.

Zhao, L., Xu, Q., Shao, Z., Chen, Y., Xue, Z., Li, H. and Zhang, J., 2020. Enhanced oxygen reduction reaction performance using intermolecular forces coupled with more exposed molecular orbitals of triphenylamine in Co-porphyrin electrocatalysts. *ACS Applied Materials & Interfaces*, *12* (41), pp.45976-45986.

Zhong, L., Kropp, T., Baaziz, W., Ersen, O., Teschner, D., Schlögl, R., Mavrikakis, M. and Zafeiratos, S., 2019. Correlation between reactivity and oxidation state of cobalt oxide catalysts for CO preferential oxidation. *ACS Catalysis*, *9* (9), pp.8325-8336.

Zhou, Q., Mou, Y., Ma, X., Xue, L. and Yan, Y., 2014. Effect of fuel-to-oxidizer ratios on combustion mode and microstructure of Li_2TiO_3 nanoscale powders. *Journal of the European Ceramic Society*, *34* (3), pp.801-807.

Zhu, L., Liu, X.Q., Jiang, H.L. and Sun, L.B., 2017. Metal–organic frameworks for heterogeneous basic catalysis. *Chemical reviews*, *117* (12), pp.8129-8176.

APPENDIX A

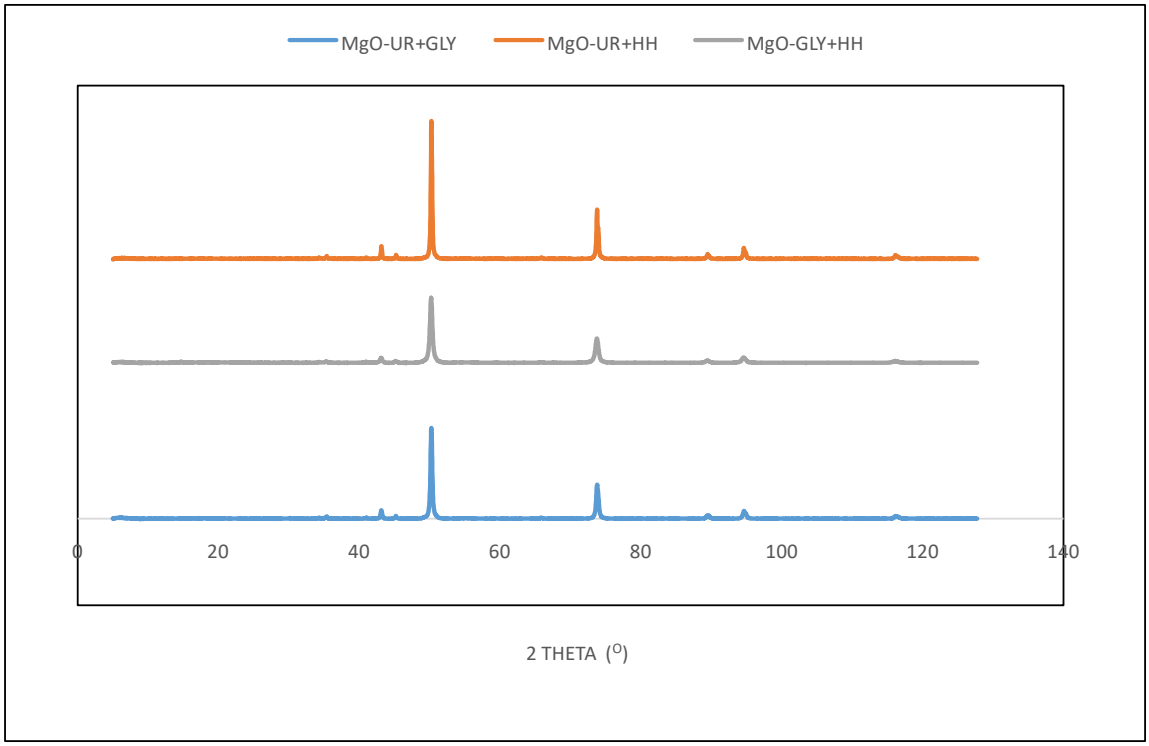

Figure 1A: XRD diffractogram of MgO catalysts

Table 1A: Elemental composition and BET results of MgO

Catalyst	ICP-OES (wt %)	Surface area (m^2/g)
MgO-GLY/UR	83 wt%	23.4
MgO-GLY/HH	84 wt%	21.9
MgO-UR/HH	84 wt%	6.4

APPENDIX B

Table 1B: Calculated Brønsted acid sites for VO_x/MgO catalysts

Variables	GLY/HH	GLY/UR	UR/HH
Apms	0.064	0.185	0.148
Cal. Factor	3.2	3.2	3.2
1/22,414	0.0446	0.0446	0.0446
	1000000	1000000	1000000
1/mass	13	10	11
	0.001	0.001	0.001
Nas	118.743	264.032	232.3482

Table B1: Summary of gas flow rates employed to attain GHSV and C: O ratios in testing

GHSV/h^{-1}	C: O	*n*-octane/mL/min	N_2/mL min^{-1}	Air/ml min-^{1}	% *n*-octane
8000	8: 2	0.08	56,9	72	12%
8000	8 :2	0.04	25	36	5%